arXiv:physics/9709010 v2 14 Dec 1997

Andreas E. Klinkmüller • Doctorate thesis 1997

Akademisk avhandling, som för avläggande av filosofie doktorsexamen
vid Göteborgs Universitet, försvaras vid offentlig disputation
fredagen den 10 oktober 1997 kl 10.10, sal HA2, Hörsalsvägen 4,
Chalmers Tekniska Högskola, Göteborg.

Avhandlingen försvaras på engelska

Department of Physics
Gothenburg University and Chalmers University of Technology
Fysikgränd 3
SE-412 96 Göteborg, Sweden

Electronically available from http://xxx.lanl.gov

On doubly excited states in negative ions

Dubbelt exciterade tillstånd i negativa joner

Andreas E. Klinkmüller
Göteborg 1997

Fysiska Institutionen, Göteborgs Universitet
och Chalmers Tekniska Högskola

ISBN 91-7197-547-0
Chalmers bibliotekets tryckeri

©This copy of the thesis has been supplied on condition that anyone who consults it is understood to recognise that its copyright rests with the author and that no quotation from the thesis, nor any information derived therefrom, may be published without the author's prior written consent.

Abstract

Atomic negative ions are fragile quantum systems with a binding energy one order of magnitude smaller than for atoms. Due to this weak binding, correlation among the valence electrons plays a very important role. For doubly excited states, where two electrons are simultaneously promoted, correlation becomes dominant and is thus no longer a small perturbation to the independent particle behaviour.

Photodetachment is the process where a negative ion absorbs a photon and as a consquence ejects the outermost electron. Investigations of this process have been performed with the laser and ion beams merged over 0.5 m in a collinear geometry. This simultaneously enables high resolution and high sensitivity. By combining measurements with co- and counter-propagating laser and ion beams the Doppler shift can be eliminated to *all* orders. The ion beam facility was equipped with a sputter ion source and a plasma ion source, which together allow the production of atomic negative ions of almost any element. The laser light for the investigations was generated by two excimer pumped dye lasers.

A new detection scheme has been developed. The residual atom of a photodetachment is state selectively ionised by resonance ionisation spectroscopy. This novel detection scheme retains all advantages of the collinear geometry and, at the same time, offers the possibility of measuring partial photodetachment cross sections.

Investigations of the photodetachment threshold of tellurium with neutral particle detection have been performed and yielded an electron affinity of 1 589 618(5) m^{-1}. With state selective detection the Li(2p) photodetachment threshold was investigated and the electron affinity was determined to be 498 490(17) m^{-1}.

Doubly excited states of both Li^- and He^- have been studied. Resonance structure in the Li^- photodetachment cross section near the Li(3p) threshold has been investigated. The structure arises from the autodetaching decay of doubly excited $^1\mathrm{P}^\mathrm{o}$ states of Li^- that are bound with respect to the Li(3p) state. According to an assisting calculation this structure is analogous to the symmetrically excited intra-shell $({}_3\{0\}_3^+)\,{}^1\mathrm{P}^\mathrm{o}$ state in H^-. Higher lying asymmetrically excited inter-shell states were observed to converge on the Li(3p) limit.

In He^- the three doubly excited states, $1\mathrm{s}3\mathrm{s}4\mathrm{s}\,{}^4\mathrm{S}$, $1\mathrm{s}3\mathrm{p}^2\,{}^4\mathrm{P}$ and $1\mathrm{s}3\mathrm{p}4\mathrm{p}\,{}^4\mathrm{P}$ were investigated. The Feschbach resonance associated with the $1\mathrm{s}3\mathrm{s}4\mathrm{s}\,{}^4\mathrm{S}$ state was observed in both the $\mathrm{He}(1\mathrm{s}2\mathrm{s}\,{}^3\mathrm{S}) + \mathrm{e}^-(\epsilon\mathrm{s})$ and the $\mathrm{He}(1\mathrm{s}2\mathrm{p}\,{}^3\mathrm{P}^\mathrm{o}) + \mathrm{e}^-(\epsilon\mathrm{p})$ partial photodetachment cross section, whereas the $1\mathrm{s}3\mathrm{p}^2\,{}^4\mathrm{P}$ and $1\mathrm{s}3\mathrm{p}4\mathrm{p}\,{}^4\mathrm{P}$ resonances were observed in the $\mathrm{He}(1\mathrm{s}2\mathrm{p}\,{}^3\mathrm{P}^\mathrm{o}) + \mathrm{e}^-(\epsilon\mathrm{p})$ partial photodetachment cross section.

The energy positions of all these resonances [$1\mathrm{s}3\mathrm{s}4\mathrm{s}\,{}^4\mathrm{S}$: $E_0 = (2\,386\,803.1 \pm 4.2)$ m^{-1}, $\Gamma = 160(16)$ m^{-1}; $1\mathrm{s}3\mathrm{p}^2\,{}^4\mathrm{P}$: $E_0 = 2.478\,2(55) \times 10^6$ m^{-1}, $\Gamma = 40(3) \times 10^3$ m^{-1}; $1\mathrm{s}3\mathrm{p}4\mathrm{p}\,{}^4\mathrm{P}$: $E_0 = 2\,633\,297(40)$ m^{-1}, $\Gamma = 492(35)$ m^{-1}] agree with a recent ab initio calculation by Xi and Froese Fischer [Phys. Rev. A, **53**(5), 3169, (1996)] to an accuracy of up to 10^{-4}. The widths, however, are less accurate both in experiment and theory: The width of the $1\mathrm{s}3\mathrm{s}4\mathrm{s}\,{}^4\mathrm{S}$ resonance agrees with this calculation, but for the $1\mathrm{s}3\mathrm{p}^2\,{}^4\mathrm{P}$ resonance there is a slight discrepancy and the $1\mathrm{s}3\mathrm{p}4\mathrm{p}\,{}^4\mathrm{P}$ resonance is only half as broad as predicted.

Sammanfattning

Atomära negativa joner är bräckliga kvantsystem med bindingsenergier som är typiskt en storleksordning lägre än för atomer. På grund av denna svaga bindning spelar korrelationen mellan valenselektronerna en mycket viktig roll. I dubbelt exciterade tillstånd, där två elektroner är samtidigt exciterade, kan korrelationen dominera och den utgör följdaktligen inte längre endast en liten störning till den oberoende partikelmodellen.

I fotoneutralisationsprocessen absorberar en negativ jon en foton varvid den yttersta elektronen emitteras. Undersökningar av denna process har genomförts i en kollinjär geometri där laser- och jonstrålarna överlappade varandra över 0.5 m. Detta möjliggjorde samtidigt både hög upplösning och hög känslighet i experimenten. Genom att kombinera mätningar med parallella och anti-parallella laser och jonstrålar kan Dopplerförskjutning elemineras till alla ordningar. Jonstråleanläggningen är utrustad med en sputter jonkälla och en plasma jonkälla, vilka tillsammans möjliggör produktionen av atomärer negativa joner av nästan alla grundämnen. Laserljuset genereras av två excimerpumpade färgämneslasrar.

En ny detektionsmetod har utveklats. De i fotoneutralisationsprocessen bildade atomerna detekterades härvid tillståndsselektivt med hjälp av resonansjonisationsspektroskopi. Med denna nya detektionsmetod kan fördelarna med en kolinjär geometri bevaras, samtidigt som det blir möjligt att mäta partiella fotoneutralisationstvärsnitt.

Undersökningar av fotoneutralisationströskeln hos tellur med neutralpartikeldetektion har genomförts och gav en elektronaffinitet på 1 589 618(5) m^{-1}. Med den tillståndsselektiva detektionsmetoden undersöktes Li(2p)-tröskeln och elektronaffiniteten betämdes i detta fall till 498 490(17) m^{-1}.

Dubbelt exciterade tillstånd hos både Li^- och He^- har studerats. I Li^- har resonansstrukturer i fotoneutralisationstvärsnittet nära Li(3p)-tröskeln studerats. Strukturen härstammar från autoneutraliserande dubbelt exciterat $^1\mathrm{P}^\mathrm{o}$-tillstånd hos Li^- som är bundet till 3p-tillståndet i den neutrala atomen. Teoretiska studier har visat att denna struktur är analog till det symmetriskt exciterade tillståndet $({}_1\{0\}_3^+)\,{}^1\mathrm{P}^\mathrm{o}$ i H^-. Högre liggande assymmetriskt exciterade tillstånd som konvergera till Li(3p) gränsen har också observerats.

I He^- har de tre dubbelt exciterade tillstånden, $1\mathrm{s}3\mathrm{s}4\mathrm{s}\,{}^4\mathrm{S}$, $1\mathrm{s}3\mathrm{p}^2\,{}^4\mathrm{P}$ och $1\mathrm{s}3\mathrm{p}4\mathrm{p}\,{}^4\mathrm{P}$, oberverats. En Feschbachresonans associerad med $1\mathrm{s}3\mathrm{s}4\mathrm{s}\,{}^4\mathrm{S}$ tillståndet har studerats i de partiella fotoneutralisationstvärsnitten $\mathrm{He}(1\mathrm{s}2\mathrm{s}\,{}^3\mathrm{S}) + \mathrm{e}^-(\epsilon\mathrm{s})$ och $\mathrm{He}(1\mathrm{s}2\mathrm{p}\,{}^3\mathrm{P}^\mathrm{o}) + \mathrm{e}^-(\epsilon\mathrm{p})$, och $1\mathrm{s}3\mathrm{p}^2\,{}^4\mathrm{P}$ och $1\mathrm{s}3\mathrm{p}4\mathrm{p}\,{}^4\mathrm{P}$ resonanserna har observerats i det partiella fotoneutralisationstvärsnittet $\mathrm{He}(1\mathrm{s}2\mathrm{p}\,{}^3\mathrm{P}^\mathrm{o}) + \mathrm{e}^-(\epsilon\mathrm{p})$.

Energierna hos alla resonanserna [$1\mathrm{s}3\mathrm{s}4\mathrm{s}\,{}^4\mathrm{S}$: $E_0 = (2\,386\,803.1\pm4.2)\,\mathrm{m}^{-1}$, $\Gamma = 160(16)\,\mathrm{m}^{-1}$; $1\mathrm{s}3\mathrm{p}^2\,{}^4\mathrm{P}$: $E_0 = 2.478\,2(55)\times10^6\,\mathrm{m}^{-1}$, $\Gamma = 40(3)\times10^3\,\mathrm{m}^{-1}$; $1\mathrm{s}3\mathrm{p}4\mathrm{p}\,{}^4\mathrm{P}$: $E_0 = 2\,633\,297(40)\,\mathrm{m}^{-1}$, $\Gamma = 492(35)\,\mathrm{m}^{-1}$] överensstämmer med en nyligen publicerad ab initio beräkning av Xi och Froese Fischer [Phys. Rev. A, **53**(5), 3169, (1996)] upp till en noggrannhet av 10^{-4}. Vidderna hos resonansen är dock mindre noggrannt bestämda i såväl experiment som teori och överensstämmelsen är här mindre god. För $1\mathrm{s}3\mathrm{s}4\mathrm{s}\,{}^4\mathrm{S}$ resonansen är skillnad mellan teori och experiment mindre än den experimentella noggrannheten, medan det för $1\mathrm{s}3\mathrm{p}^2\,{}^4\mathrm{P}$ resonansen finns en liten avvikelse. För $1\mathrm{s}3\mathrm{p}4\mathrm{p}\,{}^4\mathrm{P}$ resonansen, slutligen, är det experimentella värdet bara hälften av den teoteriska förutsägelsen.

Zusammenfassung

Atomare negative Ionen sind zerbrechliche Quantensysteme mit einer um eine Größenordnung niedrigeren Bindungsenergie als Atome. Aufgrund dieser schwachen Bindung spielt Korrelation unter den Valenzelektronen eine sehr wichtige Rolle. In doppelt angeregten Zuständen, wo zwei Elektronen gleichzeitig angeregt sind, kann Korrelation dominierend werden und ist folglich keine kleine Störung des unabhängigen Teilchenverhaltens mehr.

Photoneutralisation ist der Prozess bei dem ein negatives Ion ein Photon absorbiert und infolgedessen das äußerste Elektron abgibt. Die Untersuchungen sind in kollinearer Geometrie mit einem Laser und Ionenstrahlüberlapp von 0.5 m Länge durchgeführt. Dieses ermöglicht gleichzeitig hohe Auflösung und hohe Empfindlichkeit. Durch Kombinieren von Messungen mit gleich- und gegenläufigen Laser- und Ionenstrahlen kann die Dopplerverschiebung in *allen* Ordnungen beseitigt werden. Die Ionenstrahlanlage ist mit einer Zerstäuberquelle und einer Plasmaquelle ausgerüstet, die zusammen die Produktion negativer Ionen nahezu aller Elemente erlauben. Das Laserlicht für die Untersuchungen wird von zwei excimergepumpten Farbstofflasern erzeugt.

Eine neue Nachweismethode ist entwickelt worden. Das von einer Photoneutralisation verbleibende Atom wird mit Resonanzionisationsspektroskopie zustandsempfindlich ionisiert. Diese neuartige Nachweismethode bewahrt alle Vorteile der kollinearen Geometrie und bietet gleichzeitig die Möglichkeit partielle Photoneutralisationsquerschnitte zu messen.

Untersuchungen der Photoneutralisationsschwelle von Tellur mit Neutralteilchennachweis wurden durchgeführt und ergaben eine Elektronenaffinität von 1 589 618(5) m^{-1}. Mit dem zustandsempfindlichen Nachweis wurde die Li(2p) Photoneutralisationsschwelle untersucht und die Elektronenaffinität zu 498 490(17) m^{-1} bestimmt.

Doppelt angeregte Zustände von Li^- und He^- sind studiert worden. Es wurde Resonanzstruktur im Li^- Photoneutralisationsquerschnitt nahe der Li(3p) Schwelle untersucht. Die Struktur wird durch einen autoneutralisierenden doppelt angeregten $^1\mathrm{P}^\mathrm{u}$ Zustand von Li^-, der im Bezug auf den Li(3p) Zustand gebunden ist, hervorgerufen. Gemäß einer begleitenden Berechnung ist diese Struktur analog zum symmetrischen intra-Schalen Zustand $({}_3\{0\}_3^+)\,{}^1\mathrm{P}^\mathrm{u}$ des H^-. Höherliegende asymmetrisch inter-Schalen Zustände konvergieren zur Li(3p) Schwelle.

In He^- sind drei doppelt angeregte Zustände, $1s3s4s\,{}^4\mathrm{S}$, $1s3p^2\,{}^4\mathrm{P}$ und $1s3p4p\,{}^4\mathrm{P}$, untersucht worden. Die Feschbachresonanz verbunden mit dem $1s3s4s\,{}^4\mathrm{S}$ Zustand ist im $\mathrm{He}(1s2s\,{}^3\mathrm{S}) + \mathrm{e}^-(\epsilon s)$ und $\mathrm{He}(1s2p\,{}^3\mathrm{P}^\mathrm{o}) + \mathrm{e}^-(\epsilon p)$ partiellen Photoneutralisationsquerschnitt beobachtet worden und die $1s3p^2\,{}^4\mathrm{P}$ und $1s3p4p\,{}^4\mathrm{P}$ Resonanzen wurden im $\mathrm{He}(1s2p\,{}^3\mathrm{P}^\mathrm{o}) + \mathrm{e}^-(\epsilon p)$ partiellen Photoneutralisationsquerschnitt beobachtet.

Die Energie aller Resonanzen [$1s3s4s\,{}^4\mathrm{S}$: $E_0 = (2\,386\,803.1 \pm 4.2)\,\mathrm{m}^{-1}$, $\Gamma = 160(16)\,\mathrm{m}^{-1}$; $1s3p^2\,{}^4\mathrm{P}$: $E_0 = 2.478\,2(55) \times 10^6\,\mathrm{m}^{-1}$, $\Gamma = 40(3) \times 10^3\,\mathrm{m}^{-1}$; $1s3p4p\,{}^4\mathrm{P}$: $E_0 = 2\,633\,297(40)\,\mathrm{m}^{-1}$, $\Gamma = 492(35)\,\mathrm{m}^{-1}$] stimmt mit einer jüngst erschienen ab initio Rechnung von Xi und Froese Fischer [Phys. Rev. A, **53**(5), 3169, (1996)] bis zu einer Genauigkeit von 10^{-4} überein. Die Breiten sind sowohl im Experiment als auch in der Theorie ungenauer: Die Breite der $1s3s4s\,{}^4\mathrm{S}$ Resonanz stimmt mit der Berechnung überein, aber für die $1s3p^2\,{}^4\mathrm{P}$ Resonanz gibt es eine leichte Abweichung und die $1s3p4p\,{}^4\mathrm{P}$ Resonanz ist nur halb so breit wie vorhergesagt.

Riassunto

Gli ioni negativi sono dei fragili sistemi quantistici con energie legame di un ordine di grandezza inferiore a quelle degli atomi. A causa di queste basse energie di legame la correlazione tra gli elettroni di valenza gioca un ruolo molto importante. Per stati doppiamente eccitati, dove due elettroni sono simultaneamente promossi, la correlazione diviene dominante e quindi non può più essere consderata una piccola perturbazione del modello a particelle indipendenti.

La fotoneutralizzazione è un processo in cui uno ione negativo assorbe un fotone ed emette un elettrone dello stato più esterno. Lo studio di questo processo è stato qui compiuto utilizzando una geometria collineare in cui il raggio laser ed il fascio ionico sono accoppiati per una lunghezza di 0.5 m. Ciò migliora simultaneamente risoluzione e sensibilità. Combinando misure con il raggio laser e il fascio ionico co- e contro-propaganti lo spostamento Doppler può essere eliminato *a tutti* gli ordini. La strumentazione che produce il fascio ionico è provvista di una sorgente a 'sputtering' e una sorgente di plasma, che insieme permettono la produzione di ioni negativi per quasi tutti gli elementi. La radiazione laser usata nell'indagine è generata da due laser a coloranti pompati da un laser ad eccimeri.

È stato sviluppato un nuovo schema di rivelazione. L'atomo risultante dal fotoneutralizzazione è ionizzato stato-selettivamente (spettroscopia a risonanza di ionizzazione). Questo nuovo schema conserva i vantaggi di una geometria collineare e allo stesso tempo offre la possibilità di misurare sezioni d'urto parziali efficaci di fotoneutralizzazione.

Le indagini sulla soglia di fotoneutralizzazione del Te^- con rivelazione delle particelle neutre hanno prodotto una misura dell'affinità elettronica di 1 589 618(5) m^{-1}. La spettroscopia a risonanza di ionizzazione è stata utilizzata per lo studio della soglia di fotoneutralizzazione del Li(2p) e si è determinato che l'affinità elettronica del litio è 498 490(17) m^{-1}.

Sono stati studiati gli stati doppiamente eccitati di Li^- e He^- e la struttura risonante della sezione d'urto efficace del Li^- vicino alla soglia del Li(3p). La struttura deriva dall'autoneutralizzazione degli stati doppiamente eccitati $^1P^o$ del Li^- che sono legati rispetto allo stato del Li(3p). Secondo alcuni calcoli questa struttura è analoga a quella dello stato intraguscio $({}_3\{0\}_3^+)\,{}^1P^o$ dell'H^-. Gli stati interguscio superiori ecciatati asimmetricamente, sono stati osservati e la loro energia converge a quella del Li(3p).

Per l'He^- abbiamo studiato i tre stati doppiamente eccitati 1s3s4s ^4S, 1s3p^2 ^4P e 1s3p4p-^4P. Le risonanze di Feschbach associate con lo stato 1s3s4s ^4S sono state osservate in entrambe le sezioni d'urto parziali efficaci degli stati He(1s2s ^3S) + $e^-(\epsilon s)$ e He(1s2p $^3P^o$) + $e^-(\epsilon p)$, mentre le risonanze 1s3p^2 ^4P e 1s3p4p ^4P sono state osservate nella sezione d'urto parziale efficace He(1s2p $^3P^o$) + $e^-(\epsilon p)$.

Le posizioni di tutte le risonanze [1s3s4s ^4S: $E_0 = (2\,386\,803.1 \pm 4.2)\,m^{-1}$, $\Gamma = 160(16)\,m^{-1}$; 1s3p^2 ^4P: $E_0 = 2.478\,2(55) \times 10^6\,m^{-1}$, $\Gamma = 40(3) \times 10^3\,m^{-1}$; 1s3p4p ^4P: $E_0 = 2\,633\,297(40)\,m^{-1}$, $\Gamma = 492(35)\,m^{-1}$] sono in accordo con recenti calcoli ab initio di Xi e Froese Fischer [Phys. Rev. A, **53**(5), 3169, (1996)] con un'accuratezza fino a 10^{-4}. Le larghezze di riga, comunque, sono meno accurate sia nell'esperimento che nella teoria: la larghezza di riga della risonanza 1s3s4s ^4S è in accordo con i calcoli, ma per la risonanza 1s3p^2 ^4P c'è una leggera discrepanza e la risonanza 1s3p4p ^4P è larga solo la metà di quanto previsto.

Contents

List of figures **11**

List of tables **13**

Preface **15**

1. Introduction **17**

2. Atomic negative ions **19**
2.1. Structure of atomic negative ions 23
2.2. Excited states 24
2.3. Formation 27

3. Photodetachment of negative ions **29**
3.1. Threshold behaviour 31
3.2. Resonance structure 35
3.3. Asymptotic behaviour 40

4. Experimental apparatus **41**
4.1. The negative ion beam apparatus 42
4.2. The laser system 46
4.3. The detection system 48
4.4. Data acquisition and processing 50

5. Threshold studies **53**
5.1. Tellurium electron affinity 53
5.2. Lithium electron affinity 56

6. Autodetachment resonances **62**
6.1. Li^- doubly excited states 62
6.2. He^- doubly excited states 65

7. Summary and conclusion **76**
7.1. Summary of Results 76
7.2. Conclusion 79

A. Glossary **81**

B. Symbols **83**

C. He^- partial cross sections **86**

Bibliography **89**

List of Figures

2.1. Binding energies of H and H^- 24
2.2. Asymptotic potentials of H and H^- 24
2.3. Significance of A for doubly excited states 27

3.1. Analytic model of H^- photodetachment cross section 30
3.2. Calculated total photodetachment cross section of Li^- 31
3.3. Schematic oscillator strength across a threshold 32
3.4. Scattering geometry 33
3.5. Wigner threshold law 33
3.6. O'Malleys modification of the Wigner law 34
3.7. Two channel level scheme 35
3.8. Beutler-Fano profile 37
3.9. Three channel photodetachment model 39
3.10. Shape resonance model 39
3.11. Wigner cusp 40
3.12. Asymptotic photodetachment cross section 40

4.1. Ion beam machine 41
4.2. Sputter ion source 42
4.3. Plasma ion source 43
4.4. Wien filter 43
4.5. Charge exchange cell 44
4.6. Ion optics in the beam lines 45
4.7. Ion optics in the interaction-detection chamber 45
4.8. Laser system overview 46
4.9. Laser arrangement 47
4.10. Two colour laser beam path 47
4.11. Interaction-detection chamber 49
4.12. Logic of the detection system 49
4.13. Time structure of the signal 50
4.14. Logbook pages 52

5.1. Tellurium excitation scheme 54
5.2. Tellurium scan overview 55
5.3. $Te(5p^4)+\epsilon s$ threshold 56

5.4. Tellurium electron affinity 56
5.5. Li^- excitation scheme I 58
5.6. Static electric field ionisation 58
5.7. Lithium Rydberg series and fine structure 59
5.8. Li(2p+ϵs) threshold 60
5.9. Lithium electron affinity 61

6.1. Li^- excitation scheme II 63
6.2. Photodetachment cross section near the Li(3p) threshold 64
6.3. Modified interaction-detection chamber 67
6.4. He^- excitation scheme 69
6.5. Partial photodetachment cross sections near the $He^-(1s3s4s\,^4S)$ state 72
6.6. Photodetachment cross section near the $He^-(n{=}3\ ^4P)$ states 73
6.7. Energies of He^- doubly excited states near the He(n=3) thresholds . 74
6.8. Widths of He^- doubly excited states near the He($n = 3$) thresholds . 75

C.1. He(1s3s ^{3}S) partial cross section of ^{4}S symmetry 86
C.2. He(1s3p ^{3}P^o) partial cross section of ^{4}P symmetry 87
C.3. He(1s2s ^{3}S) partial cross sections 87
C.4. He(1s2p ^{3}P^o) partial cross sections 88

List of Tables

2.1. Autodetachment selection rules 26

5.1. Tellurium calibration lines 54
5.2. Tellurium electron affinity 55
5.3. Lithium electron affinity 61

6.1. Li^- doubly excited states 65
6.2. $He^-(1s3s4s\,^4S)$ calibration lines 68
6.3. $He^-(1s3s4s\,^4S)$ state 70
6.4. $He^-(n = 3\,^4P)$ states 71
6.5. $He^-(1s3p4p\,^4P)$ calibration lines 72

7.1. Tellurium electron affinity 76
7.2. Lithium electron affinity 77
7.3. Li^- doubly excited states 77
7.4. He^- doubly excited states 78

A.1. Abbreviations 81

B.1. Symbol conventions 83
B.2. Symbols in the thesis 83

Preface

This work was done in the atomic physics group of Professor Ingvar Lindgren at the department of Atomic Physics, Göteborg University and Chalmers University of Technology. The presence of both theorists and experimentalists in the same group contributes to a stimulating atmosphere of scientific commitment.

The theorists of our group have been mainly engaged in accurate calculations for heavy atomic systems where relativistic, nuclear and QED effects are important. On the experimental side research has been conducted in the fields of hyperfine structure, combustion, trace element analysis, optical tweezers, and the negative ions.

During my first year I participated in building up a new negative ion beam apparatus. Meanwhile I also learned Swedish. To begin with the experiments were mainly led by others but later I gradually ran the apparatus more and more on my own. My first real enterprise, an investigation of calcium, was a failure, at least as far as publishable results are concerned. Thereafter things worked out better and we started our very successful investigations of the negative lithium ion. In early 1995 we had a breakthrough with the application of a state selective detection scheme based on resonance ionisation. This finding triggered a series of resonance structure investigations that has so far not found an end. Also the most important experiments for this thesis use the state selective detection scheme.

Above all I wish to cordially thank my supervisor Dag Hanstorp for his guidance and encouragement far beyond his 'work assignments'. His commitment to supervision is perhaps best illustrated by the weekly meeting held with each doctoral student. I am deeply indebted to him and wish to express my gratitude for his continued support. This doctorate would not have been possible had Professor Ingvar Lindgren not accepted me as his student, and therefore I wish to convey my thanks to him and hope to have lived up to his expectations.

Many of people have contributed to render the work presented here possible. Among them I acknowledge James R. Petersons and Professor David J. Pegg for many discussions and ideas concerning the studies of resonance structure in the photodetachment cross section of calcium, lithium and helium. My colleagues Ulric Ljungblad and Gunnar Haeffler are acknowledged for countless stimulating discussions.

This thesis is based on the following publications:

- U. Berzinsh, G. Haeffler, D. Hanstorp, A. Klinkmüller, E. Lindroth, U. Ljungblad, and D. J. Pegg. Resonance structure in the Li^- photodetachment

cross section. *Phys. Rev. Lett.*, 74(24):4795–4798, June 1995. e-print: physics/9703015.

- Gunnar Haeffler, Dag Hanstorp, Igor Kiyan, Andreas E. Klinkmüller, Ulric Ljungblad and David J. Pegg. Electron affinity of Li: A state-selective measurement. *Phys. Rev. A*, 53(6):4127–4131, June 1996. e-print: physics/9703013.

- Gunnar Haeffler, Andreas E. Klinkmüller, Jonas Rangell, Uldis Berzinsh, and Dag Hanstorp. The electron affinity of tellurium. *Z. Phys. D*, 38:211–214, October 1996. e-print: physics/9703012.

- Andreas E. Klinkmüller, Gunnar Haeffler, Dag Hanstorp, Igor Yu. Kiyan, Uldis Berzinsh, Christopher Ingram, David J. Pegg, and James R. Peterson. Photodetachment study of the $1s3s4s\,^4S$ resonance in He^-. *Phys. Rev. A*, accepted for publication, 1997. e-print: physics/9703011.

- D. Hanstorp, G. Haeffler, A. E. Klinkmüller, U. Ljungblad, U. Berzinsh, I. Yu. Kiyan, and D. J. Pegg. Two electron dynamics in photodetachment. *Adv. Quant. Chem.*, 29, 1997. e-print: physics/9706013.

The results have also been presented at several international conferences [1–7].

All occurrences of author names in this thesis shall be understood as 'author et al.' if applicable. The reader, tempted to cry out "foul", is referred to the bibliography to find that there, contrary to common practice in physics, the full list of authors and the title are presented.

After having suffered from the stupidity of unit conversion from CGS and other systems for many years I decided to use the SI [8, 9] units throughout this thesis. To convert eV to m^{-1} we used the recommended factor 806 554.10(24) (m^{-1}/eV) [10]. For other eventual conversions we used the factors from the same source [10]. Theoretical results are sometimes quoted in element specific atomic units.

1. Introduction

Negative ion research is a rapidly developing field of atomic physics. Good introductions to the subject of negative ions are given in the books of Massey [11] and Smirnov [12]. The reviews by Buckman [13], Esaulov [14] and Andersen [15] give an introduction to more recent research.

Negative ions are more sensitive to correlation effects than isoelectronic atoms or positive ions, since for this member of a sequence the core field is weakest and therefore the masking of the more subtle inter-electronic interaction is reduced. This makes negative ions a critical testing ground for theory since for highly correlated valence electrons the independent particle model ceases to be a valid approximation.

In doubly excited states, where an extra electron moves in the field of an excited atom, the strength of the interaction between the two electrons becomes comparable to the weakened interaction of each electron with the core. Under these conditions it is possible to study the dynamics of electron-electron correlation.

Most of the methods currently used to investigate negative ions are based on the interaction with narrow bandwidth laser light [15]. Other powerful methods involve the scattering of electrons on a neutral atom target. Weakly bound negative ions can also be studied with field detachment in electric or magnetic fields. In electron scattering experiments resonances due to transient negative ion states and thresholds appear as prominent structures in the scattering cross section. This method allows one to cover large energy regions but suffers from a relatively limited resolution of roughly 10 meV.

In field detachment experiments [16, 17] typically a fast ion beam is exposed to an electric field. Negative ions with binding energies of some tens of meV can be studied with this method. A resolution of a few meV is realistic.

Photodetachment [18] is another powerful technique to study negative ions. Both products, the neutral atom and the photo-electron, of the photodetachment can be detected. This leads to two principal methods: Photo-electron spectroscopy [19], where the outgoing electron is registered, and neutral particle detection, where the number of produced atoms is counted.

In laser photo-electron spectroscopy a photon detaches an electron from the negative ion and the energy of the escaping electron is monitored. This permits one to determine the state in which the residual atom is left, thus making it a channel specific method. If, in addition, angular resolved experiments are performed, then the state of the outgoing electron can be, apart from the spin orientation, fully registered. The most severe limitation of the method is the resolution that typically

never exceeds 10 meV. Photo-electron spectroscopy is usually performed with the laser beam perpendicularly intersecting the ion beam.

Laser photodetachment with neutral particle detection gives a very high resolution, especially if applied in a collinear geometry. Thus far, most very precise electron affinity determinations have been made with this method [20, 21]. Several such measurements are presented in this thesis.

Recently this versatile method has been made channel specific by selectively detaching the residual atom using resonance ionisation [22, 23]. This combination of collinear interaction and selective detection is rapidly becoming a standard tool for negative ion investigations, since it offers high sensitivity, resolution and selectivity. The method has been developed by us at the Department of Atomic Physics in Göteborg [23] and, independently, in the research group of T. Andersen at Aarhus University in Denmark [22]. Several experiments presented in this thesis have been performed using this new method.

Other accelerator based methods have also been developed [24]. The group of T. Andersen in Aarhus, for example, has performed several experiments in a storage ring for negative ions. This offers the possibility of Doppler tuning. By monitoring the stored current they are also able to measure the lifetime of metastable negative ions [25].

Experiments on negative ions can also be performed on ions stored in traps [26]. A group at the University of Virginia has done experiments on photodetachment of negative ions in the presence of static magnetic fields [27]. They found interesting periodic modulations in the photodetachment cross section near the threshold.

With high power lasers it is also possible to induce multi-photon processes in negative ions [28, 29]. For instance, excess photon absorption in the photodetachment of Rb^- has been observed [30]. Raman like coupling schemes [31] have been successfully applied to negative ions and the fine structure splitting of Te^- has been determined with this technique [32].

2. Atomic negative ions

In this chapter we briefly introduce some results from the theory of atoms. We begin with a Hamiltonian, which contains, apart from the Coulomb interaction, only the spin-orbit coupling. This can be thought of as resulting from an heuristic derivation or as an approximation of the Dirac equation.

An atomic negative ion is formed when an electron is attached to an atom. The attachment process is discussed in section 2.3. With the exception of nitrogen, the noble gases and the mercury group, essentially all elements form negative ions. Negative ions are genuine atomic systems, and consequently the description is very similar to atoms.

The actual calculations of binding energies, fine structure or excitation energies of negative ions, however, turns out to be a formidable task. For instance the alkali earth metals negative ions are bound with only some tens of meV, which is only a few times 10^{-7} of the total electronic energy. Thus a very high precision has to be attained on the total energy to obtain a good value for the electron affinity.

The Hamiltonian for an atomic multi-electron singly charged negative ion with spin-orbit coupling is [33]

$$\mathcal{H} = \mathcal{H}_0' + \mathcal{H}_1' + \mathcal{H}_2 \quad , \tag{2.1}$$

where

$$\mathcal{H}_0' = \sum_{i=1}^{Z+1} \left(-\frac{\hbar^2}{2m}\nabla_i^2 - Z\frac{q^2}{4\pi\epsilon_0 r_i} \right) \quad , \tag{2.2}$$

$$\mathcal{H}_1' = \sum_{i<j=1}^{Z+1} \frac{q^2}{4\pi\epsilon_0 r_{ij}} \quad , \tag{2.3}$$

$$\mathcal{H}_2 = \sum_{i=1}^{Z+1} -\frac{\hbar^2}{2m^2c^2}\frac{1}{r}\frac{\partial V(r_i)}{\partial r_i}\mathbf{l}_i \cdot \mathbf{s}_i \quad . \tag{2.4}$$

The Hamiltonian $\mathcal{H}_0'$ is the kinetic plus the potential energy of an electron in the potential of a nucleus with a charge Z, the Hamiltonian $\mathcal{H}_1'$ is the mutual electrostatic repulsion among the electrons, and finally Hamiltonian $\mathcal{H}_2$ is the spin-orbit coupling in the central field approximation.

In the central field approximation the spherical symmetric part of the Coulomb

repulsion (2.3) $\mathcal{H}_1'$ is added to $\mathcal{H}_0'$ to obtain a one-electron operator $U(r)$,

$$\sum_{i=1}^{Z+1} U(r_i) = -\sum_{i=1}^{Z+1} Z\frac{q^2}{4\pi\epsilon_0 r_i} + \left\langle \sum_{i<j=1}^{Z+1} \frac{q^2}{4\pi\epsilon_0 r_{ij}} \right\rangle \quad , \tag{2.5}$$

where the $\langle\ \rangle$ denotes the spherical average. The new Hamiltonians $\mathcal{H}_0$ and $\mathcal{H}_1$ are:

$$\mathcal{H}_0 = \sum_{i=1}^{Z+1} \left(-\frac{\hbar^2}{2m}\nabla^2 + U(r_i) \right) = \sum_{i=1}^{Z+1} h_{0i} \quad , \tag{2.6}$$

$$\mathcal{H}_1 = \sum_{i<j=1}^{Z+1} \frac{q^2}{4\pi\epsilon_0 r_{ij}} - \left\langle \sum_{i<j=1}^{Z+1} \frac{q^2}{4\pi\epsilon_0 r_{ij}} \right\rangle \quad . \tag{2.7}$$

Now the total Hamiltonian can be written as

$$\mathcal{H} = \mathcal{H}_0 + \mathcal{H}_1 + \mathcal{H}_2 \quad . \tag{2.8}$$

The two limiting cases with

$$\mathcal{H}_0 \gg \mathcal{H}_1 \gg \mathcal{H}_2 \ , \quad \text{or} \quad \mathcal{H}_0 \gg \mathcal{H}_2 \gg \mathcal{H}_1 \quad , \tag{2.9}$$

correspond to LS-coupling and jj-coupling. In all other cases different coupling schemes have to be used [34].

The central field equation is

$$h_{0i}\psi_i = \epsilon_{0i}\psi_i \quad , \tag{2.10}$$

where ϵ_{0i} is the energy eigenvalue of the ith electron. For the ith electron the one-orbitals can be expressed as the product of a radial function R_{nl}, an angular function Y_{lm}, and a spin function ξ:

$$\psi_i(r_i, \Omega_i) = R_{n_i l_i}(r_i) Y_{l_i m_i}(\Omega_i) \xi_{m_{s_i}}(s_i) \quad . \tag{2.11}$$

The eigenfunctions Ψ of the multi-electron equation

$$\mathcal{H}_0\Psi = E_0\Psi \quad , \tag{2.12}$$

are anti-symmetrised products of central field orbitals, or, for brevity, orbitals. The energy eigenvalue of a multi-electron state E_0 is the sum of one-electron energies ϵ_{0i} for the respective configuration. The angular function Y_{lm} and the spin function ξ are identical to the one-electron case. To determine the radial function R_{nl} the Hartree-Fock method can be used. With these one-electron orbitals one can construct N-electron wavefunctions Ψ complying with the Pauli exclusion principle. This anti-symmetrised wavefunction Ψ is usually written as a Slater determinant,

$$\Psi = \frac{1}{\sqrt{N!}} \begin{vmatrix} \psi_1(\lambda_1) & \psi_2(\lambda_1) & \dots & \psi_N(\lambda_1) \\ \psi_1(\lambda_2) & \psi_2(\lambda_2) & \dots & \psi_N(\lambda_2) \\ \dots & \dots & \dots & \dots \\ \psi_1(\lambda_N) & \dots & \dots & \psi_N(\lambda_N) \end{vmatrix} \quad , \tag{2.13}$$

where λ_i is the ith set of spin and spatial coordinates, $\psi_j(\lambda_i)$ a spin orbital, and, j a set of quantum numbers. The parity of such a wavefunction Ψ is given by $(-1)^{l_1}(-1^{l_2})\ldots(-1)^{l_N}$. The distribution of the electrons with respect to n and l is called configuration, and electrons with the same n and l are called equivalent. A multi-configurational wave function is a superposition of several Slater determinants,

$$\Psi = \sum_i c_i \Psi_i \quad . \tag{2.14}$$

The starting points of most calculation are either, for low nuclear charge where $\mathcal{H}_1$ dominates over $\mathcal{H}_2$ (2.9),

$$\mathcal{H}_{\text{a}} = \mathcal{H}_0 + \mathcal{H}_1 \quad , \tag{2.15}$$

or, for high nuclear charge where $\mathcal{H}_2$ dominates over $\mathcal{H}_1$ (2.9),

$$\mathcal{H}_{\text{b}} = \mathcal{H}_0 + \mathcal{H}_2 \quad . \tag{2.16}$$

In both cases the second term of the sum, $\mathcal{H}_1$ and $\mathcal{H}_2$ respectively, is treated as a perturbation to $\mathcal{H}_0$.

The Hamilton operator (2.8) is rotation invariant, the eigenfunctions of $\mathcal{H}$ consequently form a basis of the irreducible representations of the rotation group. The spherical harmonics $Y_{lm}(\Omega)$ in (2.11) constitute such a basis. Furthermore, the Hamiltonian is invariant under the exchange of electrons (exchange of both space and spin coordinates), because electrons are indistinguishable. The eigenfunctions accordingly form a basis to the representations of the permutation group. In compliance with the Pauli principle only the antisymmetric representations, written for example as Slater determinants (2.13), occur for fermions like electrons. The inversion symmetry is reflected by the definite parity of the eigenfunctions of $\mathcal{H}$.

The operator $\mathcal{H}_{\text{a}}$ conserves the total orbital angular momentum $\mathbf{L}$ and the total spin $\mathbf{S}$ in addition to the total angular momentum $\mathbf{J}$, as is expressed by the following commutators:

$$\left[\mathcal{H}_{\text{a}}, \mathbf{L}\right] = 0 \qquad \text{if} \qquad \mathbf{L} = \sum_i \mathbf{l}_i \quad , \tag{2.17}$$

$$\left[\mathcal{H}_{\text{a}}, \mathbf{S}\right] = 0 \qquad \text{if} \qquad \mathbf{S} = \sum_i \mathbf{s}_i \quad , \tag{2.18}$$

$$\left[\mathcal{H}_{\text{a}}, \mathbf{J}\right] = 0 \qquad \text{if} \qquad \mathbf{J} = \mathbf{L} + \mathbf{S} \quad . \tag{2.19}$$

The operator $\mathcal{H}_{\text{b}}$ conserves the total angular momentum $\mathbf{J}$,

$$\left[\mathcal{H}_{\text{b}}, \mathbf{J}\right] = 0 \qquad \text{if} \qquad \mathbf{J} = \sum_i \mathbf{j}_i \quad , \tag{2.20}$$

$$\mathbf{j}_i = \mathbf{l}_i + \mathbf{s}_i \quad . \tag{2.21}$$

The eigenfunctions of $\mathcal{H}_\mathrm{a}$ can also be chosen to be simultaneous eigenfunctions of L^2, L_z, S^2, and S_z, that are written as $|LSM_LM_S\rangle$ plus an additional label that describes for instance the radial part of the wavefunction. It is possible to construct alternative simultaneous eigenfunctions of $\mathcal{H}_\mathrm{a}$ and L^2, S^2, J^2, and J_z. Such functions can be written as $|LSJM_J\rangle$. The eigenfunctions of $\mathcal{H}_\mathrm{b}$ can only be chosen to be simultaneous eigenfunctions of J^2 and J_z, written as $|JM_J\rangle$.

As long as only $\mathcal{H}_0$ is considered, the energy depends only on the sum $n + l$, hence all levels within a configuration are degenerate. In LS-coupling, used in conjunction with $\mathcal{H}_\mathrm{a}$ (2.15), the non spherical part of the Coulomb interaction $\mathcal{H}_1$ (2.7) splits a configuration into terms whose energies depend on L and S. The spin-orbit interaction $\mathcal{H}_2$ (2.4) then splits these terms further into levels whose energies depend of J. In jj-coupling, used in conjunction with $\mathcal{H}_\mathrm{b}$ (2.16), a configuration is first split by the spin-orbit interaction $\mathcal{H}_2$ (2.4) into terms with every possible combination of the individual j values and then by the non-spherical part of the Coulomb interaction $\mathcal{H}_1$ (2.7) into levels. For intermediate nuclear charge values other coupling schemes apply [34], but the resulting levels can always be *labelled* in LS-coupling nomenclature.

On correlation

The troublesome part of the Hamiltonian $\mathcal{H}$ (2.8) is the mutual repulsion $\mathcal{H}_1$ (2.7) among the electrons which induces correlated motion. Yet there is a clear distinction between core electrons and valence electrons. Following Amusia [35] the interaction energy E_int is

$$E_\mathrm{int} = \frac{q^2}{4\pi\epsilon_0\overline{r}} N_\mathrm{Sh} \quad , \tag{2.22}$$

where N_Sh is the number of electrons in a shell and $\overline{r}$ is its mean radius. The mean kinetic energy E_kin is

$$E_\mathrm{kin} = \frac{P^2}{2m} \quad , \tag{2.23}$$

where P is the mean momentum and m the electron mass. If the ratio,

$$\eta = \frac{E_\mathrm{int}}{E_\mathrm{kin}} \tag{2.24}$$

$$= \sqrt[3]{N_\mathrm{Sh}}\frac{\overline{r}}{a_0} \quad , \tag{2.25}$$

is much less than one, the self consistent field dominates. For outer electrons, especially in negative ions, the mean radius $\overline{r}$ can be much larger than the Bohr radius a_0, and thus correlation effects become important or even dominating.

The correlation energy is commonly defined as effects beyond the independent particle model,

$$E_\mathrm{c} = E_\mathrm{exp} - E_\mathrm{HF} - E_\mathrm{rel} \quad , \tag{2.26}$$

where E_{exp} is the experimental energy value, E_{HF} is the Hartree-Fock energy, E_{rel} is the relativistic contribution and E_{c} is called the correlation energy. This correlation energy increases roughly linearly with the nuclear charge Z and is very nearly equal for the iso-electronic positive ion, atom and negative ion [36]. The differences and similarities of atoms and negative ions are further illuminated in the following section.

2.1. Structure of atomic negative ions

Atoms in general have many bound discrete states. Most of the knowledge about atomic systems is based on investigations of the energy position of these bound states. The energy positions are mostly derived from line spectra. Negative ions do not have discrete spectra, owing to lack of bound states, but only a continuum above the photodetachment threshold. This continuum however contains resonance structure due to excited autodetaching states of the negative ion. The short lifetime of these autodetaching states leads to rather broad resonances, limiting the precision and accuracy with which resonance energies can be determined.

Negative ions are fragile quantum systems with some striking properties distinguishing them from other atomic systems such as positive ions and neutral atoms. The higher binding energy of valence electrons in atoms of around 10 eV (figure 2.1), compared to about 1 eV for negative ions, stems from the strength of the Coulomb interaction. The strength of an interaction has no definite relation to its range: there are short ranged very strong interactions, the strong interaction between hadrons, and long ranged very weak interactions, such as gravitation. The binding energy is mainly determined by the strength of the potential, or, loosely speaking, its depth at the origin. From the lower binding energy of H^- we can conclude that the binding potential for the extra electron is relatively shallow.

Another characteristic of atoms and positive ions are the Rydberg series converging on the detachment limit. These series exist as a consequence of the long range nature of the Coulomb potential which, according to Levinsons theorem, supports an infinite number of asymptotic levels. In contrast, the asymptotic potential acting on an electron escaping from a negative ion, figure 2.2, is only the polarisation potential V_{pol},

$$V_{\mathrm{pol}}(r) = \frac{-\alpha_{\mathrm{D}}}{2(r^4 + r_0^4)} \quad \text{with} \quad r \gg r_0 \quad , \tag{2.27}$$

where α_{D} is the dipole polarisability of the atom and r_0 its diameter. This is a short ranged potential that does not support Rydberg series.

In atoms and positive ions the lion's share of the ground state binding energy is described by the independent particle model, and the remaining discrepancy to the correct experimental value is due to electron correlation (2.26). Even atoms have bound doubly excited states with very high correlation, which are poorly described by the Hartree-Fock model. In such states the independent particle model ceases to be a valid approximation.

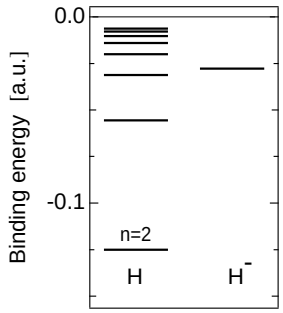

Figure 2.1.: *Binding energies of H and H^-: Energy levels for H and H^- with respect to their ionisation/detachment limits. The ground state binding energies of H, 0.5 a.u., and H^-, approx. 0.025 a.u., differ by roughly one order of magnitude, reflecting the different strength of the binding potential (see figure 2.2). Note also the absence of a Rydberg series for H^- stemming from the lack of a long range asymptotic potential.*

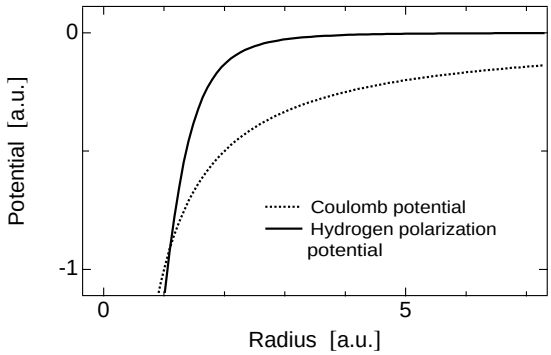

Figure 2.2.: *Asymptotic potentials of H and H^-: The asymptotic Coulomb potential, $V(r) = -1/(r + r_0) \quad r_0 = 18 \times 10^{-6}$ (proton radius), is compared to the polarisation potential* (2.27) *of H, $V_{pol}(r) = -4.5/2(r^4+1)$, with no linear Stark effect.*

For negative ions, sometimes, not even the stability of the ground state can be predicted from an independent particle point of view [37]. The electron correlation effects in negative ions are no longer small corrections, but decisively contribute to the binding energy. Roughly speaking we could view the situation for negative ion binding energies as a shift of orders compared to atoms or positive ions: what is a first order correction for an atom is zeroth order for a negative ion. Hence negative ions are somewhat like a magnifying glass for correlation effects among the outermost electrons. Since these systems are moreover relatively easily accessible to ion-beam-laser experiments, they have attracted a great deal of interest.

2.2. Excited states

Most of the bound excited states in negative ions are fine structure levels [20]. The ones where the configuration is different from the ground state we call electronically excited. In this thesis we will call *all* states above the ground state excited states. Excited states of negative ions can be singly or doubly excited and situated below or above the detachment limit. Only in rare cases, for example platinum and iridium, even electronically excited states are bound [20]. Therefore practically all electronically excited states of negative ions lie above the detachment limit and are consequently autodetaching.

Autodetachment

Since autodetachment is such an important mechanism for the decay of excited states of negative ions I hereby introduce the autodetachment selection rules and outline their physical origin. The treatment closely follows the one given by Brage [38].

Autodetachment can be crudely described as a transition from a discrete state to an adjacent continuum [38] (figure 3.7). This process is induced by a Breit-Pauli Hamiltonian $\mathcal{H}_{\mathrm{BP}}$ [39, 40]. The autodetaching state $\psi(E_0)$ can, in a first approximation, be written as a sum of a discrete state wave function ψ_0 and a continuum wave function ψ_{cont}, representing the open channel,

$$\psi(E_0) = \psi_0 + \psi_{\mathrm{cont}} \quad , \tag{2.28}$$

where E_0 is the energy of the state ψ_0. If we assume Fermi's Golden Rule to be valid, the autodetachment rate ξ is

$$\xi = |\langle \psi_{\mathrm{cont}} | \mathcal{H}_{\mathrm{BP}} - E_0 | \psi_0 \rangle|^2 \quad . \tag{2.29}$$

To calculate this matrix element is the subject of theoretical investigations.

The Breit-Pauli Hamiltonian $\mathcal{H}_{\mathrm{BP}}$ consists of different parts,

$$\mathcal{H}_{\mathrm{BP}} = \mathcal{H}_{\mathrm{NR}} + \mathcal{H}_{\mathrm{RS}} + \mathcal{H}_J \quad , \tag{2.30}$$

where $\mathcal{H}_{\mathrm{NR}}$ and $\mathcal{H}_{\mathrm{RS}}$ are the J independent parts, consisting of non-relativistic and relativistic shift operators, respectively. The operator $\mathcal{H}_J$ consists of the J dependent spin-orbit, spin-spin, and spin-other-orbit operators.

Here we want to compile the relevant selection rules for autodetachment. In all of the subsequent processes parity is conserved. The decay of an autodetaching state can be induced by the Coulomb repulsion or the relativistic terms in the Hamiltonian. The Coulomb interaction conserves orbital angular momentum L, spin S, and the total angular momentum J, and consequently the selection rules for Coulomb autodetachment are $\Delta L = \Delta S = \Delta J = 0$ (table 2.1).

A typical decay time for an autodetaching state is 10 fs. Autodetachment induced by relativistic terms in the Hamiltonian (2.30) are in the order of a factor of α^4 slower than Coulomb autodetachment, but the selection rules are less restrictive (table 2.1). These selection rules hold strictly for LS-coupling only. For other couplings the selection rules on parity π and total angular momentum J still hold, while the others are relaxed.

If a state can decay via Coulomb autodetachment this mechanism will completely dominate, owing to the much higher detachment rate than the relativistically induced decays. A given state that cannot decay via Coulomb autodetachment may have small admixtures, caused by configuration mixing, that couple to the continuum through Coulomb autodetachment. The decay rate induced by these small admixtures is likely to dominate the total decay rate. This mechanism is called induced Coulomb autodetachment.

Table 2.1.: *Autodetachment selection rules: Conventionally if one speaks of autodetachment only the Coulomb autodetachment is meant. In all cases the parity is conserved. The labels SO, SOO mean spin-orbit and spin-other-orbit induced, respectively, and SS stands for spin-spin induced. These names refer to the type of interaction in the Breit-Pauli Hamiltonian* (2.30) *that induces the respective transition [38].*

Quantity	Coulomb	SO, SOO	SS
ΔL	0	0, ± 1	0, ± 1, ± 2
ΔS	0	0, ± 1	0, ± 1, ± 2
ΔJ	0	0	0

Doubly excited states

Among the excited states of negative ions, just as for atoms, we find singly and doubly excited states. The expansion of the exact wavefunction, as obtained from perturbation theory, multi-configurational Dirac-Fock calculations (MCDF) or configuration interaction (CI) calculations, in configurations is usually dominated by one or a few terms. For doubly excited states the analogous expansion contains many configurations with about equal weight. Hence, the state can no longer be meaningfully labelled with one of these configurations. It would be desirable to assign quantum numbers to doubly excited states that reflect the symmetry of a two-electron state.

This goal has been pursued since the discovery of doubly excited states in He [41, 42] and new approximate quantum numbers have been derived. The issue of doubly excited states has not yet been treated in standard textbooks, but there are numerous reviews and articles [43–49] that give a good introduction to the various aspects of doubly excited states. Here we present only one of several possible descriptions. In this K, T scheme [50–59] doubly excited states are labelled,

$$ {}_n(K,T)_N^A \, {}^{2S+1}L_J^\pi \quad , \tag{2.31} $$

with n, N, S, L, π, J having their usual meaning. The quantum numbers K, T and A are specific two electron quantum numbers. They can take the following values:

$$ T = 0, 1, \ldots, \min(L, N-1) \tag{2.32} $$

$$ K = N - T - 1, N - T - 3, \ldots, -(N - T - 1) \tag{2.33} $$

$$ A = \begin{cases} (-1)^{S+T+\pi} & K > L - N \\ 0 & K \leq L - N \end{cases} \quad . \tag{2.34} $$

The quantum numbers K and T are obtained [60, 61] from the decomposition of $SO(4) \otimes SO(4)$ into $SO(4)$ representation and label the so called 'doubly excited symmetry basis'.

These labels are approximate in as much as the symmetry group of two electrons with electrostatic repulsion is only almost $SO(4) \otimes SO(4)$. Physically K and T have

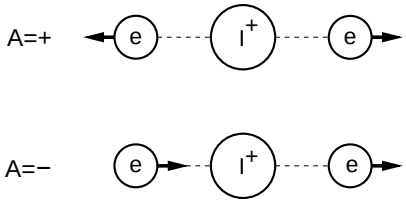

Figure 2.3.: *Significance of A for doubly excited states: If the quantum number A, introduced in section 2.2, has the value + the two electrons vibrate anti symmetrically as depicted in the part (a) and for $A = -$ they stretch symmetrically as indicated in part (b) of the figure. States with A=0 are singly excited.*

the following interpretation [48, 62]: K is proportional to $-\langle\cos\theta_{12}\rangle$, where θ_{12} is the angle between the two electrons with respect to the nucleus, and T measures to what extend the two electron orbits are not coplanar. Both K and T thus describe angular correlation.

The quantum number A was introduced [63] to characterise radial correlation. A value $A = 0$ corresponds to singly excited states, $A = +$ can be envisioned as an anti-symmetric stretching vibration of the electrons with respect to the ion core, see figure 2.3, and $A = -$ as a symmetric stretch. Based on these quantum numbers, approximate selection rules, the propensity rules, for radiative and non-radiative transitions can also be derived [64].

2.3. Formation

To study negative ions requires ways to produce them in sufficient numbers. Even though atomic negative ions in general have a low binding energy they can be formed in a great variety of processes [11]. Here we present only a selection that is related to the experiments performed in this thesis. There are different classes of formation processes: Radiative processes, dissociative processes, three body collisions and electron capture from bound states. Among the radiative processes, radiative attachment,

$$\mathrm{A} + \mathrm{e}^- \mapsto \mathrm{A}^- + \hbar\omega \quad , \tag{2.35}$$

is the time inverse of photodetachment (3.1). The probability for this process, however, is low since it is approximately the ratio of the transit time of a thermal electron to pass an atom, about 1 fs, to the radiation time for a photon, about 10 ns, making it ineffective in the production of negative ion beams of any appreciable intensity. This inefficiency can also be understood as a consequence of angular momentum conservation, since the electron has to hit the atom with an impact parameter in a very narrow range. Another radiative negative ion formation process is the polar photodissociation,

$$\mathrm{A}_2 + \hbar\omega \mapsto \mathrm{A}^+ + \mathrm{A}^- \quad , \tag{2.36}$$

which has been observed for instance for iodine [11].

The low probability of (2.35) increases a lot if a third body participates in the collision. Then the angular momentum balance can be fulfilled in a manifold of different ways. Negative ion creation via three body collisions leads therefore to

much higher cross sections than two body processes. Three body collisions can involve electrons or more massive particles as 'third' body. The latter case usually leads to higher cross sections for negative ion creation. This type of negative ion formation can be fairly efficient in dense gaseous media [12].

In a collision of two neutral atoms the more electro-negative one can capture an electron from the other,

$$\mathrm{A} + \mathrm{B} \mapsto \mathrm{A}^- + \mathrm{B}^+ \quad . \tag{2.37}$$

In negative ion beam experiments often a positive ion beam is charge exchanged in a vapour cell. The charge exchange is a two step process where first the positive ion A^+ is neutralised

$$\mathrm{A}^+ + \mathrm{B} \mapsto \mathrm{A} + \mathrm{B}^+ \quad , \tag{2.38}$$

and then captures another electron,

$$\mathrm{A} + \mathrm{B} \mapsto \mathrm{A}^- + \mathrm{B}^+ \quad . \tag{2.39}$$

Charge exchange is favoured if the electron affinity of A is about equal to the ionisation potential of B. Therefore charge exchange is most efficient for a positive ion beam in an alkali metal vapour [65]. The conversion efficiency is between 0.1 % and 10 %.

Since charge exchange is a scattering process the negative ion beam will have a slightly higher divergence than the initial positive ion beam. In our apparatus, however, this effect is negligible.

3. Photodetachment of negative ions

Photodetachment of negative ions is the process where a photon $\hbar\omega$ detaches an electron e^- from a negative ion A^-:

$$A^- + \hbar\omega \mapsto A + e^- \quad . \tag{3.1}$$

The photodetachment of negative ions exhibits a characteristic threshold behaviour. By virtue of energy conservation a minimum energy of the photon $\hbar\omega$, equal to the electron affinity, is required to detach an electron from the negative ion. More details of this process are discussed in section 3.1. Conservation of parity and total angular momentum lead to the electric dipole selection rules (E1 transitions), that severely restrict the number of accessible final states.

Photodetachment induced by an electromagnetic field can be treated as a small time-dependent perturbation and can therefore be calculated with Fermi's Golden Rule. The pulses delivered by our laser system (section 4.2) are weak in this sense and therefore essentially only induce one-photon transitions. The photodetachment cross section is analogous to the transition probability. Under the mentioned restrictions the photodetachment cross section $\sigma(\omega)$ (in a.u.) for an N-electron ion is given by [66]

$$\sigma(\omega) = \frac{4\pi^2\alpha}{\omega} \int |M_{0\nu}|^2 \, \delta(E - E_0 - \omega) d\nu \quad , \tag{3.2}$$

with the transition matrix element

$$M_{0\nu} = \sum_{q=1}^{N} \int \Psi_0^*(x_1 \dots x_n) e^{-i\boldsymbol{k}\cdot\boldsymbol{r}} (\mathbf{e} \cdot \mathbf{P}_q) \Psi_\nu(x_1 \dots x_N) dx_1 \dots x_N \quad , \tag{3.3}$$

where $E - E_0$ is the energy difference between the initial and final state, ω the energy of the incident light, and ν labels the state of the outgoing electron. The vectors $\mathbf{e}$ and $\mathbf{P}$ are the polarisation of the light and the momentum of the electron respectively. The selection rules for an E1 electric dipole transition ($e^{-i\boldsymbol{k}\cdot\boldsymbol{r}} \approx 1$ in (3.3)) [33] are:

$$\Delta E = \hbar\omega \quad , \tag{3.4}$$

$$\Delta J = 0, \pm 1 \quad \text{and} \quad J_f + J_i \geq 1 \quad , \tag{3.5}$$

$$\Delta M = 0, \pm 1 \quad , \tag{3.6}$$

$$\pi_f = -\pi_i \quad , \tag{3.7}$$

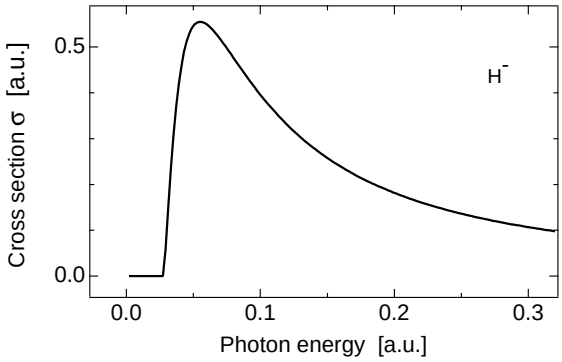

Figure 3.1.: *Analytic model of H^- photodetachment cross section: The photodetachment cross section of an analytical model of H^- given by* (3.8)*. Above the threshold the cross section rises steeply to a maximum at $E = 2E_\mathrm{D}$ and asymptotically falls as $\omega^{-3/2}$ (see section 3.3). This cross section agrees qualitatively with experimental findings.*

where the indices f and i stand for final and initial, respectively.

This photodetachment cross section is a total cross section in as much as no further distinction is made regarding the final atom state on the right side of (3.1). But it is possible to calculate partial cross sections for photodetachment. This means that a specific state of the residual atom, a certain orbital angular momentum of the outgoing electron *and* the coupling of these two angular momenta have to be specified.

In the following sections we first introduce the Wigner threshold law (section 3.1), the various types of resonances (section 3.2), and finally the asymptotic behaviour of the photodetachment cross section (section 3.3). To give a rough idea about the structure of the photodetachment cross section, we present an analytically solvable model negative ion with realistic features, namely the H^- ion with the extra electron bound in a zero range δ-potential [67].

To calculate the photodetachment cross section $\sigma(\omega)$ of this model system three simplifying assumptions are necessary. First, the bound outermost electron is assumed to occupy a hydrogen-like orbital; second, the detached electron is approximated as a plane wave, and finally the binding potential is modelled by an attractive zero range potential $V = -A\delta(r)$. The solution for this model is (in a.u.) [68]:

$$\sigma(\omega) = \frac{16\pi}{3c}\sqrt{E_\mathrm{D}}\frac{\sqrt{(\omega - E_\mathrm{D})^3}}{\omega^3} \quad , \tag{3.8}$$

with E_D being the detachment limit.

This cross section, shown in figure 3.1, has most of the characteristics of photodetachment cross sections: A steep rise of the cross section above the threshold that reaches a maximum at $\omega = 2E_\mathrm{D}$ followed by a slow decrease of the cross section towards higher photon energies. Qualitatively this is the behaviour of the photodetachment cross section of negative ions. In most real negative ions there will be additional structure present. As can be seen in the Li^- photodetachment cross section in figure 3.2(a), calculated by Lindroth [69], this model gives a good general picture of the photodetachment cross section.

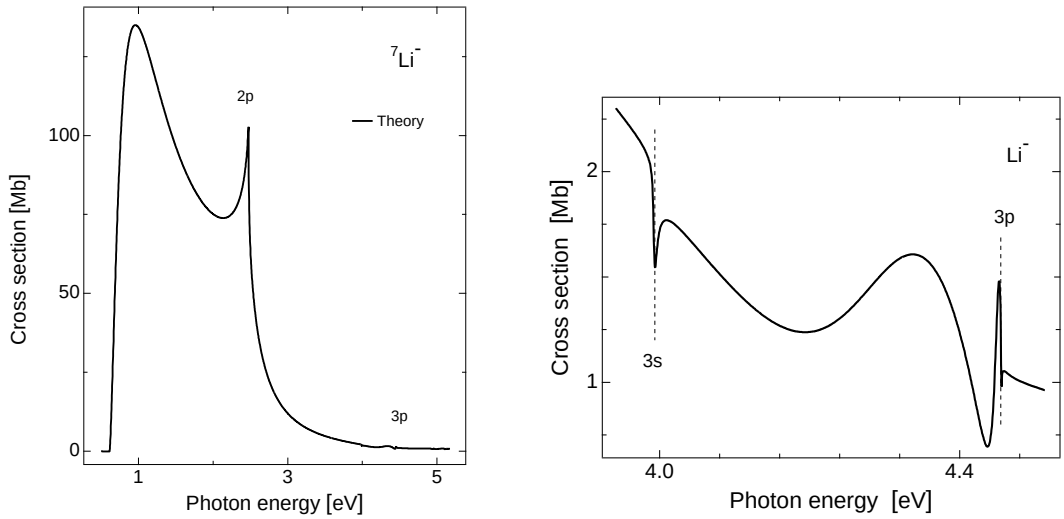

(a) Photodetachment cross section of Li^-.

(b) Magnification at the n=3 thresholds

Figure 3.2.: *Calculated photodetachment cross section of Li^- [69]: Part (a) shows how this cross section qualitatively resembles the analytic model H^- cross section* (3.8) *of figure 3.1, but with additional features at threshold of new detachment channels, resembling the cusp at the Li(2p) threshold. Part (b) shows structures at higher thresholds. They are further discussed in section 6.1.*

3.1. Threshold behaviour

The Wigner threshold law [70] is a general structure in inelastic scattering cross sections. According to this law the energy dependence of the photodetachment cross section $\sigma(E)$ near the threshold is given by

$$\sigma(E) \sim \begin{cases} \left(\sqrt{E - E_j}\right)^{2l+1} & E \geq E_j \quad , \\ 0 & E < E_j \quad , \end{cases} \tag{3.9}$$

where l is the lowest allowed angular momentum in the continuum channel j with a threshold energy E_j. This is valid provided the binding potential $V(r)$ is short ranged so that

$$\lim_{r \to \infty} r^2 V(r) = 0 \quad . \tag{3.10}$$

No resonance should be located at the threshold, because this leads to a modified threshold behaviour [71].

The photodetachment process, in contrast to photo-ionisation, starts with zero cross section at the threshold. In the case of atoms or positive ions the photo-ionisation cross section is non-zero already at the threshold, stemming from continuity with the Rydberg series converging to the ionisation limit, schematically depicted in figure 3.3. The absence of Rydberg series in negative ions, by the same token, leads to zero cross section at the threshold.

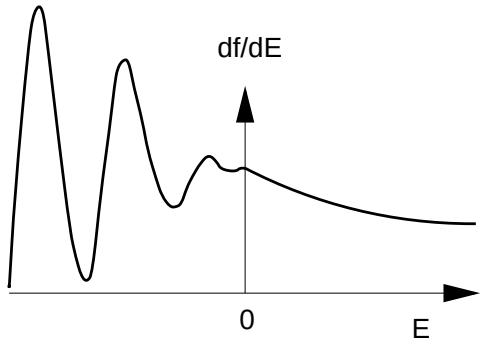

Figure 3.3.: *Schematic oscillator strength across a threshold: To the left of zero the oscillator strength is depicted as measured with a finite resolution. To the right of zero the oscillator strength density is shown.*

We will now sketch the origin of this threshold law as derived from inelastic scattering [72, 73]. Inelastic scattering induces a transition from the initial state of the target particle, here a negative ion, to a different final state. The normalised asymptotic wave function is

$$\psi(\boldsymbol{r}) = \delta_{ji} e^{ik_i z} + \frac{e^{i\boldsymbol{k}_j \cdot \boldsymbol{r}}}{r} f_{j,i}(\Omega) \ , \quad r \to \infty \quad . \tag{3.11}$$

Hence, here

$$k_j = \sqrt{\frac{2\mu(E - E_j)}{\hbar^2}} \tag{3.12}$$

is the asymptotic wavenumber of the outgoing electron in the open channel j and μ is the reduced mass of the electron. The first term in (3.11) is the plane wave incoming along the z-axis (figure 3.4) that represents the incoming particle current, and the second term is the outgoing angularly modulated spherical wave. Most of the plane wave passes the scattering centre forming the so called forward scattered part. The angular modulation $f_{j,i}(\Omega)$ of the spherical wave contains most of the information concerning processes at the scattering centre. Most prominently, the outgoing particle current through a specific solid angle is given by $f_{j,i}(\Omega)$,

$$\frac{d\sigma_{i,j}}{d\Omega} = \frac{k_j}{k_i} |f_{j,i}(\Omega)|^2 \quad . \tag{3.13}$$

The scattering amplitude $f_{j,i}(\Omega)$ is essentially the matrix element for the transition between the final state (3.11) and the incoming plane wave,

$$f_{j,i}(\Omega) = -\frac{\mu}{2\pi\hbar^2} \sum_n \int e^{-i\boldsymbol{k}_j \cdot \boldsymbol{r}'} V_{j,n} \psi_n(\boldsymbol{r}) d\boldsymbol{r}' \quad . \tag{3.14}$$

Here the potential operator $V_{j,n}$ determines the Ω dependence of $f_{j,i}$. To further clarify this point we expand the plane wave and the final state in spherical harmonics. Inserting this in (3.14) and using the orthogonality of the spherical harmonics we

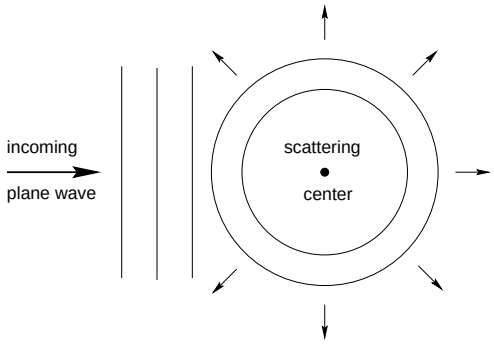

Figure 3.4.: *Scattering geometry: An incoming plane wave from the left is scattered from a scatterer. The scattered part of the wave is an angularly modulated spherical wave* (3.11)*. For clarity the outgoing plane wave is omitted.*

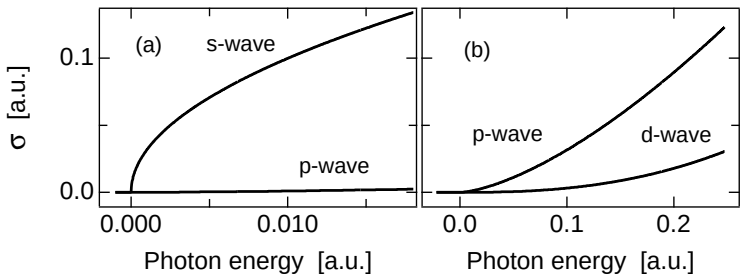

Figure 3.5.: *Wigner threshold law* (3.9)*: In the left graph (a) the photodetachment cross sections for a s-wave and p-wave detachment are compared. The p-wave cross section increases relatively slowly because it starts with zero slope at the threshold. In the right part (b) the p-wave and d-wave cross sections are compared.*

obtain

$$f_{j,i}(\Omega) = -\frac{\mu}{2\pi\hbar^2}\sum_n \int \left[4\pi \sum_{l=0}^{\infty}\sum_{m=-l}^{L} (-i)^l \mathrm{j}_l(\boldsymbol{k}_j\cdot\boldsymbol{r}')(-1)^{-m} Y_{l,m}(\Omega_{k_j})\right] \times V_{j,n}(r)\alpha_{n,l',m'}\delta_{ll'}\delta_{-mm'}dr \quad . \tag{3.15}$$

Herein j_l is a Bessel function, $Y_{l,m}$ a spherical harmonic, and $\alpha_{n,l',m'}$ are the expansion coefficients of the final state. In the vicinity of the threshold, k is small and the Bessel function $\mathrm{j}_l(\boldsymbol{k}_j\cdot\boldsymbol{r}')$ can be approximated as k^l [74] . Close to the threshold all other terms in (3.15) can be considered as constant. To obtain the integrated cross section for inelastic scattering we have to square $f_{j,i}(\Omega)$ and multiply by k_j/k_i, as can be seen from (3.13). This leads to the Wigner law for cross sections $\sigma_{ij}(E)$ at the threshold of inelastic scattering channels (3.9).

Close to photodetachment thresholds usually only the cases $l = 0, 1$, also called s-wave and p-wave, are important. The s-wave has an onset with an infinite slope (figure 3.5) which facilitates a precise determination of the threshold position. All higher orbital angular momenta lead to thresholds with zero slope at the threshold.

The sharp onset of the s-wave detachment cross section is a remarkable feature, and one can question how sharp it can become. In this case there is no limit due to the finite lifetime of excited states, such as for the width of spectral lines. Pho-

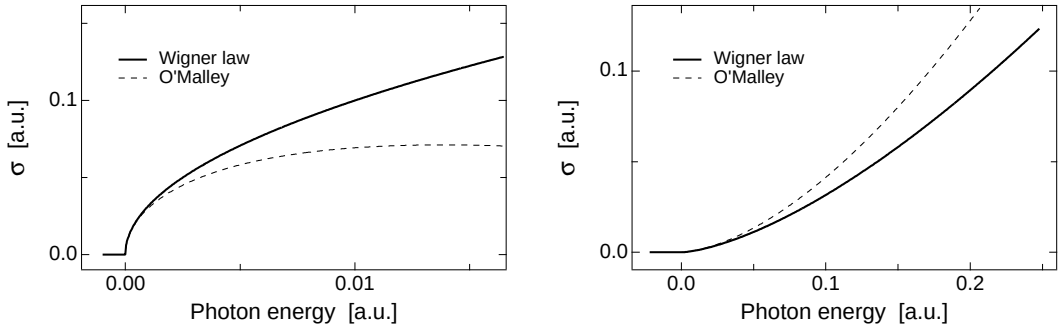

(a) Modified s-wave threshold (b) Modified p-wave threshold

Figure 3.6.: *O'Malleys [75] modification of the Wigner law: O'Malley has calculated a correction* (3.17) *to the Wigner law which accounts for the interaction between the residual atom and the outgoing electron through the polarisation potential* (2.27) *of the atom. The correction is proportional to the dipole polarisability* α_D *of the residual atom, and is here plotted for* $\alpha_D = 10$.

todetachment involves a transition between two *stable* states. Both the initial and the final state have an infinite lifetime, and consequently no width can be associated with it. Only imperfect isolation from the environment, such as stray electric and magnetic fields, cause a 'broadening' of the threshold.

To fit our data we used a function $\sigma_{\mathrm{W}}(E)$ derived from the Wigner law (3.9) that includes a constant background a, an amplitude b, the photon energy E, and a threshold energy E_0:

$$\sigma_{\mathrm{W}}(E) = a + b\left[\sqrt{\frac{|E-E_0|}{2} + \frac{(E-E_0)}{2}}\right]^{2l+1} \quad . \tag{3.16}$$

The two terms under the square root assure that for $E \leq E_0$ the radix is zero. For $E > E_0$ the sum of these terms gives the correct value as in (3.9).

A simple and general law such as the Wigner law is likely to have limited range of validity above the threshold. One restriction is due to the interaction of the outgoing electron with the residual atom through the polarisation potential (2.27). The modification of the Wigner law, depicted in figure 3.6, caused by this interaction has been calculated by O'Malley [75–77] to be

$$\sigma_{\mathrm{OM}}(E) = k^{2l+1}\Big[1 - \frac{4\alpha_{\mathrm{D}}k^2 \ln k}{(2l+3)(2l+1)(2l-1)} + O(k^2)\Big] \quad , \tag{3.17}$$

with

$$k = \sqrt{2E} \quad . \tag{3.18}$$

Farley [78] has proposed an analytic model (called zero core contribution model) to calculate the photodetachment cross section near the threshold, given the core

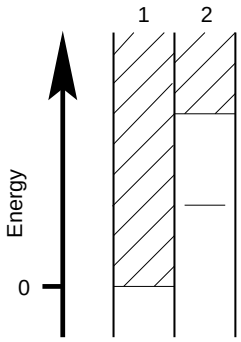

Figure 3.7.: *Two channel level scheme: The discrete level in the closed channel 2 would be stable without the interaction with the open channel 1. Due to this interaction the discrete level may be shifted and broadened. This leads to a continuum structure called Beutler-Fano profile (figures 3.8 and* (3.19)*).*

radius and the electron affinity. With these two numbers as input he succeeds in correctly calculating the photodetachment cross section higher above the threshold than it is possible with the O'Malley [75] form (3.17). The proposed model contains fairly easily accessible parameters and could therefore become an option for the description of measured photodetachment cross section in the vicinity of thresholds.

3.2. Resonance structure

Apart from the overall smooth variation of the photodetachment cross section there occur sharper structures. Some of them are resonances due to autodetaching states of the negative ion, others are Wigner cusps located at the threshold of s-wave detachment channels. Among the resonances it is possible to distinguish Feshbach resonances, due to negative ion states below the atomic parent state, and shape resonances, due to negative ion states bound by a centrifugal barrier above the atomic parent state.

In the simplest analysis the resonance states are assumed to be isolated i.e. well separated in energy from the threshold region and other resonance states. In some cases resonances close to thresholds can be described by modified threshold laws [71, 79, 80]. The simple case of one state being embedded in one continuum leads to the well known Beutler-Fano [81] profile in the total photodetachment cross section.

Here we will first discuss Feshbach resonances, then briefly a situation with two levels embedded in one continuum and thereafter discuss shape resonances and finally introduce Wigner cusps.

The Beutler-Fano profile

A Feshbach resonance is due to an isolated state of a negative ion embedded in one continuum as schematically shown in figure 3.7. The isolated state in channel 2 would be stable without the continuum channel 1 to which it can decay by autodetachment. This model was first investigated by Fano [81]. The structure in the photodetachment cross section owing to this kind of interaction is shown in figure 3.8 and called a Beutler-Fano profile.

In the vicinity of an autodetaching state of the negative ion the total photode-

tachment cross section is given by

$$\sigma_{\mathrm{BF}}(E) = a + bF(q;\epsilon) \tag{3.19}$$

with

$$F(q;\epsilon) = \frac{(q+\epsilon)^2}{1+\epsilon^2} \tag{3.20}$$

where

$$\epsilon = \frac{E - E_0}{\Gamma/2} \quad . \tag{3.21}$$

E_0 is the resonance energy, Γ the width, q the shape parameter, E the photon energy, a a background and b the amplitude of the resonance structure.

This formula (3.19) only strictly applies for an isolated state embedded in one continuum. An isolated state embedded in several continua can be described by (3.19) if all but one continuum contribute only to a non-resonant background, accounted for by the parameter a in (3.19). The Beutler-Fano model is suited only to describe total cross sections.

The Beutler-Fano profile is also used with a different parametrisation involving a correlation parameter ρ^2 with a value between 0 and 1,

$$\sigma_{\mathrm{BF}}(E) = \sigma_0\big[(1-\rho^2) + \rho^2 F(q;\epsilon)\big] \quad , \tag{3.22}$$

with σ_0 being the background cross section. The Fano parameters ρ and q can be expressed in terms of transition matrix elements as, for instance, in [82].

Another, parametrisation has been suggested by Shore [83],

$$\sigma_{\mathrm{Sh}}(E) = \sigma_0 + \frac{A\epsilon + B}{1+\epsilon^2} \quad . \tag{3.23}$$

The parameters A and B are called the Shore parameters and σ_0 is a constant accounting for a non-resonant background.

The unsatisfactory situation of only having a description for resonance structure in the total cross section was resolved by Starace [84]. He addressed a model with one level coupled to two continua. The cross section σ_{SF} then is,

$$\sigma_{\mathrm{SF}}(E) = \frac{\sigma_0}{1+\epsilon^2}\Big\{\epsilon^2 + 2\big[q\Re(\alpha_\mu) - \Im(\alpha_\mu)\big]\epsilon + \big[1 - 2q\Im(\alpha_\mu) - 2\Re(\alpha_\mu) + (q^2+1)|\alpha_\mu|^2\big]\Big\} \quad , \tag{3.24}$$

in which σ_0, ϵ and q retain their meaning as in the Beutler-Fano model (3.20) and the new complex parameter α_μ describes the branching into the different channels.

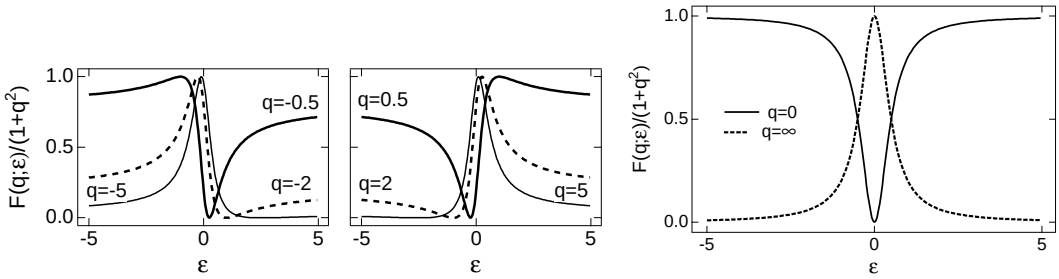

(a) Asymmetric Fano profiles (b) Symmetric Fano profiles

Figure 3.8.: *Beutler-Fano profile: Normalised Beutler-Fano profiles* (3.22) *for various q values. The curves for q and $-q$ are mirror images of each other, as shown in part (a) of the figure, and the profile becomes a symmetric Lorentzian line in the limit of $q = 0$ and $q = \infty$, as can be seen in part (b) of the figure.*

The appearance of all these parametrisations suggests a generalisation, given for example in [82], to a Lorentz line times a quadratic polynomial in ϵ,

$$\sigma_{\mathrm{P}}(E) = \sigma_0 \frac{C_1 + C_2\epsilon + \epsilon^2}{1+\epsilon^2} \quad . \tag{3.25}$$

The aforementioned parametrisations are all special cases of this one with

$$C_1 = 1 + \frac{B}{\sigma_0} \ , \qquad B = \sigma_0(C_1 - 1) \quad , \tag{3.26}$$

$$C_2 = \frac{A}{\sigma_0} \ , \qquad A = \sigma_0 C_2 \quad , \tag{3.27}$$

for the Shore form (3.23), and

$$\begin{aligned} C_1 = \ & 1 - 2q\Im(\alpha_\mu) - 2\Re(\alpha_\mu) \\ & + (q^2+1)|\alpha_\mu|^2 \quad , \end{aligned} \tag{3.28}$$

$$C_2 = 2q\Re(\alpha_\mu) - 2\Im(\alpha_\mu) \quad , \tag{3.29}$$

for the Starace-Fano form (3.24), and

$$C_1 = \rho^2 q^2 + 1 - \rho^2 \ , \qquad q_{1,2} = \frac{C_1 - 1}{C_2} \pm \sqrt{\frac{(1-C_1)^2}{C_2^2} - 1} \quad , \tag{3.30}$$

$$C_2 = 2\rho^2 q \ , \qquad \rho^2 = \frac{C_2}{2q} \quad , \tag{3.31}$$

for the Beutler-Fano from (3.22). Hence, the Beutler-Fano and the Shore parametrisation are *not* equivalent and the latter form has been used in this work since it applies to resonance structure in partial as well as total cross sections. From a fit of the generalised parametrisation (3.25) the parameters of the Beutler-Fano (3.22) and Shore form (3.23) can be obtained from (3.30)(3.31) and (3.26)(3.27) respectively.

A resonance that properly has to be described with the theory of Starace [84] can also be fitted with the generalised form (3.25), as (3.28) and (3.29) reveal, but from the obtained parameters σ_0, C_1, C_2, E_0, and Γ, it is not possible to extract α_μ, thus these two forms are not equivalent. They refer to different physical systems, but nonetheless the width Γ and the energy E_0 are properties of the underlying negative ion state, and consequently *not* depending on the parametrisation.

More complicated systems with more than one level embedded in one continuum lead to a much richer and complex continuum structure. To illustrate this we present here a situation with two closed channels (number 2,3 in figure 3.9(a)) interacting with an open one, number 1.

This model is treated in [85], and here we only present the results, in graphical form. The graphs in figure 3.9 should be understood as follows: the positions of the discrete states in part (b) are *nominal* positions disregarding the interaction with the continuum. These nominal positions are also indicated by the vertical dashed lines in part (b). The coupling of these levels to the continuum leads to new eigenstates and eigenenergies of the extended system. The cross section of this coupled system is given by the solid line in the figures of part (b). Two different situations are shown: one where the two levels are well separated, and a second below where the two levels are close together. The first situation leads to a broad and narrow resonance structure, both of them well away from their nominal position without the coupling to the continuum. The two resonances share their width, or in other words, the sum of their widths is equal to the sum of the individual level width, but here one resonance carries almost all width while the other is very narrow. The second situation gives rise to one narrow Beutler-Fano profile that cuts into another broader one.

Shape resonances

This type of resonances can occur in attractive potentials with a centrifugal barrier. The attractive asymptotic polarisation potential V_{pol} (2.27) with a repulsive centrifugal term has a maximum V_{max} [86],

$$V_{\mathrm{max}} = \frac{(l+1/2)^4}{8\alpha_{\mathrm{D}}} \quad , \tag{3.32}$$

in atomic units, α_{D} denoting the atomic dipole polarisability. Any shape resonance must be situated below V_{max}. The width of shape resonances is usually about equal to the excess energy above the parent state. This is confirmed by a model calculation [87] for a potential V_{Shape} (in a.u.),

$$V_{\mathrm{Shape}} = -V_0 e^{-r^2} + \frac{l(l+1)}{2r^2} \quad . \tag{3.33}$$

Width and energy of a shape resonance in this potential for two different values of V_0 are shown in figure 3.10.

Wigner cusps

A Wigner cusp is not a resonance but a discontinuity in the scattering cross section at the threshold of an s-wave continuum. They can appear in four different variants,

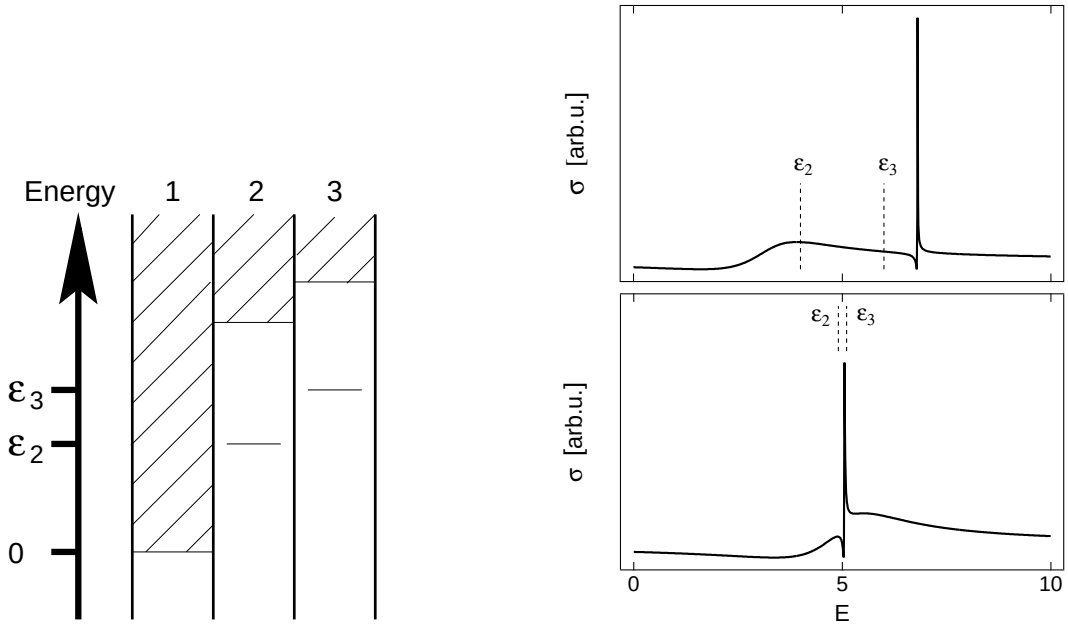

(a) Three channels (b) Photodetachment cross section

Figure 3.9.: *Three channel photodetachment model: The two closed channels 2,3 interact with the one open channel 1, as depicted in part (a). This leads to similar effects as for two channels but with a richer structure. In the upper part of (b) the two levels are well separated (ϵ_2=4,ϵ_3=6) and give rise to a broad and very narrow resonance. In the lower part of (b) the two levels are close together (ϵ_2=4.9, ϵ_3=5.1), resulting in a narrow Beutler-Fano profile cutting into a broader one.*

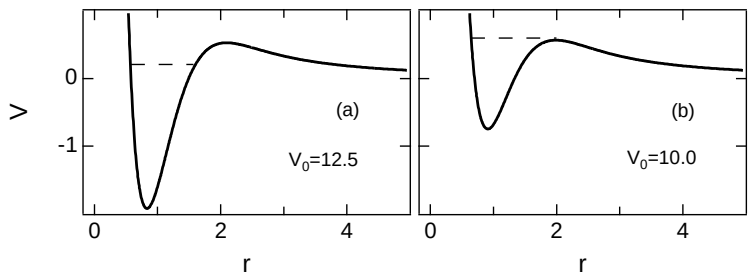

Figure 3.10.: *Shape resonance model: In a binding potential with a repulsive centrifugal barrier* (3.33) *states with positive energy can exist, but they decay by tunnelling through the barrier. The width* Γ *of a shape resonance increases as the energy* E *of the state. In the left part (a) the energy* $E = 0.21$ *and* $\Gamma = 0.06$*, whereas in the right part (b)* $E = 0.6$ *and* $\Gamma \approx 0.5$ *[87].*

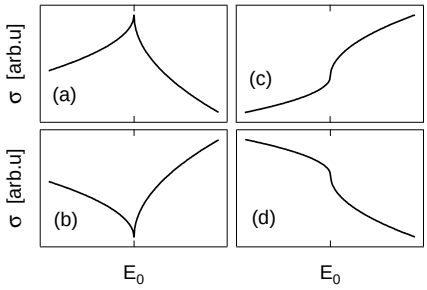

Figure 3.11.: *Wigner cusp: The four possible shapes of cusps* (3.34) *that occur at the threshold of a new ϵs continuum. The upward one (a) has been observed in [88] at the Li(2p) threshold in figure 3.2(a), and a downward one (b) at the Li(3p) threshold shown in figure 3.2(b).*

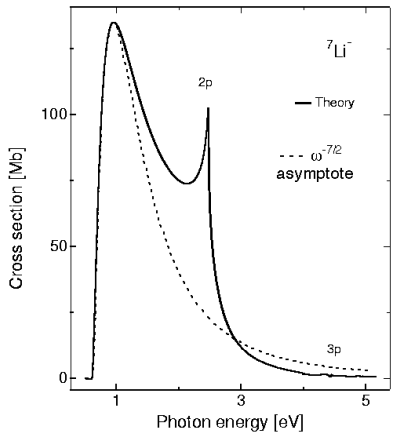

Figure 3.12.: *Asymptotic photodetachment cross section: The Li⁻ photodetachment cross section, calculated by Lindroth [69] is compared to a* $\omega^{-7/2}$ *asymptote.*

all shown in figure 3.11, with the common feature of an infinite slope at the threshold energy E_0. The cross section σ_{cu} near a Wigner cusp can be parametrised as

$$\sigma_{\mathrm{cu}} = 1 \pm G\sqrt{\frac{E_0 - E}{2} + \frac{|E_0 - E|}{2}} \pm H\sqrt{\frac{E - E_0}{2} + \frac{|E - E_0|}{2}} \quad . \tag{3.34}$$

E is the photon energy, E_0 the threshold energy and G and H are constants describing the amplitude on either side of the cusp. The cusps in figure 3.11 have $G = 0.57$ and $H = 1$.

3.3. Asymptotic behaviour

The asymptotic decrease of the photodetachment cross section is due to dwindling overlap of the initial and final state wave function. The higher the excess energy of the detached electron is, the more rapid its wave function oscillates. Since the initial state is fixed, the overlap is given by the product of this function with the ever more rapidly oscillating function of the outgoing electron.

The model cross section for H^- (3.8) drops like $\omega^{-3/2}$ for large ω. For negative ions the asymptotic fall off should theoretically be between $\omega^{-1/2}$ and $\omega^{-7/2}$ [89]. In figure 3.12 we compare the calculated Li^- photodetachment cross section [69] with a modified (3.8) that matches the top and falls off as $\omega^{-7/2}$. In the case of He^- the decay exponent is below the predicted lower limit of $-1/2$.

4. Experimental apparatus

The apparatus used in this work, shown schematically in figure 4.1, consists of two ion sources with independent acceleration stages and a common collinear interaction-detection chamber. Beam handling and the two sources are described in section 4.1. The laser system will be the subject of section 4.2 and the detection system is treated in section 4.3. In section 4.4 we will discuss the data acquisition and processing.

The two different ion sources allow us to produce almost any negative ion. From both sources the negative ion beam is guided into the interaction-detection chamber where the ion beam is either collinearly merged with the laser beam or perpendicularly intersected by the light. This flexibility makes this apparatus a versatile tool for negative ion investigations.

In the collinear geometry laser and ion beams are merged over a 0.5 m long path defined by two 3 mm apertures. This gives a large interaction volume, leading to a high sensitivity. The velocity compression [90] in a fast ion beam reduces the Doppler broadening and thereby enhances the precision. By combining energy positions from measurements with co- and counter-propagating laser and ion beams one can eliminate the Doppler shift to *all* orders. In the collinear geometry, just as in a crossed beam arrangement, it is possible to let the ions interact with more than one laser beam, a possibility that we exploited in the measurements involving state selective detection through resonance ionisation presented in chapter 5.2.

For laser photo-electron spectroscopy it is required to let the laser and ion beams intersect perpendicularly. This beam geometry is also suitable when high light

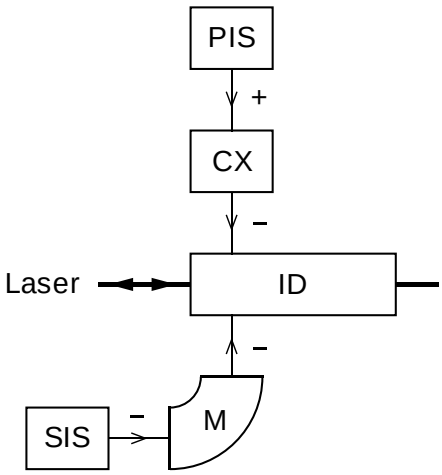

Figure 4.1.: *The ion beam machine: PIS, plasma ion source; CX, charge exchange chamber; ID, interaction-detection chamber; M, sector magnet; SIS, sputter ion source. Velocity filtered positive ions from the plasma ion source (figure 4.3) are charge exchanged in the charge exchange chamber (figure 4.5). The negative ions then enter the interaction-detection chamber (figure 4.11 page 49). Negative ions from the sputter ion source (figure 4.2) are mass selected by the sector magnet and then directed into the interaction-detection chamber.*

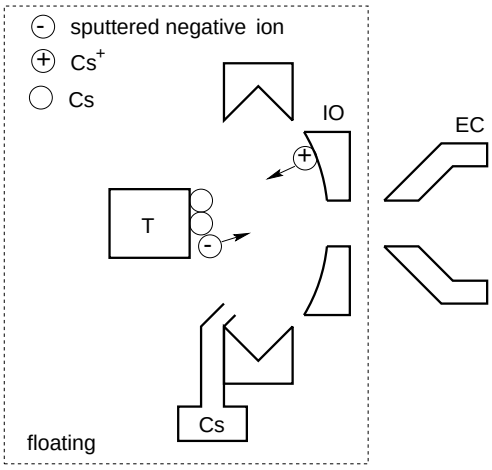

Figure 4.2.: *Sputter ion source: T, sputter target; Cs, cesium reservoir; IO, spherical or helical ioniser; EC, electrostatic extractor. Cesium atoms from the reservoir are ionised on the ioniser and accelerated towards the target on negative potential. On the target Cs^+ ions are neutralised and form a layer on the target. When sputtered atoms pass this layer they pick up an electron. In the field between the target and the ioniser the negative ions are accelerated towards the extractor on ground potential and leave the source [92].*

intensities are necessary to induce nonlinear effects such as multi-photon absorption. In the experiments presented in this thesis none of these options has been used.

4.1. The negative ion beam apparatus

Our negative ion beam machine has two legs (figure 4.1), one starting with a sputter ion source (SIS) and the other one beginning with a plasma ion source (PIS). From the sputter ion source negative ions are extracted directly, whereas from the plasma source positive ions are extracted and charge exchanged to form a negative ion beam.

In the sputter ion source negative ions are produced by accelerating positive cesium ions from the ioniser, shown in figure 4.2, towards the sputter target. The target consists of a heat conducting material that contains the atoms of which we strive to form negative ions. On the targets surface a thin layer of cesium is formed. When target atoms are sputtered they have to penetrate this cesium layer, and upon doing so, an electron can be attached. The negative ion is accelerated towards the extractor and leaves the source. This source can produce micro ampere currents [91] of negative ions from metals with high electron affinities. Metals with lower electron affinities are usually less prolific.

The commercial sputter ion source in our laboratory delivers a beam of about 1 mm diameter with a divergence of approximately 40 mrad. With some ion optics (figure 4.6(b)) it is possible to form a reasonably collimated beam in the interaction region.

The other leg of the ion beam machine starts with the plasma ion source and a charge exchange chamber. From the plasma ion source, figure 4.3, positive ions are extracted from the discharge between the filament and the anode cap. The positive ions are mass selected with a Wien filter, figure 4.4, and directed into a cesium vapour in the charge exchange chamber, figure 4.5.

To run the source with a gaseous medium, like helium, the desired gas is admitted through the hole on the left side in figure 4.3. Through the hole to the right in figure

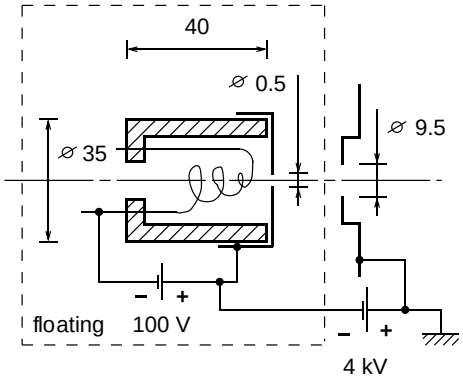

Figure 4.3.: *Plasma ion source: The body of the source is machined in BN_3 ceramics. From the discharge between the filament and the anode cape positive ions are extracted through the hole in the anode. Through the larger hole from the left a charge holder with a compound containing the desired atoms can be inserted. The approximate dimensions are given in mm.*

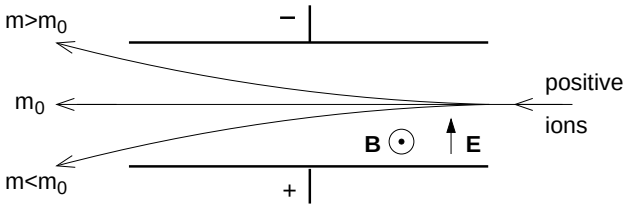

Figure 4.4.: *Wien filter: For singly charged positive ions of mass m_0 the speed dependent Lorentz force is exactly balanced by the electric force on the ion, all others are deflected out of the beam.*

4.3 positive ions are extracted from the discharge between the molybdenum filament (cathode) and the anode plate. To create ions from condensed matter we insert a charge holder, loaded with a compound containing the desired atoms, from the left in figure 4.3 and heat the filament with a current of up to 18 A, to evaporate the compound. A buffer gas, for example nitrogen, is admitted to create a steady discharge. In this discharge most compounds are destructed and we see mostly atomic masses and some very stable dimers, such as N_2.

The extraction, according to the manufacturer, ensues from an area of about 25 μm diameter with a beam divergence of 250 mrad. From this point-like source a reasonably collimated beam can be formed with the relatively simple ion optics shown in figure 4.6(a).

To perform well controlled experiments it is mandatory to create a mass selected beam. The resolution should suffice to separate the desired negative ion from the nearly always present hydrides, with a mass number one higher than the ion. A resolution of 200 is therefore enough. This can be accomplished with Wien filters (also called velocity filter) or sector magnets.

In a Wien filter, figure 4.4, crossed electric and magnetic fields act on the ion. For a parallel beam with uniform speed the required resolution is achieved with a moderate electric field of $\approx 15\ \frac{\mathrm{kV}}{\mathrm{m}}$ and a magnetic field of ≈ 0.1 T. Currently our Wien filter has a resolution of about 50. For the lighter elements this is still good enough. Our sector magnet has a mass resolution of roughly 200 and is therefore well adapted to the heavier negative ions produced by the sputter ion source.

The charge exchange is achieved in a saturated cesium vapour heated to typically 380 K. This is estimated to give a vapour pressure of a few milli Pascal. To optimise the charge exchange we have varied the reservoir temperature and found

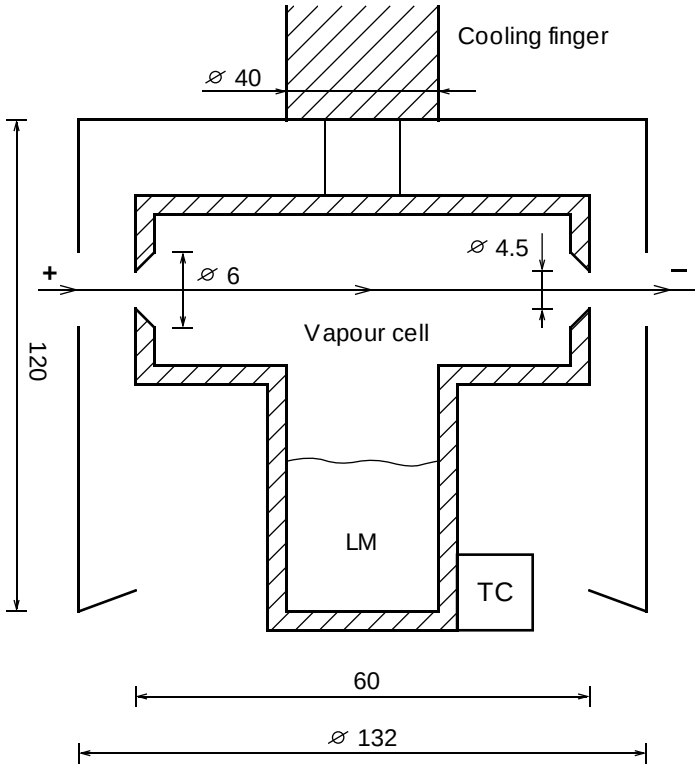

Figure 4.5.: *Charge exchange cell: LM, liquid metal; TC, thermo couple. The mass selected positive ions from the plasma ion source (figure 4.3, 4.1) enter the cesium vapour from the left and leave the cell, with two more electrons attached, as negative ions. The cooled cylinder, mounted on a water cooled finger, around the vapour cell serves to avoid excessive cesium contamination of the vacuum chamber. The approximate dimensions are given in mm.*

the efficiency had become constant above a certain temperature. We interprete this as being due to saturation of the charge exchange process. No investigations of the charge exchange process have been undertaken here. Due to the scattering nature of the charge exchange the beam acquires additional divergence, which we for ^{7}Li with an energy of 4.5 keV estimated to be less than 1 mrad.

To deflect and focus the ion beams there are numerous deflection plates and electrostatic lenses installed in the system, figure 4.6,4.7. The horizontal and vertical deflection plates are used to steer the beam. Thanks to careful alignment of the beam path, using a theodolite, the steering voltages are only a few Volt. The electrostatic quadrupoles, figure 4.7, in the interaction-detection chamber bend the ion beam by 90°. The einzellense in the plasma ion source chamber and in the focusing section are used to maximise the current through the system by appropriately focusing the ion beam. From the sputter ion side a similar system is used, with two differences: the compression lenses are necessary to compensate for the focusing properties of the magnet, and these lenses are also used to steer the beam since they are fed with two independent voltages.

During the design the system has been simulated with a ray tracing program called SIMION [94], to find the right position and strength for the lenses. The lens design follows suggestions given in Hartings book [93] on electrostatic lenses. We have chosen a design that minimises abberations under the geometric restrictions of our system. It has also been estimated which portion of the initial phase space

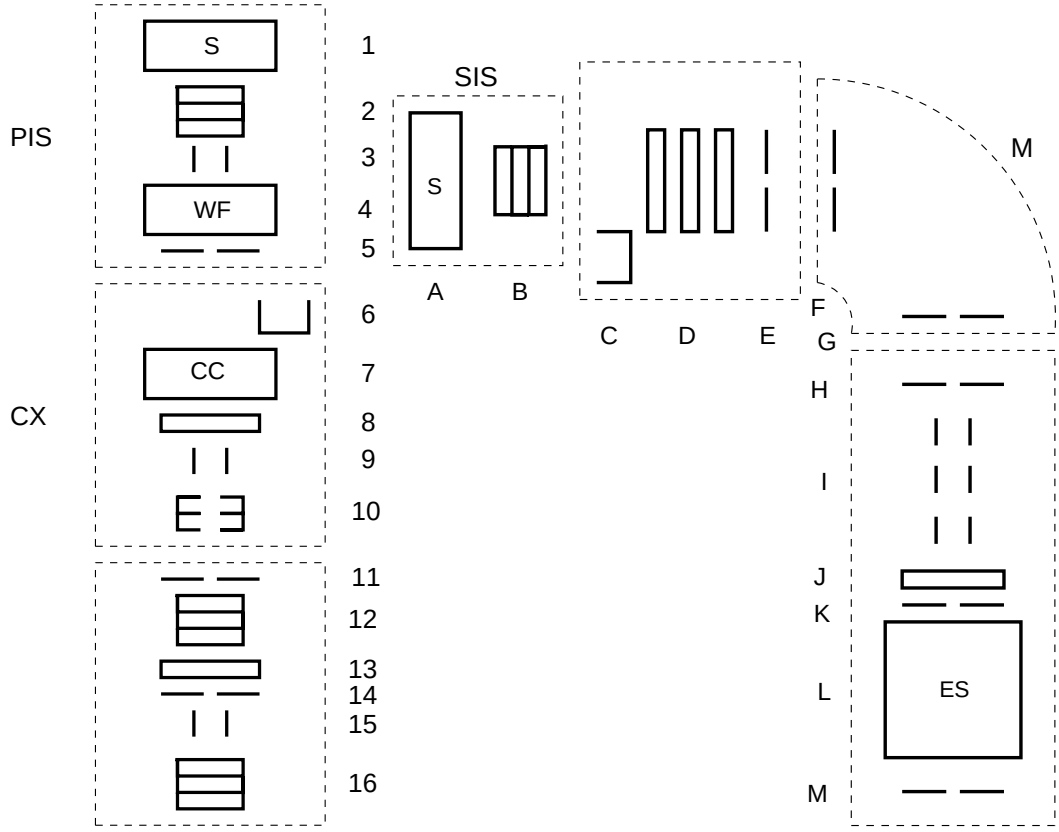

(a) Ion optics in the plasma ion beam line

(b) Ion optics in the sputter ion beam line

Figure 4.6.: *Ion optics in the beam lines: In part (a) there are shown 1, plasma ion source; 2,12,16, einzellense, 3,9,15, horizontal steering plate; 4, Wien filter; 5,11,14, aperture; 6, movable Faraday cup; 7, charge exchange cell; 8,13, vertical steering plate; 10, triple aperture lense after [93]. In part (b) there are shown A, sputter ion source; B, einzellens; C, movable Faraday cup; D,I, cylinder lens; E,F,G,H,K,M, aperture; J, deflection plate; L, electron spectrometer. The compression lens consists of three pairs of plates, the two outer pairs are on ground potential and the middle pair is fed with one voltage per plate to both compress and steer the beam. The electron spectrometer ES will in the near future be moved to place indicated in the figure.*

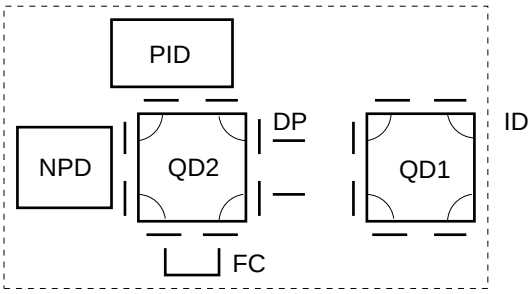

Figure 4.7.: *Ion optics in the interaction-detection chamber: NPD, neutral particle detector (figure 4.11 page 49); PID; positive ion detector (figure 4.11); QD1,QD2, electrostatic quadrupole deflectors; DP, deflection plates. Around the quadrupole deflectors there are apertures. Between the quadrupole deflectors the beam is shielded stray from electric fields by a stainless steel tube.*

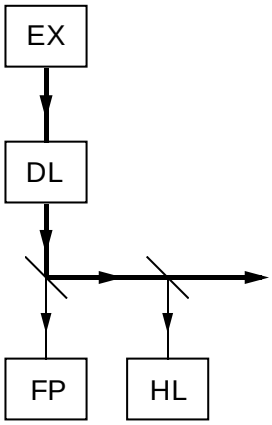

Figure 4.8.: *Laser system overview: EX, excimer laser; DL, dye laser; FP, Fabry Perot etalon; HL, hollow cathode lamp. The wavelengths of the excimer pumped dye lasers is determined by combining an absolute calibration from transitions in the hollow cathode lamp with the frequency markers provided by the fringes of the Fabry-Perot etalon.*

spanned by the ion beam can possibly be transfered into the interaction region [94].

4.2. The laser system

Our laser system consists of two excimer and two dye lasers. Normally one excimer laser pumps one dye laser, as indicated in figure 4.9(b). Each set of excimer plus dye laser can be used individually for high resolution measurements. It is also possible to pump both dye lasers by a common excimer laser as shown in figure 4.9(a).

The XeCl excimer lasers deliver pulses of 15 ns duration with an energy of 100 mJ to 200 mJ and 308 nm wavelength. One of them has a repetition rate of up to 200 Hz and the other one has a maximum repetition rate of 20 Hz. The dye laser pumped with these pulses emit pulses of the same duration and repetition rate with an energy ranging from 1 mJ to 10 mJ, for the fundamental, and 100 μJ to 1 mJ per pulse for the doubled light.

The dye lasers generate tunable light from 800 nm to 330 nm, and 400 nm to 200 nm with frequency doubling. The line width is 20 m^{-1} (6 GHz). By inserting a Fabry Perot etalon in the oscillator beam path of the dye laser the bandwidth can be narrowed to 4 m^{-1} (1.2 GHz).

For experiments involving resonance ionisation the two laser pulses have to be synchronised. This is accomplished by simply pumping both dye lasers by a common excimer laser, as shown in figure 4.9(a).

The wavelength of the laser light is determined by combining an absolute calibration from transitions in the hollow cathode lamp with the frequency markers provided by the fringes of the Fabry Perot etalon. With high contrast Fabry Perot fringes and good hollow cathode lamp lines we can calibrate to a precision of approximately 1 m^{-1}.

The accuracy of a fitted energy position we judge by the statistical scatter of the fitted parameters and by the estimated error of the individual values. Generally the scattering and the individual error bars were, as expected, of comparable size. By combining two measurements with co and counter-propagating laser and ion beams

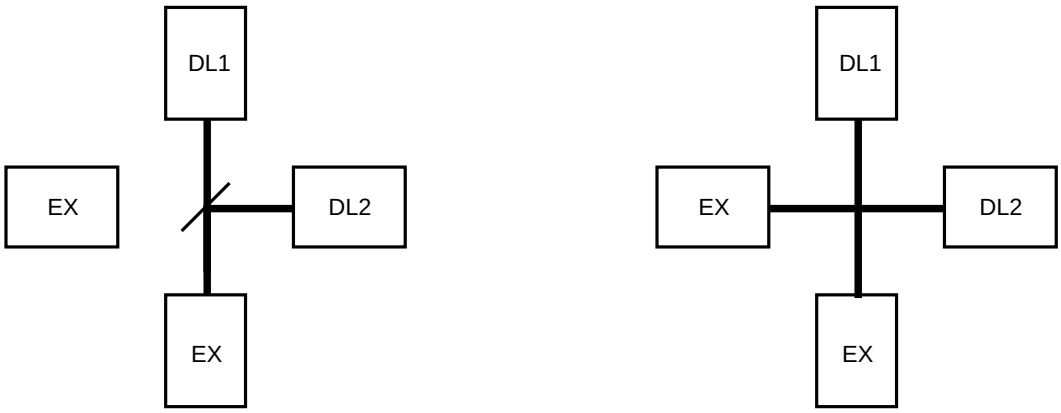

(a) Commonly pumped dye lasers (b) Separately pumped dye lasers

Figure 4.9.: *Laser arrangement: The excimer and dye lasers are placed such that both excimer lasers can pump either one of the dye lasers or both at once. The excimer lasers are placed about 1.5 m from the dye lasers.*

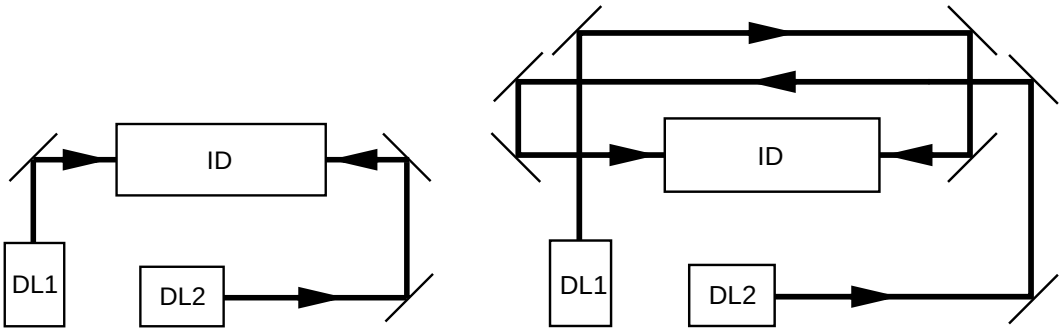

Figure 4.10.: *Two colour laser beam path: In the interaction-detection chamber ID the laser beams are always running opposite to each other. The left part of the figure shows the photodetachment laser beam 1 (from DL1) co-propagating with the the ion beam and the right part counter-propagating. The beam reversal requires some rearranging of optics and cannot be undertaken during a scan.*

one can eliminate the Doppler shift to *all* orders. To obtain these measurements the laser beam(s) have to be reversed. The geometric mean of the two measurements gives a Doppler free value for the measured energy E_0,

$$E_0 = \sqrt{E_0^{\mathrm{r}} E_0^{\mathrm{b}}} \quad , \tag{4.1}$$

if $E_0^{\mathrm{b,r}}$ is the blue- respectively red shifted value for co- and counter-propagating laser and ion beams.

This combining assumes the beam energy, or rather the speed of the ions, to be constant. For a one-laser experiment where the beam reversal is made during a scan this clearly is a valid assumption. For two-laser experiments with reversed beams, shown in figure 4.10, beam reversal typically is performed within the next days. Here the question of stability is far less trivial. The ionisation step ω_2 (figure 5.5) of the state selective excitation scheme is tuned to a Rydberg state, and this transition is used to check our day to day stability of the beam speed. In all cases we found the laser wavelength to still be in resonance after a restart of the beam one or even a few days later. We therefore believe that the above named combination of red and blue shifted value also makes sense if the ion beam has to be restarted to reverse the laser beam.

4.3. The detection system

The detection chamber, figure 4.11, renders four different detection schemes possible: angular resolved photodetachment, laser photo electron spectroscopy, photodetachment with neutral particle detection and photodetachment resonance ionisation spectroscopy with positive ion detection. In all cases particles are counted. Electrons are registered with micro channel plates MCP or channel electron multipliers CEM. Neutral atoms or positive ions are counted with a secondary emission detector (PID,NPD) [95] shown in figure 4.11. In the secondary emission detectors the electrons emitted upon impact of the atom or positive ion on the plate are registered with a CEM.

The pulses from any of the hitherto mentioned detectors are pre-amplified and then counted by a gated photon counter, figure 4.12. This gated detection based on the time structure of the signal, figure 4.13, allows us to exclude all events not originating from the spatial and temporal overlap of laser and ion beams from being counted.

We empirically found the neutral particle and positive ion detectors start to saturate at a count rate cr per pulse of,

$$cr \approx \frac{1}{2}\sqrt{m} \quad , \tag{4.2}$$

with m denoting the mass number of the negative ion in question. The mass dependence is an indirect one, because it is really the mass dependent beam speed for a given beam energy (3 kV to 4 kV) that lies behind this dependency.

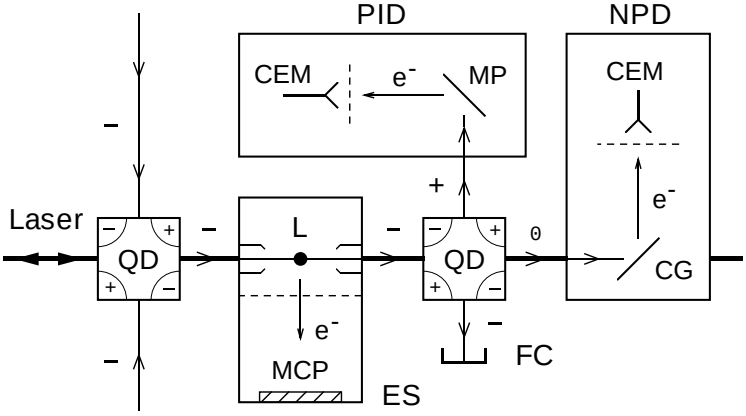

Figure 4.11.: *Interaction-detection chamber: QD, electric quadrupole deflector; PID, positive ion detector; CEM, channel electron multiplier; L, perpendicular laser beam (for electron spectroscopy); MCP, micro channel plate; ES, time-of-flight electron spectrometer; MP, metal plate; FC, Faraday cup; NPD, neutral particle detector; CG, conducting glass plate. Laser and ion beams are coaxially merged over 0.5 m between the quadrupole deflector. For electron spectroscopy* only *the laser beam L perpendicularly intersecting the ion beam is used.*

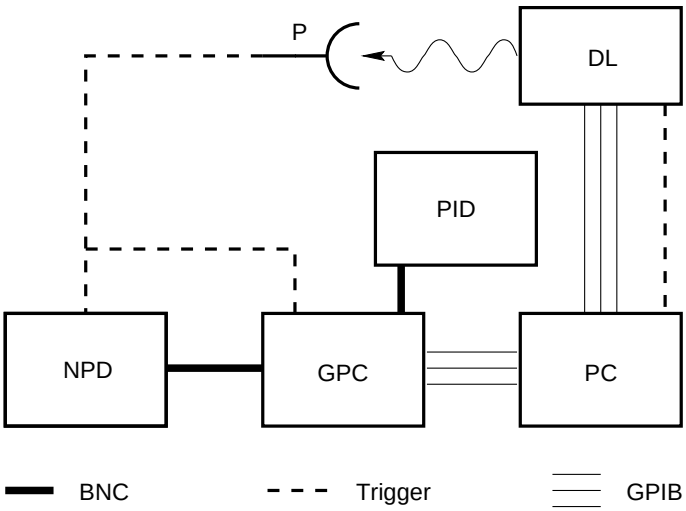

Figure 4.12.: *Logic of the detection system: NPD, neutral particle detector; P, photodiode; GPC, gated photon counter; PID, positive ion detector; DL, dye laser; PC, data acquisition computer; GPIB, general purpose interface bus. The apparatus operates under the control of the PC that sends, via GPIB, a start signal to the dye laser, which then delivers a preset number of pulses without a further start signal. The trigger pulses from the dye laser to the PC are counted to recognise the end of a burst. The neutral particle detector and the gated photon counter are triggered from a photodiode (figure 4.13). The positive ion detector does not need triggering. After a burst of pulses the data from the gated photon counter are transfered via GPIB to the PC. Thereafter a new cycle can start.*

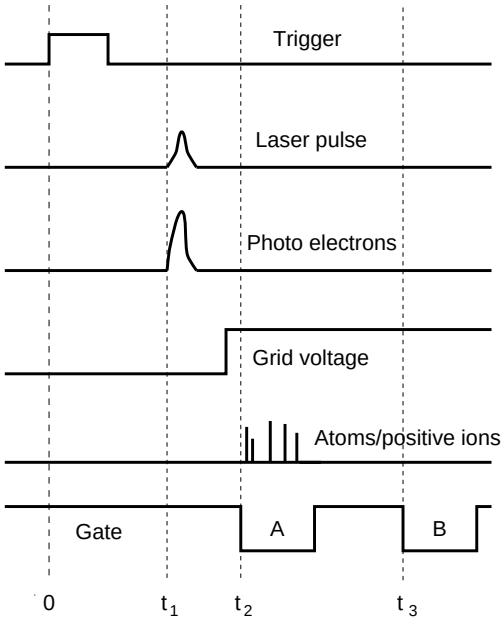

Figure 4.13.: *Time structure of the signal: at the time $t_1 \approx 1\mu s$ after the dye laser trigger, the excimer laser fires and the light pulse almost instantaneously creates photo electrons on the plate of the neutral particle detector (figure 4.11). To prevent the photo electrons from reaching the CEM (figure 4.11) the grid between the plate and the CEM is held at negative potential with respect to the plate. Shortly before $t_2 \approx 2\mu s$ this grid is grounded. At t_2 the gate A of the photon counter starts. The delay $t_2 - t_1$ is the time of flight for the positive ions or neutral particles which arrive first at the detector. The width of gate A and B is equal to the time of flight (≈5 μs) for the 0.5 m length of the interaction region. In gate B we count the background with a delay of $t_3 \approx 40\mu s$.*

It has been estimated that every positive ion or neutral atom created in the interaction region is detected, owing to the very high efficiency of the secondary emission detectors [95]. This makes the apparatus very sensitive and well adapted to measurements on small photodetachment cross section.

The negative ion current is monitored with the Faraday cup FC in the interaction-detection chamber. On the beam path there are several apertures on which a current can be measured. This serves as a valuable aid in adjusting the beam.

The electron spectrometer ES in figure 4.11 is of time of flight type. On the entrance the ion beam is decelerated and focused to improve resolution and signal level. The resolution is about 10 meV.

Angular resolved photodetachment studies can be used to distinguish between different photodetachment channels. A carbon cylinder with approximately radial holes can be inserted in the beam path in the interaction-detection chamber to perform angular resolved photodetachment studies [96]. Neither electron spectroscopic nor angular resolved measurements are presented in this thesis.

4.4. Data acquisition and processing

All data are acquired with a PC and stored in 7-bit ASCII files. The PC controls the whole experiment via GPIB, figure 4.12. A measurement cycle is initiated by a start message to one of the dye lasers. The micro computer integrated in the dye laser then generates a trigger pulse which is shown in the upper trace in figure 4.13. This pulse triggers the excimer laser(s) to emit a pulse at t_1.

Since this time t_1 is subject to a substantial jitter we trigger the rest of the equipment from a photodiode P picking up light from the excimer laser. In this way

we are able to trigger the light related detection of interaction products with a jitter of only ≈0.5 ns, thus reducing fluctuations in the detection. The quality of these trigger pulses is also carefully checked with a fast oscilloscope.

The neutral particle detector is triggered. To avoid overloading the CEM with photo electrons, the grid between the plate, figure 4.11, and the CEM is held at negative potential with respect to the plate. This voltage has to be switched off a few hundred nanoseconds before the first neutral particles from the interaction zone impinge on the plate at the time t_2 in figure 4.13. The photo electrons and neutral particles can be separated because the photo electrons are created on the plate while the neutral particles have to travel about 0.15 m from the interaction region to the detector with a speed of about 100 000 $\frac{\mathrm{m}}{\mathrm{s}}$. The delay time $t_2 - t_1$ is the time of flight for the neutral particles from the interaction region between the quadrupole deflectors QD1,2 to the neutral particle detector NPD.

The photodetachment events are counted during the gate A, as indicated in the lowermost trace of figure 4.13. The width of this gate is equal to the time of flight, about 5 μs, for the 0.5 m long interaction region. The photon counter GPC uses a threshold height for the pulses to discriminate the events caused by neutral particles from noise. To subtract an eventual background of neutral particles due to collisional detachment we count the events in a second gate B with a delay t_2 of about 40 μs.

The positive ion detector PID functions the same way as the neutral particle detector NPD except that this detector is not triggered. We found the effect of laser pulse related disturbances to be so small that no effort for further suppression was made.

After a preset number of laser pulses the number of events counted by the photon counter GPC is transfered via GPIB to the PC where it is recorded in a file. After that a start request is sent to the dye laser and a new cycle may start.

The program has recently been refined [97] and allows now a different step length and pulse number in different parts of the scan. This comes in useful when scans with relatively short data relevant parts are made and in between only the Fabry Perot fringe count has to be kept.

From the PC the data files are transfered to a computer, here Linux/Unix machines, and automatically preprocessed for further evaluation with the program Igor 2.02 on a Macintosh computer. The data files are also archived as `gnuzip`-compressed `tar`-files. All files are graphed for screening and archiving purposes, as shown in figure 4.14(b).

To fit the parameters of the respective functions to our data, we used the Levenberg Marquardt method [98]. This method elegantly interpolates between a more global search for the minimum of χ^2 and a fine local search. The quality of a non-linear fit can depend on the initial values for the fit routine. The graphical interface of Igor allows one to quickly find adequate start values. We found it seldom necessary to hold parameters constant during a fit. In the case of very noisy data we also used a robust fit algorithm that reduces the relative significance of outlier data points described in [98]. When fitting to the photodetachment signal the data were weighted with their inverse error, all other data were fitted with equal weight for

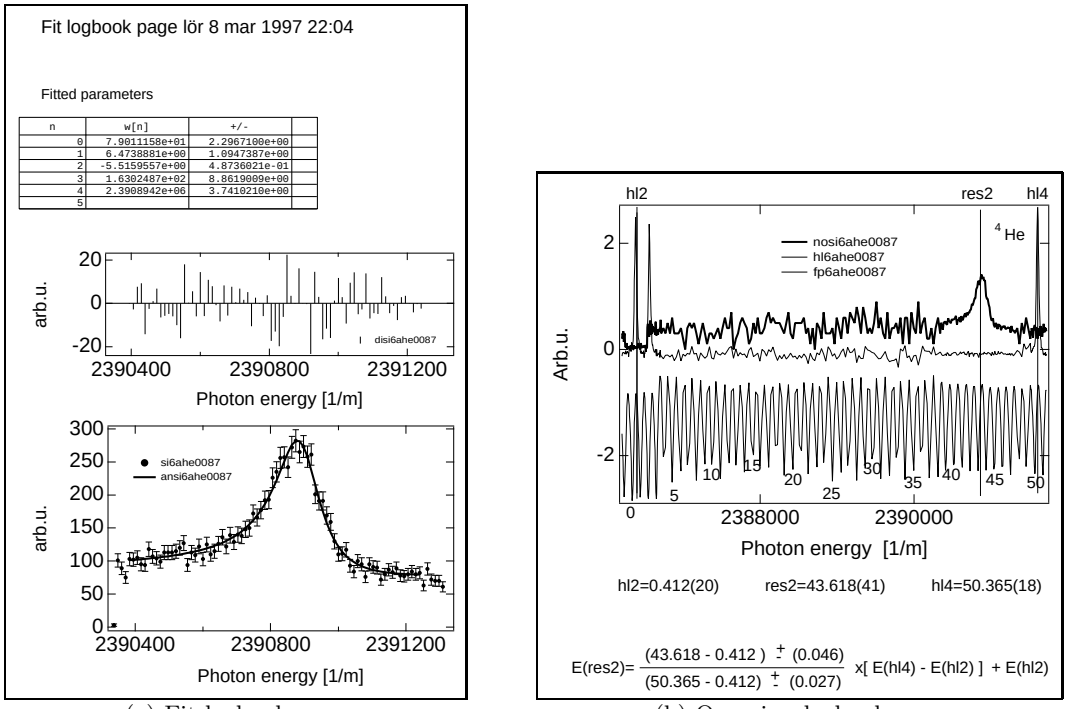

(a) Fit logbook page (b) Overview logbook page

Figure 4.14.: *Logbook pages: The logbook page (a) is archived for every fit containing the parameter values, their uncertainty, the data with the best fit, and, the fit residuals to roughly judge the quality of the fit. Part (b) shows, from top to bottom, the signal per laser pulse, the hollow cathode lamp signal and the Fabry Perot fringes. This page is used to screen the data and to collect the fitted parameters. The positions of* hl2, res2 *and* hl4 *are given in Fabry Perot fringe numbers, which together with the energy values for the calibration lines, give the calibrated position of the Doppler shifted resonance.*

all points. When the data are weighted with their inverse error then χ^2 also has an absolute meaning and can be used to judge the statistical quality of the data. Of all fits a logbook page is printed and archived, as shown in figure 4.14(a)

There is no straight forward way of obtaining reliable errors for the fitted parameters [98]. The uncertainties given by the routine are the square root of the diagonal elements of the correlation matrix. These values we use as guideline in estimating the error bars. Always a serious attempt is made to have sufficient statistics to also judge the statistical scatter of the fitted parameters. Usually both error estimates give comparable results.

5. Threshold studies

The most accurate methods to determine the electron affinity of atoms is to measure the threshold energy for the photodetachment process [20]. Especially for s-wave threshold this gives very accurate results owing to the very steep onset of the photodetachment cross section. Here we present one classical photodetachment threshold study on tellurium and an electron affinity measurement on lithium with a novel state selective method.

Neutral particle detection is a well developed method and has been demonstrated to be very sensitive and accurate [15, 99–102]. In spite of some limitations, we attained a result for the electron affinity of tellurium, that ranks among the most accurate electron affinities of the periodic system [21]. To reach this level of accuracy we paid special attention to a reliable absolute calibration, which we ensured by using two completely independent sets of calibration lines in two different hollow cathode lamps. The measurement is presented in section 5.1.

The measurement of the tellurium electron affinity is almost a textbook example: an easily accessible s-wave threshold in an element of which the sputter ion source efficiently produces negative ions.

With the affinity measurement on lithium, presented in section 5.2, we mainly intended to demonstrate a new state selective detection scheme. The state selectivity is accomplished by resonance ionisation of the residual atom of the photodetachment process. This new method is introduced here and in the subsequent experiment we assume familiarity with its principles. The emphasis for this experiment was to demonstrate the feasibility of the scheme and to explore its potential. We found this technique to work very well and were able to improve the accuracy of the lithium electron affinity by an order of magnitude.

5.1. Tellurium electron affinity

Previous to this measurement [103] the electron affinity of tellurium was known to have a poor precision compared to other elements with similarly high electron affinities. We aimed to improve this value, by determining the Doppler free photodetachment threshold position by studying the process:

$$\mathrm{Te}^-(5\mathrm{p}^5\,{}^2\mathrm{P}_{3/2}) + \hbar\omega \mapsto \mathrm{Te}(5\mathrm{p}^4\,{}^3\mathrm{P}_2) + \mathrm{e}^-(\epsilon\mathrm{s}) \quad . \tag{5.1}$$

Close to the threshold the s-wave detachment dominates over the also allowed d-wave detachment (figure 3.5). As can be seen in figure 5.1, there is additional contribution

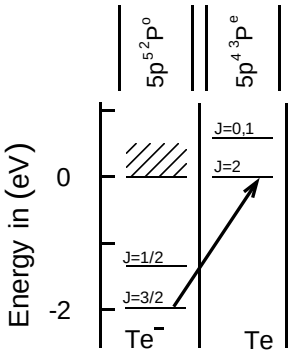

Figure 5.1.: *Tellurium excitation scheme: Selected states of Te/Te$^-$. The arrow indicates the transition induced in this experiment.*

Table 5.1.: *Tellurium calibration lines: Transition energy of the calibration lines used in this experiment. We calculated the neon transition energies from the tabulated level energies. The Ar transition energies are calculated from the levels presented in Tab* V *of [104]. The levels are designated in Paschen notation.*

Element	Transition	Line (m^{-1})
Ne [105, 106]	$2p_2 \rightarrow 4d_6$	1 592 921.6(4)
Ne [105, 106]	$2p_5 \rightarrow 3s_2$	1 588 439.6(6)
Ar [104]	$2p_6 \rightarrow 5d_4$	1 592 259.8(5)
Ar [104]	$2p_2 \rightarrow 5s_1''$	1 587 650.8(5)

to the neutral atom count rate due to the processes:

$$\mathrm{Te}^-(5p^5\,{}^2P_{1/2}) + \hbar\omega \mapsto \mathrm{Te}(5p^4\,{}^3P_{0,1,2}) + e^- \quad . \tag{5.2}$$

The contribution of these processes to the signal, however, varies slowly with the photon energy since they are far above their thresholds. Furthermore, these signals are relatively small since the sputter ion source predominantly produces ground state negative ions.

The light pulses with 10 μJ were generated by one of our excimer pumped dye lasers operating with Rhodamine 6G. We calibrate with four lines from neon and argon given in table 5.1.

For the data acquisition we used a newly written program [97]. It allows to divide a scan into several parts of which each has its individual step length and pulse number per step. It is possible to increase the data quality on the short stretches where the investigated structure is located. In between only the Fabry-Perot fringe count has to be kept, which is attainable with less laser pulses and more sparse data points. Compared to a whole scan at full resolution we reduced the scan time by about a factor of ten. An example of such a scan is given in figure 5.2.

A typical measurement is shown in figure 5.3. To obtain the photodetachment threshold energy E_0 we fitted (3.16) to the data and took the geometric mean of the fitted blue and red shifted thresholds as described in (4.1). The average threshold

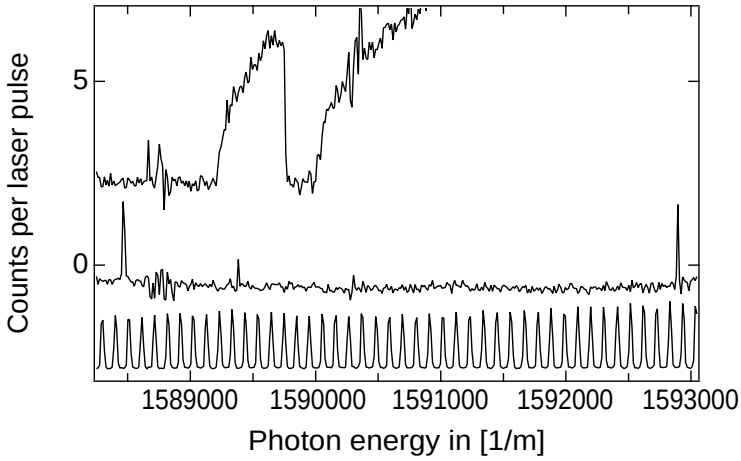

Figure 5.2.: *Tellurium scan overview: The three curves show the photodetachment signal, the reference lines (Ne) and the Fabry-Perot fringes. In the photodetachment signal, the left threshold is obtained with counter-propagating laser and ion beams and the right threshold with co-propagating beams. The background is partly due to photodetachment of the* $Te^-(5p^5\,{}^2P_{1/2})$ *state. The signal saturates at about 7 counts per laser pulse. In the vicinity of the calibration lines and the photodetachment thresholds the step-length was 1 pm and 100 shots per point were taken. Elsewhere the step-length was 5 pm and 10 shots per point were taken. The vertical scale (Counts per laser pulse) is only valid for the photodetachment signal.*

Table 5.2.: *Tellurium electron affinity: Comparison of the different measurements. The value in* m^{-1} *is only given if the publication contains the value.*

Author	Affinity in m^{-1}	Affinity in meV
Slater (1977) [107]		1970.8(3)
Thøgersen (1996) [32]	$1.589\,69(4)\times10^6$	1970.965(50)
This work (1996) [103]	$1.589\,618(5)\times10^6$	1970.876(7)

energy E_0 is

$$E_0 = 1\,589\,618(5)\ \mathrm{m}^{-1} \quad . \tag{5.3}$$

There are two major contributions to the uncertainty of E_0. There is a statistical error of 1 m^{-1} corresponding to the spread of fitted threshold values. Second, there is an uncertainty related to the laser intensity profile. We have estimated this uncertainty by analysing the Fabry-Perot fringes and the atomic reference lines to be less than 4 m^{-1}, which is one fifth of the laser frequency bandwidth.

In figure 5.4 we compare our electron affinity with other measurements. The affinity from [32] is not the main result but a "windfall profit" from fine structure measurements on Te^-. The numerical values are presented in table 5.2.

We have shown that the background contribution from photodetachment of

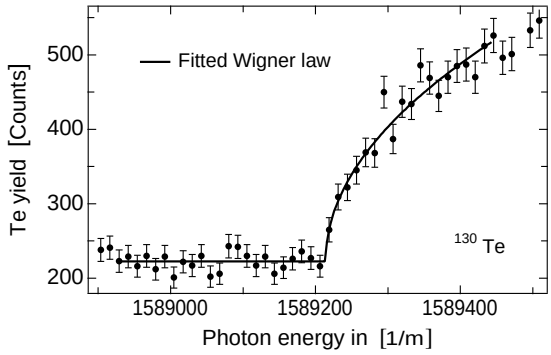

Figure 5.3.: *Te($5p^4$)+ϵs threshold: Measurement of the relative photodetachment cross section near the Te($5p^4$)+ϵs threshold with counter-propagating laser and ion beams. The solid line is a fit of the Wigner law* (3.16). *The error bars represent the shot noise. Each data point was acquired during 100 laser pulses. The background is mainly due to photodetachment of Te$^-$($5p^5\,{}^2P_{1/2}$)* (5.2).

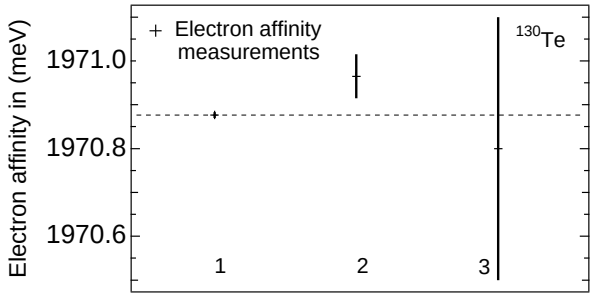

Figure 5.4.: *Tellurium electron affinity: Graphical comparison of the different experimental tellurium electron affinity values with their respective uncertainties. From left to right the values are as follows: 1, this work; 2, Thøgersen [32]; 3, Slater [107]. See also table 5.2.*

Te$^-$(^{2}P$_{1/2}$) is not critical for the accuracy achievable with our apparatus. An important part of this experiment was the use of the computer program that can vary both the wavelength step and the acquisition times for each wavelength. This has proven to be most valuable to improve the statistics and simultaneously decrease the total acquisition time, hence diminishing the probability of long term drifts. This new value of the electron affinity of tellurium is 45 times more accurate than the value of Slater [107] and fall within their error bars. The more recent value of Thøgersen [32] agrees with ours within two error bars.

5.2. Lithium electron affinity

Before the advent of photodetachment with state selective ionisation, it was very difficult to determine electron affinities of negative ions with p-wave photodetachment thresholds. As a consequence the electron affinity of lithium was not very well determined.

Electron affinity measurements using neutral particle detection could in general only hope to reach a high precision if the photodetachment threshold is of s-wave character. The state selective detection now allows to choose a higher lying atomic state that gives rise to an s-wave continuum. The electron affinity is then obtained by subtracting the atomic excitation energy from the measured threshold energy. We demonstrated the feasibility of such experiments with an improved electron affinity of lithium. This section provides the general outline of how the scheme is implemented in practice.

The idea to combine laser photodetachment and resonance ionisation [108] was born out of the struggle to reduce the background in measurements on doubly excited states of lithium, extending the results presented in section 6.1 to higher thresholds. Such measurements, exploiting the advantages of state selective detection, have now been carried out in our group by Ljungblad [109]. Even though the method has grown beyond its adolescence the background suppression is still one of its main features.

Resonance ionisation of the residual atoms, left by the photodetachment, renders final state selective detection possible while retaining the high sensitivity and superior precision and accuracy of the collinear geometry. Through the state selective ionisation it is possible to exclusively monitor photodetachment events leading to the formation of the residual atom in a specific excited state.

With this method it is possible to isolate the partial cross sections associated with a specific final state of the residual atom. A partial photodetachment cross section is labelled by the state of the residual atom, the orbital angular momentum of the outgoing electron and the coupling between the angular momenta of the atom and the electron. Since we detect the state of the residual atom A^*, it is often convenient to speak of *all* partial cross sections associated with a specific atomic state as 'A^* partial cross sections'(plural!), where A^* is the atom in an excited state. This detection scheme enriches the experimental possibilities in two important cases: firstly electron affinities of virtually any element can be determined using the advantageous s-wave thresholds, since it is almost always possible to find an accessible s-wave threshold higher up in the continuum. Secondly resonance structure due to autodetaching states can be studied in different partial cross sections.

One of the earlier measurements of the lithium electron affinity by Feldman [110] used infra-red output of a laser pumped optical parametric oscillator to investigate the p-wave threshold. Another paper [88] treats the sharp cusp at the Li(2p) threshold (figure 3.2) and attains also, as a side result, a value for the electron affinity of lithium.

Here we use a novel excitation scheme depicted in figure 5.5. This two-colour state selective photodetachment scheme is simple in concept. One laser of frequency ω_1 is used to photodetach Li^- ions producing an excited lithium atom and a free electron. A second laser of frequency ω_2 resonantly excites lithium atoms left in the 2p state to a Rydberg state, which subsequently is field ionised. Hence, the entire process can be represented by the following steps:

$$\mathrm{Li}^-(2\mathrm{s}^2\,{}^1\mathrm{S}_0) + \hbar\omega_1 \mapsto \mathrm{Li}(2\mathrm{p}\,{}^2\mathrm{P}_{1/2,3/2}) + \mathrm{e}^- \quad , \tag{5.4}$$

$$\mathrm{Li}(2\mathrm{p}\,{}^2\mathrm{P}_{1/2,3/2}) + \hbar\omega_2 \mapsto \mathrm{Li}(n\mathrm{s},n\mathrm{d}) \quad , \tag{5.5}$$

$$\mathrm{Li}(n\mathrm{s},n\mathrm{d}) \rightsquigarrow \mathrm{Li}^+(1\mathrm{s}^2\,{}^1\mathrm{S}_0) + \mathrm{e}^- \quad , \tag{5.6}$$

where $\rightsquigarrow$ denotes field ionisation and Li(ns,nd) corresponds to a highly excited Rydberg atom state with $n \approx 23$. State selectivity is accomplished in the resonant ionisation step since only Li(2p) atoms can be ionised via the intermediate Rydberg state. In this manner we were able to isolate a particluar photodetachment channel,

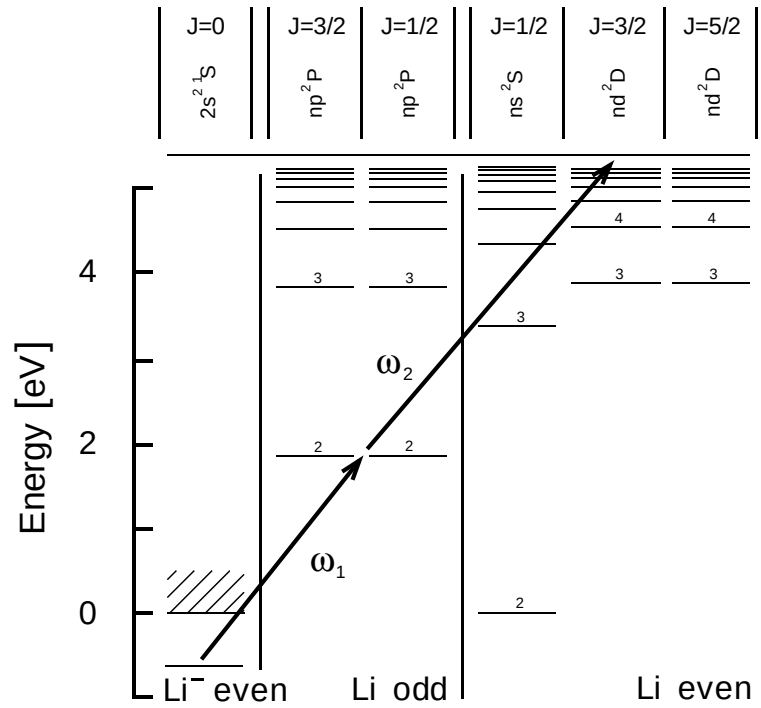

Figure 5.5.: *Li^- excitation scheme* I*: Selected bound states of Li/Li^- grouped according to their parity and total angular momentum. The arrows indicate transitions induced in this experiment.*

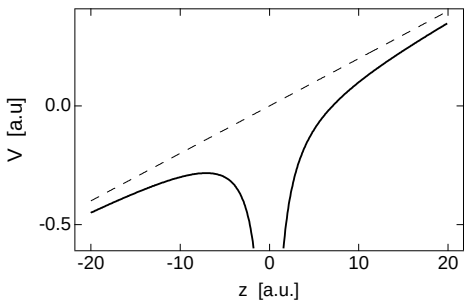

Figure 5.6.: *Static electric field ionisation: Potential energy of a hydrogen atom in an uniform electric field with a field strength of 0.02 along the z-axis. All states of the atom are unbound and can tunnel through the barrier into the continuum.*

in this case the Li(2p) channel, and investigate the partial photodetachment cross section by measurement the yield of Li^+ ions.

Field ionisation of slow atoms in a static electric field, depicted in figure 5.6, is due to tunneling predominantely along the field axis. For hydrogen this problem can be solved exactly [111] and for all other atomic systems semi-classical formulae have been derived [112–115]. For us the most improtant result is the critical field strength $\mathcal{E}_{\mathrm{cr}}$ as a function of the principal quantum number n (in a.u.),

$$\mathcal{E}_{\mathrm{cr}} = \frac{1}{16n^4} \quad , \tag{5.7}$$

above which essentially all atoms are field ionised. For the field strength of 150 $\frac{\mathrm{KV}}{\mathrm{m}}$ at the entrance of the second quadrupole QD2 the corresponding n is 22.

To find an appropriate wavelength for the ionisation laser ω_2 we tuned ω_1 above

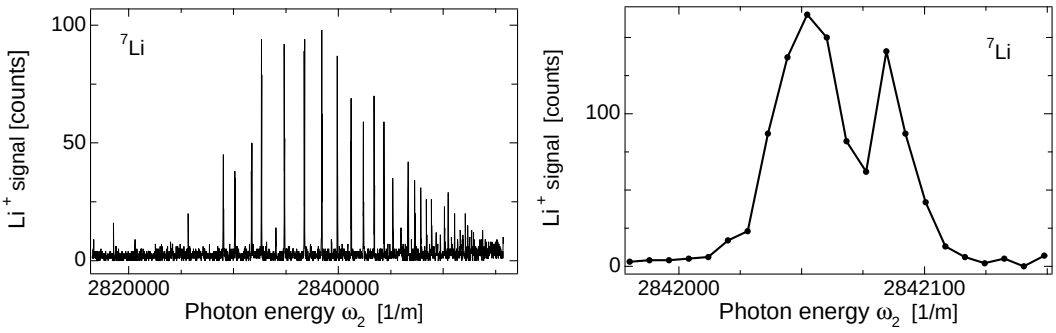

(a) Lithium Rydberg series (b) Lithium fine structure

Figure 5.7.: *Lithium Rydberg series and fine structure: In part (a) a survey of the Rydberg states below the ionisation limit of the Li atom. Note how the series are terminated at about 2 827 000 m^{-1}. The lines below that limit we interpret as being due to photo-ionisation. In part (b) the spectrum of the fine structure of the $2p\,^2P$ term is a magnification of the spectrum depicted in the figure in part (a). The left peak is due to the transition from the $J = 3/2$ level and the right one is due to the transition from the $J = 1/2$ level. For the threshold measurements, ω_2 was tuned to the peak of the $J = 1/2$ component. The energy scale is Doppler-shifted by 3100 m^{-1} to the red.*

the threshold and then tuned ω_2 from the ionisation limit down. In figure 5.7 the result of such a scan is shown. Below a certain principal quantum number n the field ionisation ceases to be effective. In part (b) of the figure a magnification of the subsequently used Rydberg transition is displayed. The doublet structure stems from the fine structure of the Li(2p) state with a splitting of 33.7 m^{-1} [116]. We found from our data a value of 33(4) m^{-1} in agreement with the known value. This, in addition, demonstrates the resolution of our machine to only be limited by the laser bandwidth of 20 m^{-1}.

Light of frequency ω_1 was generated by a dye laser operated with Coumarin 307 and light of frequency ω_2 was produced by a dye laser operated with BMQ. Both dye lasers were pumped by a common XeCl excimer laser (figure 4.9(a)). The maximum energy in a laser pulse delivered into the interaction region was 1.5 mJ for the radiation of frequency ω_1 and 200 μJ for the radiation of frequency ω_2. During the experiment both lasers were attenuated, as will be discussed below.

A typical measurement of the Li(2p) photodetachment threshold with counter-propagating laser and ion beams is shown in figure 5.8. The laser frequency ω_2 was held constant and the intensity was set to saturate the transition to the Rydberg state. The frequency ω_1 was then scanned over the Li(2p) threshold.

It was established that two processes contribute to the background, namely (a),

$$\mathrm{Li}^-(2\mathrm{s}^2\,{}^1\mathrm{S}) + \hbar\omega_2 \mapsto \mathrm{Li}(2\mathrm{p}\,{}^2\mathrm{P}) + \mathrm{e}^- \tag{5.8}$$

followed by resonance ionisation according to (5.5), (5.6) and (b) two-electron collisional ionisation. Process (a) produced nearly 80% of the background, even though

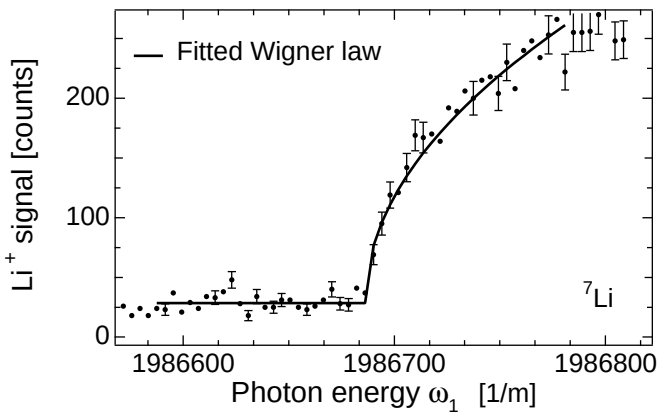

Figure 5.8.: *Li(2p)+ϵs threshold: Measurement of the partial relative photodetachment cross section of Li$^-$ around the Li(2p) threshold. The use of counter-propagating laser (ω_1) and ion beams leads to a Doppler shift of 2 169 m^{-1} to the red. The solid line is a fit of the Wigner law (3.16) to the data in the range of the line. The error bars on selected data points represent the shot noise. Each data point is obtained from 100 laser pulses.*

the intensity of laser ω_2 was attenuated. Process (b), two-electron ionisation, contributed the remaining background at the operating pressure of 5×10^{-7} Pa. This contribution was found to be proportional to the pressure and is thus dominated by double detachment, as has been discussed previously by Bae [117]. The laser intensities were too low for other processes, such as direct two-electron multi-photon detachment, to influence the experiment.

To find the photodetachment threshold energy we fitted (3.16) to our data and obtained the threshold energy E_0 according to (4.1). With aid of O'Malley's correction (3.17) we estimated the range of validity of the Wigner law (3.16). For an electric dipole polarisability of α_{D}=152 a.u. for the Li(2p ^{2}P) state [118] we found the second term in (3.17) to be much less than unity up to 100 m^{-1} above the threshold, and consequently the Wigner law should be applicable over this range. This, of course, assumes that there are no resonances in this region, a condition that has previously been established by Dellwo [119].

Our value for the threshold energy E_0 is

$$E_0 = 1\,988\,855(16)\ \mathrm{m}^{-1} \quad . \tag{5.9}$$

From this the lithium electron affinity is determined by subtracting the well known 2p $^2\mathrm{P}_{1/2} \mapsto$ 2s ^{2}S transition of 1 490 364.8130(14) m^{-1} [120]. We find a lithium electron affinity of 498 490(17) m^{-1}. In figure 5.9 this value is compared to previous measurements and in table 5.3 we also compiled a number of theoretical results.

We have demonstrated that photodetachment spectroscopy combined with resonance ionisation is a powerful method for studying partial photodetachment cross sections of negative ions. The collinear beam geometry simultaneously provides high sensitivity, due to the large interaction volume, and excellent resolution, due to velocity compression. In addition, removal of the Doppler shift to all orders can be achieved by use of two separate measurements involving co- and counter-propagating laser and ion beams. Both merits can be fully retained for channel-specific photodetachment investigations with the excitation scheme used in this experiment. Our

Table 5.3.: *Lithium electron affinity: Comparison of the different measurements and calculations. The value in m^{-1} is only given if the publication contains the value.*

Author	Affinity in m^{-1}	Affinity in meV
Experiment		
Feldman (1976) [110]		618.2(5)
Bae (1985) [88]		617.3(7)
Dellwo (1992) [119]	$4.980\,9(16)\times10^5$	617.6(2)
This work [23]	$4.984\,90(17)\times10^5$	618.049(20)
Theory (after 1992)		
Chung (1992) [121]		617.4(2)
Froese Fischer (1993) [122]		617.64

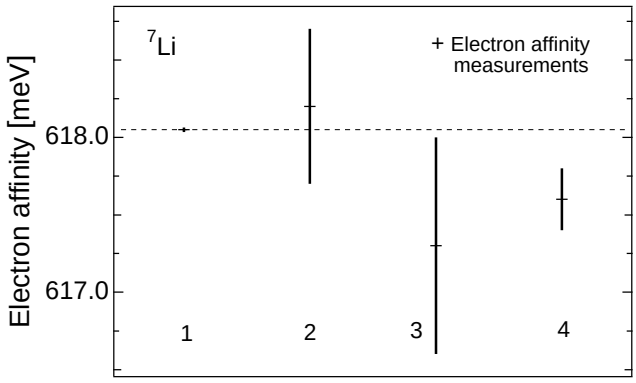

Figure 5.9.: *Lithium electron affinity: Graphical comparison of the different experimental lithium electron affinity values with their respective uncertainties. From left to right the values are: 1 this work, 2 Feldmann [110], 3 Bae [88], and 4 Dellwo [119]. See also table 5.3.*

improved Li electron affinity reveals the potential of this method, which, in principle, can be extended to essentially all elements.

6. Autodetachment resonances

The study of resonance structure in the photodetachment cross section of lithium is the first in a series of experiments [109, 123–125] aiming to deepen our knowledge of doubly excited states in negative ions. In this experiment we used neutral particle detection to unveil resonance structure near the Li(3p) threshold. The experimental work was inspired and accompanied by calculations of Pan [126] and Lindroth [124, 127].

Doubly excited states allow us to investigate the correlated motion of a pair of electrons and therefore extend our knowledge of the limits of the independent particle approximation. The two prototype two-electron systems, H^- and He, have been studied for the last 30 years and a great deal of insight in the nature of two-electron correlation has been gained. With the work performed on autodetaching doubly excited states of Li^- and He^- we studied systems where two highly excited electrons interact with a rather simple singly charged core. Comparison of H^- and He with Li^- and He^- reveals similarities as well as differences related to the finite core of Li^- and He^-. These simple negative ions are fairly tractable to theory, and therefore supply valuable insight in the strive of understanding the more general many-body problem.

6.1. Li^- doubly excited states

Here we report on the first observation of resonance structure in the total cross section for the photodetachment of Li^-. The resonances are of $^1P^o$ final state symmetry and are optically coupled to the ground state. They arise from the photo excitation and subsequent autodetaching decay of doubly-excited states of Li^- that are embedded in continua representing an excited Li atom and a free electron. The resonances were observed to lie in the energy region between the Li(3s) and Li(3p) thresholds. Recently Pan, Starace and Greene used an eigenchannel R-matrix method to predict the shape of the photodetachment cross section in the vicinity of the Li(n=3) threshold [126] and the Li(n=4,5,6) thresholds [128]. The measurements reported here present us with an opportunity to compare experimental data on Li^- with corresponding data on H^- [129]. Differences in the spectra of Li^- and H^- associated with the lifting of the degeneracy characteristic of the hydrogen atom are apparent as are certain similarities [127]. I also present calculations on Li^- and H^- by Lindroth [124] which are used to explain the origin of the observed resonances. The method accounts for full correlation between the outer electrons. The autodetaching

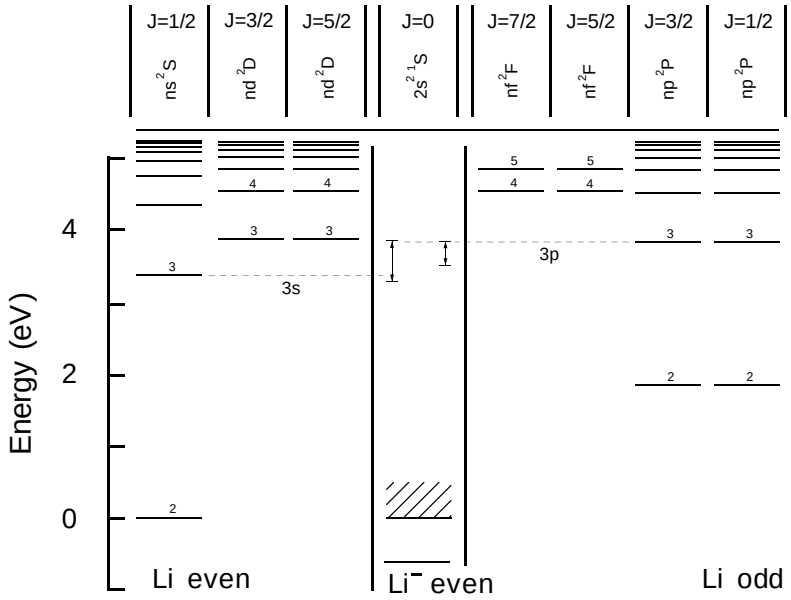

Figure 6.1.: *Li^- excitation scheme* II: *Selected bound states of Li/Li^- grouped according to their parity and total angular momentum. The left arrow indicates the range of the theoretical curve in figure 6.2 and the right one the range of our data in figure 6.2.*

decay of doubly excited states is treated using complex rotation.

The Li^- ions were generated in the plasma ion source, but, in contrast to the normal procedure, the negative ions were *directly* extracted from the discharge because the charge exchange cell was not yet operative. This is less efficient than the usual method of charge exchange of positive ions and consequently gave a current not exceeding 1 nA in the interaction region.

The light required for the photodetachment was generated by frequency doubling the output of our dye laser operated with Rhodamine 6G and Coumarin 153. A normalisation to the laser power was performed where ever necessary.

In figure 6.1 the tuning range of the experiment is indicated. The excitation process can be summarised as

$$\mathrm{Li}^-(1\mathrm{s}^2 2\mathrm{s}^2\,{}^1\mathrm{S}) + \hbar\omega \mapsto \mathrm{Li} + \mathrm{e}^- \quad . \tag{6.1}$$

The experimentally determined total photodetachment cross section is shown as the dots in figure 6.2. All data points have been normalised to the theoretically calculated value at the Li(3p) threshold. Also the energy scale has been shifted so that the Li(3p) threshold of the data and the calculation coincide. The scatter in the data is primarily caused by the small but unavoidable change in the overlap of the ion and laser beams as the wavelength of the laser was scanned. The normalisation procedure applied in this experiment was unable to completely account for beam overlap variations. We estimated, however, that this effect causes a maximum error in the relative cross section over the whole spectrum of less than 10%. The statistical scatter, mainly caused by the shot noise in counting of the neutral particles, is less than 3%.

The experimental data exhibit three significant features. First there is the Wigner cusp, 3p figure 6.2, at the Li(3p) threshold, second there is a narrow reso-

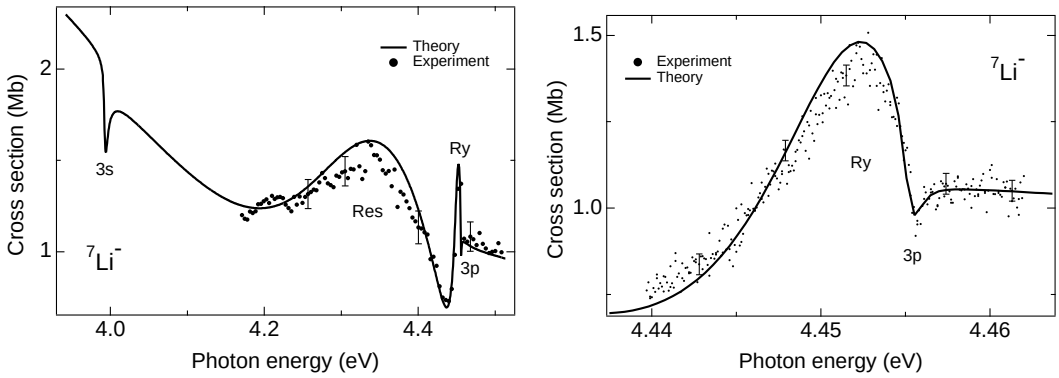

(a) Measured and calculated photodetachment cross section near the Li(3p) threshold

(b) Magnification near the Li(3p) cusp

Figure 6.2.: *Lithium total photodetachment cross section near the Li(3p) threshold: The solid line is a calculated absolute photodetachment cross section and the dots are the measured relative photodetachment cross section, which is scaled, but not fitted, to match the calculated value at the Li(3p) threshold. The labels 3s and 3p mark the Li(3s) and Li(3p) thresholds, and Res,Ry mark a broad resonance and a Rydberg like resonance (see tabular 6.1). The error bars represent one estimated standard deviation. Note how the data follow the sharp Wigner cusp.*

nance structure Ry and finally a very broad resonance Res occupies a large part of the region between the Li(3s) and Li(3p) thresholds.

The calculated cross section is shown as a solid line and is in close agreement with another recent calculation [126, 127]. The presented calculation predicts a resonant state of 0.36 eV width to lie 4.32 eV above the ground state of Li^- as shown in table 6.1. This state appears to be analogous to the symmetrically excited intra-shell $({}_3\{0\}_3^+)\,{}^1P^o$ [62] state in H^-. It has a similar binding energy relative to the double detachment limit, but is about one order of magnitude broader. The broadening of the resonance in Li^- arises from the strong coupling to the 3sεp continuum, which is not available below H(n=3) in H^-. The resonant state in Li^- is dominated by the configurations 3p3d and 4s3p and there appears to be no significant contribution to the localised part of the wave function from configurations with one electron in the 3s orbital, which is also in contrast to the case of H^-.

While the H^- intra-shell resonance is well described by a Fano profile the width of the resonant state in Li^- is too broad for this to be possible. The calculated width of 0.36 eV is overlapping the 3p threshold as well as the narrow resonance seen just below it in figure 6.2. The latter resonance is due to asymmetrically excited Rydberg-like states. In these states one of the electrons in the doubly excited pair occupies a more loosely bound orbital than the other. The presence of the threshold and the interference between the resonances affects the shape of the cross section curve significantly. The assumption necessary to obtain a Fano profile, that only one state determines the shape, is thus not valid. The interference results in a narrowed structure in the spectrum, especially on the high energy side, compared to

Table 6.1.: *Li^- doubly excited states: Comparison of theoretical results for intra-shell $^1P^o$ states of H^- below the H(n=3) threshold and of Li^- below the Li(3p) threshold. The binding energy E_{bind} is relative to the double detachment limit and E_{trans} is the transition energy from the ground state. Calculated resonance parameters for the two Rydberg-like resonances, marked Ry in figure 6.2(b), below the Li(3p) threshold are given. Note the strong overlap of these two resonances.*

Element	Label	E_{bind} (eV)	Γ (eV)	E_{trans} (eV)
H^-		-1.706	0.033	12.647
Li^-	Res	-1.688	0.36	4.322
Li^-	Ry	-1.556	0.020	4.453
Li^-	Ry	-1.555	0.016	4.454

that which would arise from a hypothetically isolated doubly excited state of width 0.36 eV. Rydberg-like resonant states are also apparent in the calculated spectrum of H^-. These states are bound relative to the H(n=3) limit by the strong dipolar field between the two electrons. The strength of this field is due to the degeneracy of the H(3ℓ) states which results in nearly equal admixture of 3snp and 3pns (or 3pns and 3dnp) configurations in the composition of the Rydberg states.

The Rydberg-like states Ry in Li^-, however, do not have this character. They are completely dominated by 3pnℓ configurations, with $n \gg 3$, and the dipolar field is in this case insignificant. The explanation for the existence of the Rydberg states in Li^- is the inability of the monopole part of the electron-electron interaction to screen the singly-charged core completely. The residual nuclear attraction binds the states below the Li(3p) threshold.

We have studied the total photodetachment cross section of the Li^- ion in the energy region between the Li(3s) and Li(3p) thresholds. This region is dominated by a broad resonance. A narrower resonance structure lies just below the Li(3p) threshold. By comparing the data with calculated photodetachment cross sections for Li^- and H^- we have been able to identify the broad resonance in the Li^- spectrum as being associated with the presence of a symmetrically excited intra-shell doubly excited state, analogous to, but much broader than, the intra-shell state in H^-. The sharper resonance structure is identified with asymmetrically excited Rydberg like states.

6.2. He^- doubly excited states

Another, and perhaps even more exciting, aspect of the state selective detection method is the possibility to seperately monitor partial cross sections. This is especially useful to investigate high lying resonances. The modulation of the total photodetachment cross section due to autodetaching states can become very small [126,130], but in certain partial cross sections there may still occur quite pro-

nounced modulation. Therefore this state selective detection scheme has rapidly become an indispensible tool for studies of negative ions.

The expriments on He doubly excited states, in particular, profited from both the backgound suppression and enhanced modulation of partial cross sections. The background suppression proved to be truly vital since the decay of the He^- ground state already leads to a background of neutral helium, thus rendering any investigation with neutral particle detection impossible. Earlier ill fated attempts to measure resonance structure near the He(n=3) thresholds in this laboratory suffered from saturation of the detection system caused by excessive neutral particle background. As is further elaborated in this section, we fard much better with the state selective detection now at our disposal.

The metastable He^- ion has received considerable attention since its discovery by Hiby in 1939 [131]. This simple three electron ion is the prototype of an unusual class of negative ions that are not stable, but rather metastable, against autodetachment. The lowest lying state is the 1s2s2p $^4P^o$ state, which is bound by 77.524(5) meV relative to the 1s2s ^3S state of He [132] in agreement with the calculated value of 77.51(4) by Bunge [133]. The He^- ion in this spin aligned quartet state cannot radiate and, since it is embedded in a doublet continuum, it can only autodetach via the relatively weak magnetic interactions (table 2.1). The varying strengths of these spin dependent interactions result in a differential metastability among the three fine structure levels. The longest lived J=5/2 level which can only decay via the spin-spin interaction (table 2.1) has, for example, a lifetime of 350(15) μs [25]. Metastable He^- ions are therefore sufficiently long lived to pass through a typical apparatus with only minor depletion by autodetachment.

Excited states of He^-, on the other hand, decay rapidly via Coulomb autodetachment. Their presence is manifested as resonance structure in scattering cross section close to thresholds for new channel openings, i. e. the excited state energies of the He atom. Many doublet resonances have been observed, for example, as transient intermediate states in studies of electron impact on atomic He targets [13]. Excited quartet states of He^-, however, have hitherto received far less attention. Such states appear as resonances in the photodetachment cross section and, to a lesser extent, in cross section for detachment via heavy particle collisions. Selection rules on photoexcitation from the 1s2s2p $^4P^o$ ground state of He^- allow transitions only to ^4S, ^4P and ^4D excited states. There have been several experimental [134–136] and theoretical studies [137–139] of the photodetachment cross section of He^-. Most recently, Xi and Froese Fischer [140] have calculated the position and width of quartet states of He^- up to the He($n = 4$) thresholds.

To investigate the He^- photodetachment cross section we use the previously introduced (section 5.2) two-colour state selective excitation scheme. The specific steps for the excitations are depicted in figure 6.4. For all resonances the yield of He^+ ions in the state selective excitation was recorded as a function of ω_1, while the frequency ω_2 was held constant on the transition to the Rydberg state. During a scan we assume the laser power of ω_2 to be constant. If the resonance is narrow also ω_1 is assumed to stay constant, otherwise we account for the varying light intensity

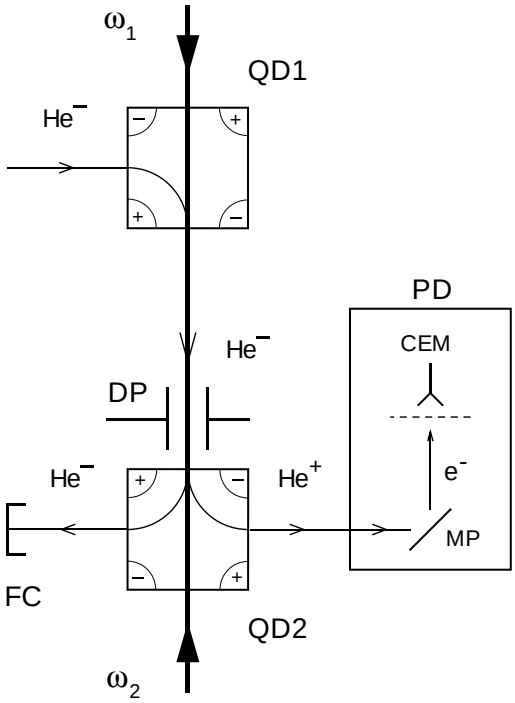

Figure 6.3.: *Modified interaction-detection chamber: QD1,QD2, electrostatic quadrupole deflectors; CEM, channel electron multiplier; DP, deflection plates; PD, positive ion detector; FC, Faraday cup; MP, metal plate. The deflection plates DP serve to sweep collisionally created positive ions out of the beam, thereby improving the signal to noise ratio. They are periodically grounded to monitor the negative ion current. Ion- and laser beams were merged in the 0.5 m long interaction region between the quadrupole deflectors.*

by a normalisation to the measured laser power.

The detection scheme based on the selective detection of residual atoms was effective in eliminating a potential background source unique to measurements involving metastable negative ions. Since He^- ions are non-stable, the ion beam will contain a fraction of He atoms produced, in flight, by autodetachment. These helium atoms will, however, be in the He($1s^2\,{}^1S$) ground state and will therefore not be resonantly photo-ionised.

The state selectivity allows us to concentrate our measurement efforts on the partial cross sections that actually contain resonance structure. The autodetachment selection rules, given in table 2.1 on page 26, impose restrictions on which partial cross sections can be expected to contain resonance structure.

The ${}^4He^-$ beam was produced from a mass selected He^+ ion beam via charge exchange in a cesium vapour cell. The beam energy was 3.1 keV. A current of typically 1 nA was obtained in the interaction region.

The apparatus was designed to reduce the background of He^+ ions produced by double collisional detachment by installing a pair of deflection plates (DP figure 6.3) just before the second quadrupole deflector (QD2). The transverse electric field between the deflection plates was insufficient to field ionise the Rydberg atoms, but strong enough to sweep collisionally created He^+ ions out of the beam.

The 1s3s4s ${}^4S$ state

To study the 1s3s4s ${}^4S$ resonance we used an excitation scheme, depicted in figure 6.4, that can be summarised by the following equations for state selective detection

Table 6.2.: *He$^-$(1s3s4s ^{4}S) calibration lines [104]: The argon levels are designated in Paschen notation. For counter-propagating laser (ω_1) and ion beams we used the lines a, b and c and for co-propagating laser (ω_1) and ion beam we used the lines b, c and d for calibration.*

#	Transition	Line (m^{-1})
a	$3p_5 \rightarrow 1s_4$	2 381 235.9(2)
b	$3p_4 \rightarrow 1s_3$	2 385 376.7(2)
c	$3p_8 \rightarrow 1s_5$	2 385 556.5(2)
d	$3p_2 \rightarrow 1s_3$	2 390 593.3(2)

on He(1s2s ^{3}S),

$$\mathrm{He}^-(1s2s2p\,^4P^o) + \hbar\omega_1 \mapsto \mathrm{He}(1s2s\,^3S) + e^-(\epsilon s) \quad , \tag{6.2}$$

$$\mathrm{He}(1s2s\,^3S) + \hbar\omega_2 \mapsto \mathrm{He}(1s24p\,^3P^o) \quad , \tag{6.3}$$

$$\mathrm{He}(1s24p\,^3P^o) \rightsquigarrow \mathrm{He}^+(1s\,^2S) + e^- \quad , \tag{6.4}$$

and for state selective detection of He(1s2p ^{3}P^o),

$$\mathrm{He}^-(1s2s2p\,^4P^o) + \hbar\omega_1 \mapsto \mathrm{He}(1s2p\,^3P^o) + e^-(\epsilon p) \quad , \tag{6.5}$$

$$\mathrm{He}(1s2p\,^3P^o) + \hbar\omega_2 \mapsto \mathrm{He}(1s25d\,^3D) \quad , \tag{6.6}$$

$$\mathrm{He}(1s25d\,^3P) \rightsquigarrow \mathrm{He}^+(1s\,^2S) + e^- \quad , \tag{6.7}$$

where $\rightsquigarrow$ in both cases represents field ionisation.

The calibration of the energy scale is done as described in section 4.2 using the four transitions in argon given in table 6.2.

A typical measurement of the 1s3s4s ^{4}S resonance in the He(1s2s ^{3}S) partial cross sections and the He(1s2p ^{3}P^o) partial cross sections is shown in figure 6.5. For the He(1s2s ^{3}S) cross sections we found three processes to significantly contribute to the background: firstly (a), collisional detachment leaving the He atom in the 1s2s ^{3}S state, and secondly (b), photodetachment by the laser ω_2

$$\mathrm{He}^-(1s2s2p\,^4P^o) + \hbar\omega_2 \mapsto \mathrm{He}(1s2s\,^3S) + e^-(\epsilon s, \epsilon d) \quad , \tag{6.8}$$

followed by resonance ionisation indicated (6.3) and (6.4). Thirdly (c), non-resonant photodetachment by the laser of frequency ω_1,

$$\mathrm{He}^-(1s2s2p\,^4P^o) + \hbar\omega_1 \mapsto \mathrm{He}(1s2s\,^3S) + e^-(\epsilon d) \quad , \tag{6.9}$$

and then proceeding as in (6.3) and (6.4).

To reduce the collisional detached contribution (a) we maintained a pressure of 5×10^{-7} Pa in the interaction chamber. To reduce contribution (b) we attenuated the output of laser ω_2.

The selection rule ΔL=0 for Coulomb autodetachment (table 2.1 page 26) in LS-coupling forbids the 1s3s4s ^{4}S resonance from appearing in the He(1s2s ^{3}S)+e$^-$(ϵd)

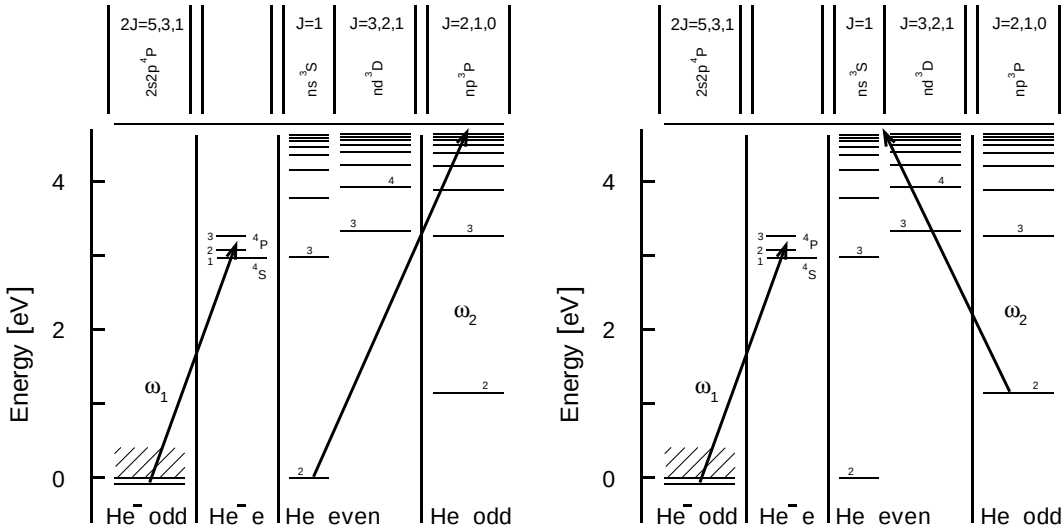

(a) Monitoring on 1s2s ^{3}S (b) Monitoring on 1s2p ^{3}P^o

Figure 6.4.: *He⁻ excitation scheme: Selected states of He/He⁻ grouped according to their parity and total angular momentum. The solid arrows represent the transitions induced in the measurements, see also* (6.2) *to* (6.7) *and figure 6.5. The designation of the He⁻ levels is, 1, 1s3s4s* ^{4}*S; 2, 1s3p*^{2} ^{4}*P; 3, 1s3p4p* ^{4}*P; according to [140].*

partial cross section. Thus, the process (c), as represented by (6.9), contributes a constant background over the region shown in the upper part of figure 6.5(a). Xi and Froese Fischer [130] predict a d-wave photodetachment cross section of 6 Mb across the resonance, figure C.3(c) page 87, and a peak s-wave cross section of approximately 20 Mb, upper part of figure 6.5(b).

For the He(1s2p ^{3}P^o) cross sections we found two processes to significantly contribute to this background: firstly (a), collisional detachment leaving the He atom in the 1s2p ^{3}P^o state, and secondly (b), photodetachment by the laser ω_2

$$\mathrm{He}^-(1\mathrm{s}2\mathrm{s}2\mathrm{p}\,^4\mathrm{P}^o) + \hbar\omega_2 \mapsto \mathrm{He}(1\mathrm{s}2\mathrm{p}\,^3\mathrm{P}^o) + \mathrm{e}^-(\epsilon\mathrm{p}), \tag{6.10}$$

followed by resonance ionisation indicated (6.6) and (6.7).

To reduce the collisional detached contribution (a) we maintained a pressure of 5×10^{-7} Pa in the interaction chamber and to reduce contribution (b) we attenuated the output of laser ω_2.

The Doppler free resonance energy E_0^{4s}, obtained as outlined in (4.1) on page 48, is

$$E_0^{4s} = (2\,386\,803.1 \pm 4.2)\ \mathrm{m}^{-1} \quad , \tag{6.11}$$

and the resonance width Γ^{4s} is,

$$\Gamma^{4s} = 160(16)\ \mathrm{m}^{-1} \tag{6.12}$$

Table 6.3.: *He^- (1s3s4s ^4S) state: Comparison of the experimental resonance energy and width with the theoretical prediction of Xi [140]. The energy position agrees, within the limited accuracy of the calculation, with the experimental value.*

	1s3s4s ^{4}S	
	E_0 (eV)	Γ (meV)
Experiment:		
This work	2.959 260(6)	0.20(2)
Theory:		
Xi [140] (1996)	2.959 07	0.19

This result is an average obtained from 11 spectra taken with co-propagating laser and ion beams and 14 spectra taken with counter-propagating beams. There are two major contributions to the quoted uncertainty: 1 m^{-1} is due to the calibration uncertainty, and the remainder is due to statistical scatter of the fitted resonance parameters. In table 6.3 and in figure 6.7,6.8 the values are compared with recently calculated resonance parameters.

The measured resonance parameters agree with those calculated by Xi and Froese Fischer [140] within the limited precision of the latter. Our measurement is, however, almost two orders of magnitudes more precise and should stimulate further theoretical work.

The 1s3p^2 ^{4}P and 1s3p4p ^{4}P state

To study the 1s3p^2 ^{4}P and 1s3p4p ^{4}P resonances we used an excitation scheme, depicted in figure 6.4(b), that can be summarised by (6.5), (6.6) and (6.7). In this case a calibration for the 1s3p^2 ^{4}P was achieved with the known energy of the 1s3s4s ^{4}S resonance, lying close to the investigated structure, and as relative scale we used the wavelength read from the laser. Seperate scans over the 1s3s4s ^{4}S resonance had to be taken since the step length in the scans of the 1s3p^2 ^{4}P resonance was too long to even find the 1s3s4s ^{4}S resonance. Owing to the broadness of the 1s3p^2 ^{4}P resonance a more precise calibration was not neccessary. For the 1s3p4p ^{4}P we calibrated with several argon lines (table 6.5) surrounding the resonance. We did not take Fabry Perot fringes but as a relative wavelength scale we used the internal scale of the laser. Since we took four calibration lines, we could check the wavelength dependency of the laser wavelength scale offset. Over the range of the measurement the offset was linearly dependent on the wavelength.

A typical measurement of both resonances in the He(1s2p ^{3}P^o) partial cross sections is shown in figure 6.6(a). Three processes contribute to the background of both measurements: firstly (a) collisional detachment leaving the helium atom in the 1s2p ^{3}P^o state, and, secondly (b) photodetachment by ω_2 summarised in (6.10). Thirdly (c) photodetachment creating a He(1s3s ^{3}S) atom, which decays with a life-

Table 6.4.: *$He^-(n = 3\,^4P)$ states: Comparison of experimental resonance energies and widths with theoretically predicted ones. The energy positions agree well with the calculations. The widths deviate from the predicted values.*

	$1s3p^2\,^4P$		$1s3p4p\,^4P$	
	E_0 (eV)	Γ (meV)	E_0 (eV)	Γ (meV)
Experiment:				
This work	3.072(7)	50(5)	3.264 87(5)	0.61(5)
Theory (after 1995):				
Bylicki [142] (1997)	3.074 24	37	3.264 78	2.45
Xi [140] (1996)	3.074 70	37.37	3.265 54	1.30
Themelis [143] (1995)	3.096 6	34.6	–	–

time of 36 ns [141] to the $1s2p\,^3P^o$,

$$He^-(1s2s2p\,^4P^o) + \hbar\omega_{1,2} \mapsto He(1s3s\,^3S) + e^- \quad , \tag{6.13}$$

$$He(1s3s\,^3S) \mapsto He(1s2p\,^3P^o) + \hbar\omega \quad , \tag{6.14}$$

proceeding further as in (6.6) and (6.7). The short lifetime makes this an efficient process. This background contribution is unfortunately proportional to the intensity of the laser light ω_1. Therefore we could not improve the signal to noise ratio much by attenuating ω_2. We found a resonance energy E_0^{3p} for the $1s3p^2\,^4P$ resonance of,

$$E_0^{3p} = 2.478\,2(55) \times 10^6\ \mathrm{m}^{-1} \quad , \tag{6.15}$$

and a width Γ^{3p},

$$\Gamma^{3p} = 40(3) \times 10^3\ \mathrm{m}^{-1} \quad . \tag{6.16}$$

The uncertainty of the resonance energy is due to the calibration uncertainty of 40 m^{-1} and the statistical scatter of the fitted parameters of 36 m^{-1}. For the $1s3p4p\,^4P$ resonance we found an energy of,

$$E_0^{4p} = 2\,633\,297(40)\ \mathrm{m}^{-1} \quad , \tag{6.17}$$

and a width $\Gamma^{4p}$of,

$$\Gamma^{4p} = 492(35)\ \mathrm{m}^{-1} \tag{6.18}$$

A comparison of the measured parameters with recent calculations is given in table 6.4.

Discussion

We have investigated three doubly excited states of He^- below the double detachment limit. The lowest lying resonance is of ^4S symmetry and all others of ^4P

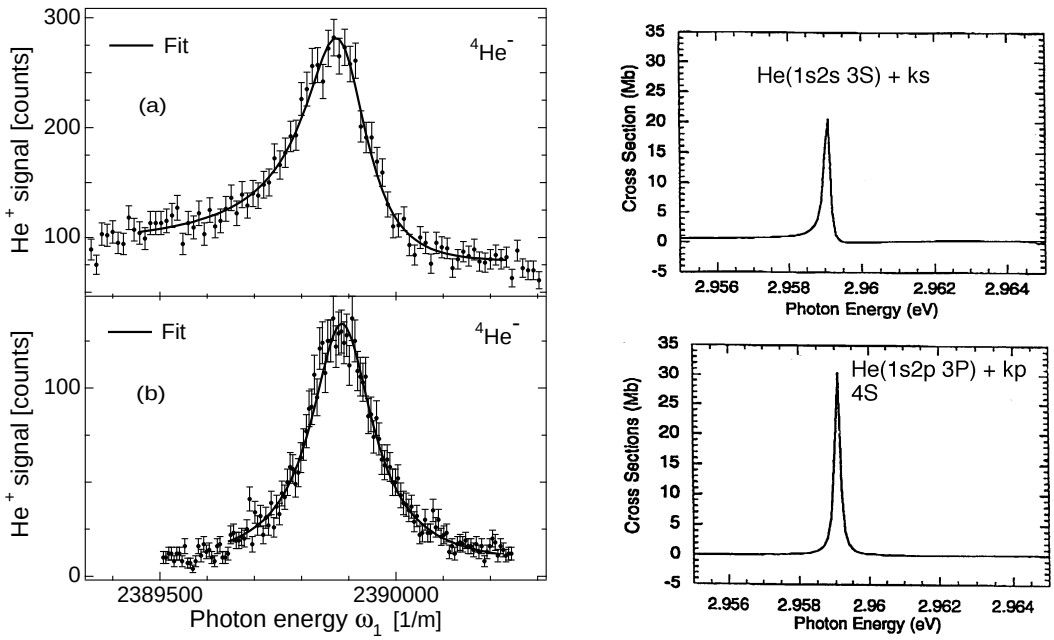

(a) Measured He(1s2s ^{3}S) and He(1s2p ^{3}P^o) partial cross sections

(b) Calculated partial cross section

Figure 6.5.: *Partial photodetachment cross section near the He$^-$(1s3s4s ^4S) state: In the upper graph of part (a) we show a measurement of the He(1s2s ^3S)+e$^-$(ϵs, ϵd) partial photodetachment cross sections of He$^-$ in the vicinity of the 1s3s4s ^4S resonance, and in the lower graph of part (a) a measurement of the He(1s2p $^3P^o$)+e$^-$(ϵp) partial photodetachment cross sections of the same state. The use of co-propagating laser (ω_1) and ion beams causes the resonance to be Doppler shifted by 3 089 m^{-1} to the blue. The solid line is a fit to the data using equation* (3.23)*. The error bars represent the shot noise. Each data point represents 200 laser pulses in the upper graph of part (a) and 100 laser pulses in the lower graph of part (a). For a comparison of width and position see figure 6.7,6.8 and table 6.3. The partial cross sections in part (b) are calculated by Xi [130].*

Table 6.5.: *He$^-$(1s3p4p ^4P) calibration lines: The tansition in Ar* I *is labled in Paschen notation and the other in the usual spectroscopic notation.*

#	Transition	Energy (m^{-1})	Element
a [104]	$4p_5 \mapsto 1s_2$	2 607 041(1)	Ar I
b [144]	[Rn]?J=9$\mapsto$[Rn]?J=8	2 643 532(1)	U I
c [145]	[Mg]3p^{4}6f J=5/2$\mapsto$[Mg]3p^4(^{3}P)4d ^{4}D$_{3/2}$	2 647 870(1)	Ar II
d [145]	[Mg]3p^4(^{3}P)5s ^{4}P$_{3/2}$$\mapsto$[Mg]3p^4(^{3}P)4p ^{4}P$^o_{1/2}$	2 651 401(1)	Ar II

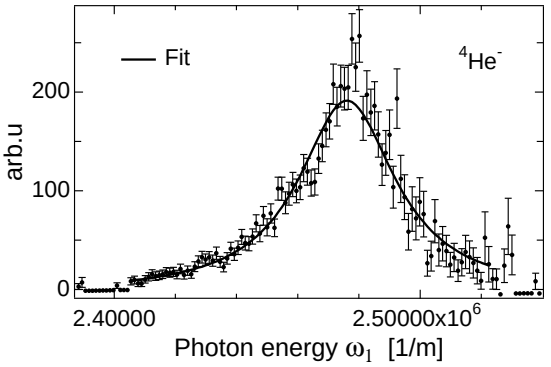

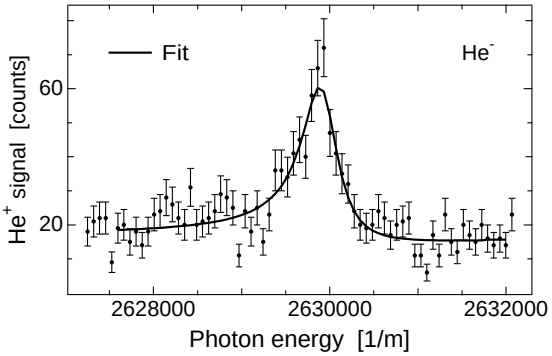

(a) The He$^-$(1s3p^2 ^{4}P) (upper graph) and He$^-$(1s3p4p ^{4}P) resonance (lower graph) both monitored on the He(1s2p ^{3}P^o) state.

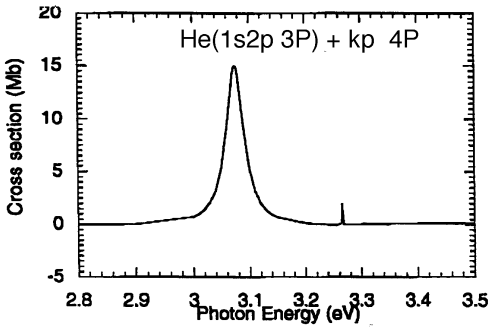

(b) Calculated He(1s2p ^{3}P^o)+ϵp absolute partial cross section for He$^-$(1s3p^2 ^{4}P) (left peak) and He$^-$(1s3p4p ^{4}P) (right peak)

Figure 6.6.: *Photodetachment cross section near the He$^-$(n=3 ^{4}P) states: In the part (a) we show a measurement of the He(1s2p ^{3}P^o)+ϵp partial photodetachment cross section in He$^-$ near the 1s3p^2 ^{4}P and 1s3p4p ^{4}P state. The solid line is a fit to the data using* (3.23)*. In the part of (a) each data point represents 100 laser pulses. The curve in the upper part of (a) is normalised to the laser power with the small background subtracted. The error bars indicate the shot noise. The calculated partial photodetachment cross section in part (b) is calculated by Xi [130]. For a comparison of width and position of the resonances see table 6.4 and figure 6.7 and 6.8.*

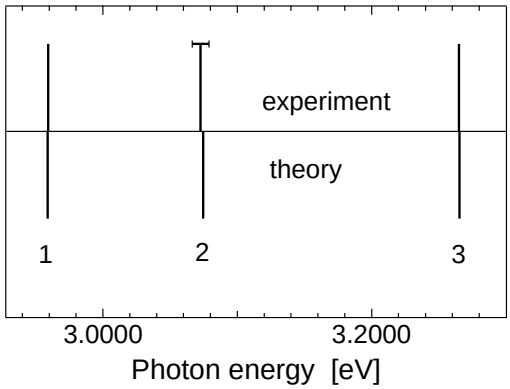

Figure 6.7.: *Energies of He$^-$ doubly excited states near the He(n=3) thresholds: A very good agreement of the predicted [140] and measured energies is found. If no error bar on the experimental value (upward) is indicated then it is less or equal to the line width. No error bars for the theoretical values are avaliable. For numerical values see table 7.4 page 78.*

symmetry, all with even parity. The resonance structure in different partial cross sections due to these autodetaching states has been studied.

In the case of the He$^-$(1s3s4s ^{4}S) state *all* possible decay channels have been measured. The shape of both partial cross sections (figure 6.5) qualitatively agrees with the predictions by Xi [130]. In addition, the width of this resonance is in perfect agreement with the predicted value. The amplitude ratio of the peak resonance cross section (figure 6.5(b) upper part) to the flat background (figure C.3(c) page 87) is predicted [130] to be 3.0(3), whereas we find this ratio to be about 3.6(3) which is not quite significantly higher.

For the 1s3p^2 ^{4}P state we also find good agreement between the predicted resonance shape (figure 6.6) and our measurement. A similar comparison is unfortunately not possible for the 1s3p4p ^{4}P resonance due to the poor resolution of the avaliable graphs. In all cases the energy position of the resonance coincides well with the experimentally determined value, shown in table 6.3,6.4 and figure 6.7 within the limited accuracy of the calculation.

The 1s3s4s ^{4}S state has also been theoretically investigated by Le Dourneuf [139]. They analysed He$^-$ doubly excited states from a hyperspherical point of view and find a good correspondence between doubly excited states of H$^-$ and He$^-$. Specifically the charge density of doubly excited states of He$^-$ very closely resembles the charge density distribution of the analog states in H$^-$. It is remarkable how little the core pertubation disturbes the correlation pattern of the two excited electrons. From the quantum numbers given by Le Dourneuf we find that the 1s3s4s ^{4}S state has $A = -1$.

The widths of doubly-excited states of Li$^-$ does not vary systematically with the value of A. The resonance of Li$^-$ cannot be classified as narrow or broad as for He$^-$. The core appears to have a more profound effect on the excited pair of electrons than in He$^-$. This seems surprising to us because the cores are rather similar with respect to their first excitation energy and dipole polarisability.

The 1s3s4s ^{4}S resonance has $A = -1$ and should accordingly be narrow. This is confirmed by our experiment and the theory by Xi. For the 1s3p^2 ^{4}P and 1s3p4p ^{4}P resonances the measured widths deviates from the predicted ones [140, 142, 143, 146,

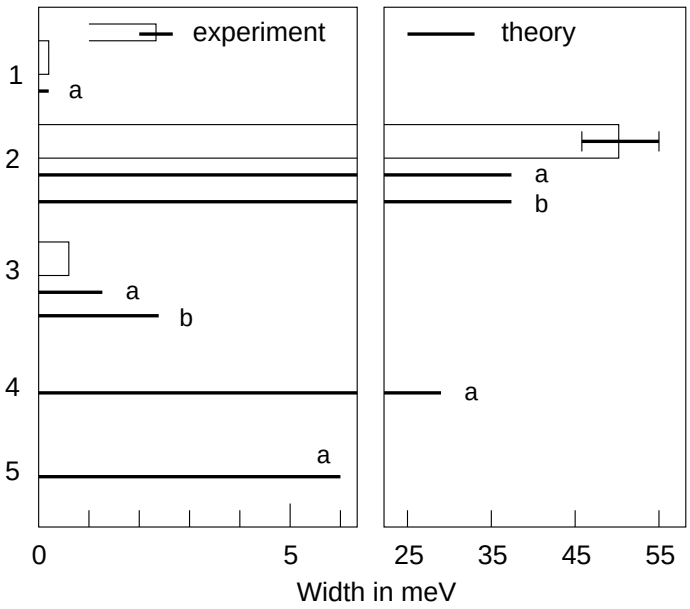

Figure 6.8.: *Widths of He^- doubly excited states near the He(n = 3) thresholds: The states with odd numbers are as narrow or narrower as predicted. These state are of A=−1 character, see section 2.2 and the states with even numbers are all broader than predicted. These states should be about 100 to 10 000 times broader than the adjacent A=−1 resonances. If no error bar is given then it is less or equal to the line width. For numerical values see tables 6.3, 6.4. The* a *marks values from Xi's calculation [140] and* b *values of Bylicki [142].*

147]. Taking the widths as guidance I suggest the $1s3p^2\,{}^4P$ state has $A = +1$ and the $1s3p4p\,{}^4P$ state has $A = -1$. It appears more difficult to calculate the widths of higher lying $A = -1$ resonances than for resonances with $A = +1$. With our experiments we hope to inspire theorists to refined calculations on He^-.

Xi [140] also predicts two states of He^- near the He($n = 4$) thresholds. Here, just as near the He($n = 3$) thesholds, the lower lying $1s4p^2\,{}^4P$ state is predicted to be much broader than the higher lying $1s4p5p\,{}^4P$ state. In the near future the study presented here will be amended with measurements of the $1s4p^2\,{}^4P$ and $1s4p5p\,{}^4P$ states.

7. Summary and conclusion

In this chapter we compile all results of this thesis, mainly in form of tables. A very brief description of the experiment, based on the abstracts of the respective publication, and an assessment of the accuracy is accompanied by a table to give the reader convenient access to the main results of this thesis. I present the experiments in the same order as they appear in the table of contents.

7.1. Summary of Results

The electron affinity of tellurium

The electron affinity of tellurium has been determined to be 1 589 618(5) m^{-1}. The threshold for photodetachment of $Te^-(^2P_{3/2})$ forming neutral Te in the ground state was investigated by measuring the total photodetachment cross section using a collinear laser-ion beam geometry. The electron affinity was obtained from a fit to the Wigner law in the threshold region.

The error is dominated by the calibration uncertainty of 4 m^{-1} due to the unknown laser line profile, the remainder is due to statistical scatter of the fitted threshold parameters.

Table 7.1.: *Tellurium electron affinity: Comparison of the different measurements. The value in m^{-1} is only given if the publication contains the value.*

Author	Affinity in m^{-1}	Affinity in meV
Slater (1977) [107]		1970.8(3)
Thøgersen (1996) [148]	$1.589\,69(4)\times10^6$	1970.965(50)
This work (1996) [103]	$1.589\,618(5)\times10^6$	1970.876(7)

The electron affinity of lithium

We have investigated the photodetachment threshold of Li^- leading to the formation of the residual Li atom in the $2p\,^2P$ state. The excited residual atom was selectively photo-ionised via an intermediate Rydberg state and the resulting Li^+ ion was detected. A collinear laser-ion beam geometry enabled both high resolution and sensitivity to be attained. We have demonstrated the potential of this state selective photodetachment spectroscopic method by improving the accuracy of Li electron affinity measurements one order of magnitude. From a fit to the Wigner

law in the threshold region, we obtained a Li electron affinity of 498 490(17) m^{-1}.

The uncertainty of 17 m^{-1} is mainly due to a calibration uncertainty of 13 m^{-1}, and the remainder is due to statistical scatter of the fitted threshold values.

Table 7.2.: *Lithium electron affinity: Comparison of the different measurements and calculations. The value in m^{-1} is only given if the publication contains the value.*

Author	Affinity in m^{-1}	Affinity in meV
Experiment		
Feldman (1976) [110]		618.2(5)
Bae (1985) [88]		617.3(7)
Dellwo (1992) [149]	$4.980\,9(16)\times10^5$	617.6(2)
This work [23]	$4.984\,90(17)\times10^5$	618.049(20)
Theory (after 1992)		
Chung (1992) [121]		617.4(2)
Froese Fischer (1993) [122]		617.64

Doubly excited states of Li^-

We report on the first observation of resonance structure in the total cross section for the photodetachment of Li^-. The structure arises from the autodetaching decay of doubly excited $^1P^o$ states of Li^- that are bound with respect to the Li(3p) state. Calculations have been performed for both Li^- and H^- to assist in the identification of these resonances. The lowest lying resonance is analogous to the previously observed $({}_3\{0\}_3^+)$ symmetrically excited intra-shell resonance in H^- but it is much broader. Higher lying resonant states are observed to converge on the Li(3p) limit. These Rydberg-like resonances are much narrower and correspond to asymmetrically excited inter-shell states.

Table 7.3.: *Li^- doubly excited states: Comparison of theoretical results for intra-shell $^1P^o$ states of H^- below the H(n=3) threshold and of Li^- below the Li(3p) threshold. The binding energy E_{bind} is relative to the double detachment limit and E_{trans} is the transition energy from the ground state. Calculated resonance parameters for the two Rydberg like resonances, marked Ry in figure 6.2 (b) page 64, below the Li(3p) threshold are given. Note the strong overlap of these two resonances.*

Element	Label	E_{bind} (eV)	Γ (eV)	E_{trans} (eV)
H^-		−1.706	0.033	12.647
Li^-	Res	−1.688	0.36	4.322
Li^-	Ry	−1.556	0.020	4.453
Li^-	Ry	−1.555	0.016	4.454

The uncertainty in this experiment is caused by the small but unavoidable change in the overlap of the ion and laser beams as the wavelength of the laser was scanned.

The normalisation procedure applied in this experiment was unable to completely account for the beam overlap variation. We estimated, however, that this effect caused a maximum error in the relative cross section over the whole spectrum of less than 10%. The statistical scatter, mainly caused by the shot noise in counting of the neutral particles, is less than 3%.

Doubly excited states of He^-

We investigated Feshbach resonances at the He(n=3) thresholds. The lowermost resonance has been identified to be of $A = -1$ chararcter [139]. The resonance energies are in good agreement with the calculation. The widths have been found to deviate systematically from the predictions.

In all experiments we have combined laser photodetachment and resonance ionisation to study Feshbach resonances associated with the autodetaching decay of doubly excited states of He^-. The measurements were made under the simultaneous conditions of high sensitivity and high energy resolution using a collinear beam apparatus.

Table 7.4.: *He^- doubly excited states: Comparison of the experimental resonance energies and width with the theoretically predicted ones of Xi [140]. The energy positions agree within the limited accuracy of the calculation with the experimental values. Some widths deviate from the predicated values. The numbers in the outermost column on the left refer to the following designations: 1, 1s3s4s ^4S; 2, 1s3p^2 ^4P; 3, 1s3p4p ^4P.*

#	Experiment			Theory			
				length from		velocity form	
	E_r (eV)	E_r (10^6 m^{-1})	Γ (meV)	E_r (eV)	Γ (meV)	E_r (eV)	Γ (meV)
1	2.959 260(6)	2.386 803 1(42)	0.20(2)	2.959 07	0.19	2.959 08	0.18
2	3.072(7)	2.478 2(55)	50(5)	3.074 70	37.37	3.074 71	37.37
3	3.264 87(4)	2.633 297(40)	0.61(5)	3.265 54	1.30	3.265 47	1.31

For the He^-(1s3s4s ^{4}S) state, number 1 in table 7.4, there are two major contributions to the quoted uncertainty: 1 m^{-1} is due to the calibration uncertainty, and the remainder is due to statistical scatter of the fitted resonance parameters. The error of the width reflects the statistical scatter of the fitted width parameter.

For the He^-(1s3p^2 ^{4}P) state, number 2 in table 7.4, there are two major contributions to the error, namely a calibration uncertainty of 40 m^{-1} and the statistical scatter of the fitted resonance parameters of 36 m^{-1}. The uncertainty of the width is entirely due to statistical scatter of the fitted width parameter.

For the He^-(1s3p4p ^{4}P) state, number 3 in table 7.4, we found two dominant source of uncertainty: a calibration uncertainty of 30 m^{-1} and the remainder is due to statistical scatter of the fitted resonance parameters. The uncertainty of the width stems only from statistical scatter of the fitted values.

7.2. Conclusion

In the beginning of the nineties, about fifteen years after the boost from the advent of tunable lasers, high resolution studies of negative ions was a mature field. The most precise method in negative ion studies by that time was laser photodetachment threshold spectroscopy in a collinear geometry. With this methode we studied the photodetachment threshold of tellurium. We attained a value for the electron affinity that ranks among the most accurately known in the periodic system. All the very precise electron affinities had so far been obtained in a collinear geometry with neutral particle detection, but this method is limited to elements with s-wave photodetachment thresholds and has been applied to most suitable elements. The majority of the elements, cannot be investigted with this method.

Using neutral particle detection it is also possible to investigate resonance structure in the photodetachment cross section of negative ions. We were able to measure resonance structure between the Li(3s) and Li(3p) thresholds. The signal contains a large fraction of non-resonantly detached ions, which contribute only to the background, thus masking the sought resonance structure. For higher lying resonances the modultation of the cross section rapidly dwindle, hence aggravating the previously mentioned problems. Furthermore we found that background caused by photo-electrons set a definite upper limit to the usable photon energies. The experiment on the Li^- doubly excited states therefore revealed some limitations of neutral particle detection: to study resonances with very small photodetachment cross sections other more sensitive methods are necessary.

The shortcommings of laser photodetachment spectroscopy with neutral particle detection are eliminated by a novel state selective detection scheme, based on resonance ionisation of the residual atom. The scheme retains all advantages of the collinear geometry, and, at the same time fundamentally augments experimental possibilities. The technique enables seperate studies of partial cross sections with little or no background. To demonstrate the feasibilty of the state selective detection we studied the Li(2p) threshold and obtained a very precise electron affinity. With this state selective detection it will be possible to measure the electron affinities of essentially all metals using favourable s-wave thresholds. It is consequently for the first time possible to determine the electron affinities of almost any elements with the high precision previously only attainable for the few with s-wave photodetachment thresholds. In addition, with the now available tunable infra-red laser light sources investigations of the so far largely unexplored rare earth element negative ions have become possible. Most notably a number of calculations [150–157] predict electron affinities and the fine structure of numerous rare earth negative ions.

This state selective detection was also applied to study three doubly excited state of He^-. Investigations of this metastable three-electron system with neutral particle detection suffered from excessive backgound of neutrals created, in flight, by autodetachment of the He^- ground state. State selective detection remedied this severe problem by completely eliminating this source of background, because the neutrals resulting from autodetachment are in the ground state and are thus not

resonantly ionised. Prior to these investigations studies of doubly excited states of negative ions had essentially been limited to the negative hydrogen ion. The results presented here are a first step towards a systematic study of doubly excited states in another fundamental negative ion.

There is at present a large theoretical activity in the field of doubly excited states in negative ions. Calculations on Li^- showed a good agreement with the experiment presented here. In He^- a recent calculation agrees with the experimentally determined energy and width for the lowest lying doubly excited state $1s3s4s\,^4S$. The energies of the two higher lying $1s3p^2\,^4P$ and $1s3p4p\,^4P$ states agree with calculations, but their width deviates from these predictions. The calculations on Li^- and He^- had a direct impact on our investigations. It is interesting to note that in this research field theory and experiment currently are developing parallelly. We hope and believe the measurements on He^- will inspire theorists to further refine their methods.

One of the new perspectives opened up by the state selective detection is to improve the electron affinities of a large number of elements. Investigations of fine structure of negative ion ground states can often be made in conjunction with affinity measurements. The studies of doubly excited states of negative ions has just begun, and the investigations of He^- and Li^- will be extended towards the double detachment limit. This type of studies can also be pursued further with negative ions with more complex cores like heavier alkaline or alkaline earth metals.

A. Glossary

Table A.1.: *Abbreviation: Acronym expansion of abbreviations used in this thesis.*

Abbreviation	Expansion
a.u.	(Hartree) atomic units
BNC	Banana normal contact
CEM	channel electron multiplier
CG	conducting glass plate
CX	charge exchange chamber
DL	dye laser
DP	deflection plate
EA	electron affinity
EC	extractor of the sputter ion source
EX	excimer laser
FC	Faraday cup
FP	Fabry Perot etalon
GPC	gated photon counter
GPIB	general purpose interface bus
HL	hollow cathode lamp
ID	interaction detection chamber
IO	ioniser of the sputter ion source
L	laser beam
LM	liquid metal
LPT	laser photodetachment threshold spectroscopy
M	sector magnet
MCDF	multi-configuration Dirac Fock
MCHF	multi-configuration Hartree Fock
MCP	micro channel plate
MP	metal plate in PID and NPD
NPD	neutral particle detector
P	photodiode
PD	positive ion detector
PID	positive ion detector
PIS	plasma ion source

continued on next page

continued from previous page

Abbreviation	Expansion
QD	electric quadrupole deflector
QED	Quantum electrodynamics
RIS	resonance ionisation spectroscopy
SIS	sputter ion source
T	sputter target
TC	thermo couple
TOF	time of flight

B. Symbols

I have tried as much as possible to use the standard symbols and notations. Here I compile first the conventions used for the different mathematical objects, and then a table with all symbols in this thesis follows.

Table B.1.: *Symbol conventions: Compilation of how I indicate which type of mathematical object is denoted by the typography.*

Item	typeface	example
vector	upper and lower case bold italic	$\boldsymbol{r}$
variable	italic	t
matrix	uppercase italic	H
Hamilton operator	calligraphic	$\mathcal{H}$
vector operators	bold roman	$\mathbf{L}$
scalar operator	italic	L^2
quantum number	italic	l

Table B.2.: *Symbols in the thesis: Explanation of symbols and variables that appear in this thesis.*

Symbol	Explanation
$\mathcal{H}$	Hamilton operator
$\hbar$	Planck's constant
m	electron mass
$\boldsymbol{\nabla}$	nabla operator
Z	nuclear charge
q	electron charge, Beutler-Fano asymmetry parameter
ϵ_0	dielectric constant
$\boldsymbol{r}$	point in space
$\boldsymbol{r}_{i,j}$	difference vector in space
$\mathbf{L}$	multi-electron angular momentum operator
$\mathbf{l}$	one-electron angular momentum operator
$\mathbf{S}$	multi-electron spin operator
$\mathbf{s}$	one-electron spin operator
$\mathbf{J}$	multi-electron total angular momentum operator

continued on next page

continued from previous page

Symbol	Explanation
$\mathbf{j}$	one-electron total angular momentum operator
ψ	one-electron orbital
Ψ	multi-electron wave function
$R_{nl}(r)$	Laguerre polynomials
$Y_{lm}(\Omega)$	spherical harmonics
Ω	solid angle
ξ	spinor
m_s	magnetic spin quantum number
λ_i	i^{th} set of spatial and spin coordinates
c_i	expansion coefficients
E_{int}	interaction energy
E_{exp}	experimental energy
E_{c}	correlation energy
E_{rel}	relativistic energy
V_{pol}	polarisation potential
α_{D}	electric dipole polarisability
Φ_{cont}	continuum wavefunction
n	principal quantum number
n_{eff}	effective principal quantum number
K	two-electron quantum number
T	two-electron quantum number
A	two-electron quantum number
π	parity
α	fine structure constant
$\sigma(\omega)$, $\sigma(E)$	photodetachment cross section
σ_{W}	Wigner law fit function
σ_{OM}	Wigner law with O'Malley's correction
σ_{BF}	Beutler-Fano profile fit function
σ_{Sh}	Shore fit function for Beutler-Fano profile
σ_{SF}	Starace-Fano fit function
σ_{P}	generalised Beutler-Fano fit function
σ_{Cu}	Wigner cusp fit function
ρ^2	Beutler-Fano correlation parameter
$M_{0\nu}$	transition matrix element
$\mathbf{e}$	polarisation vector operator
$\mathbf{P}_q$	electron momentum operator
ω	frequency of light in SI; energy of light in a.u.
$V(r)$	potential energy
$\boldsymbol{k}$	wave vector
$f_{i,j}(\Omega)$	scattering amplitude

continued on next page

continued from previous page

Symbol	Explanation
j_l	spherical Bessel function
δ_{ij}	Kronecker-Delta symbol
$F(q;\epsilon)$	Beutler-Fano function
Γ	resonance width
E_0	resonance position
$E_0^{\mathrm{r,(b)}}$	red (blue) shifted resonance position

C. He$^-$ partial cross sections

Here I compile partial photodetachment cross sections for He$^-$. Some of them have been presented earlier in this thesis, others are not present because the may not contain resonance structure. Even the non-resonant cross sections can provide valuable information, for example about possible contributions to background. All partial cross section presented here are calculated by Xi and Froese Fischer [130] and kindly provided to aid the interpretation of our data.

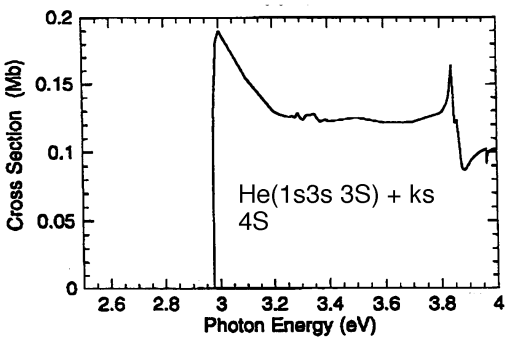

Figure C.1.: *He(1s3s^{3}S) partial cross section of ^{4}S symmetry: The parital photodetachment cross section monitored by selectively detecting He atoms in the 1s3s^{3}S state [130].*

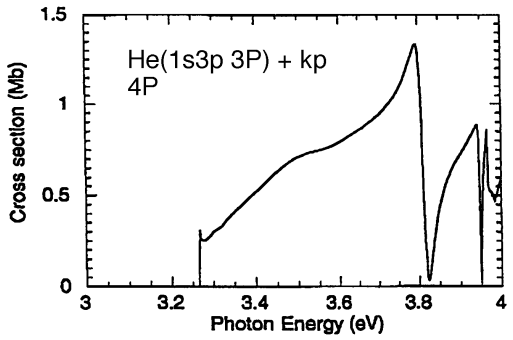

Figure C.2.: *He(1s3p $^3P^o$) partial cross section of ^4P symmetry: The partial photodetachment cross section monitored by selectively detecting He atoms in the 1s3p $^3P^o$ state [130].*

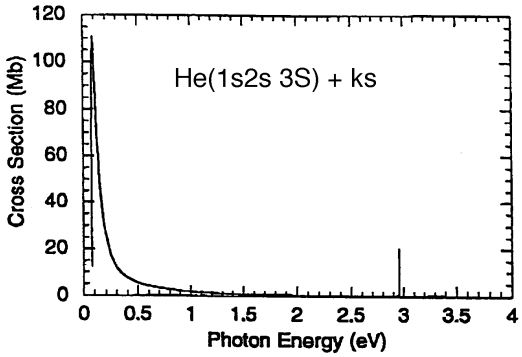

(a) Overview of He(1s2s ^{3}S) partial cross sections of ^{4}S symmetry

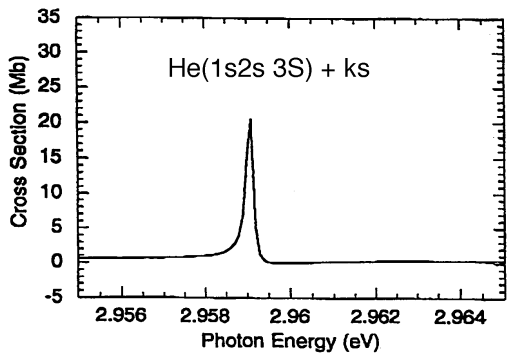

(b) He(1s2s ^{3}S) partial cross sections of ^{4}S symmetry near the 1s3s4s ^{4}S state

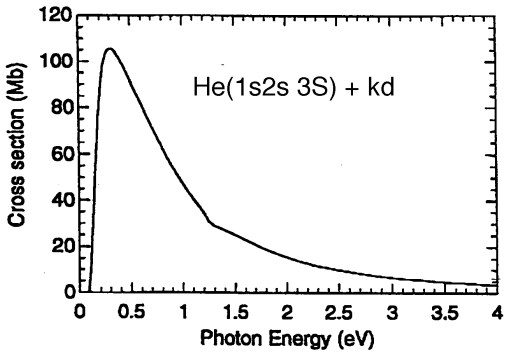

(c) Overview of He(1s2s ^{3}S) partial cross sections of ^{4}D symmetry

Figure C.3.: *He(1s2s ^3S) partial cross sections: The partial photodetachment cross sections monitored by selectively detecting He atoms in the 1s2s ^3S state [130].*

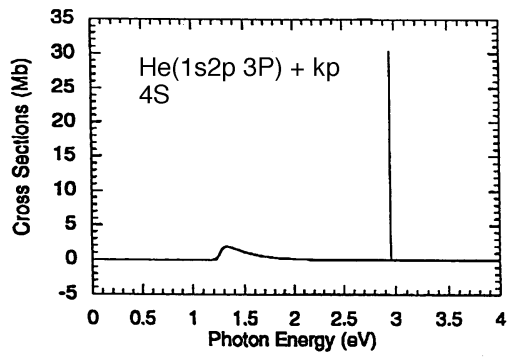

(a) Overview of He(1s2p ^{3}P^o) partial cross sections of ^{4}S symmetry

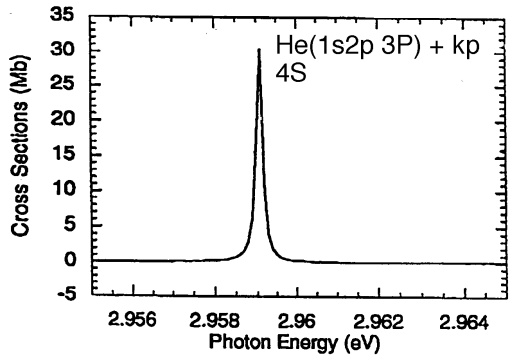

(b) He(1s2p ^{3}P^o) partial cross sections of ^{4}S symmetry near the 1s3s4s ^{4}S state

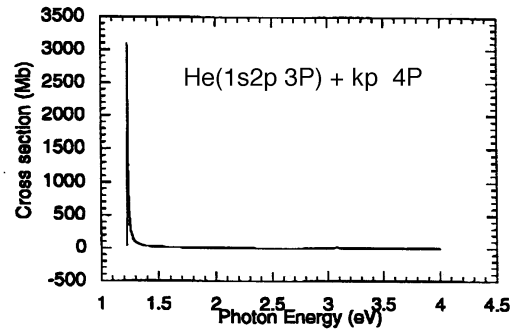

(c) Overview of He(1s2p ^{3}P^o) partial cross sections of ^{4}P symmetry

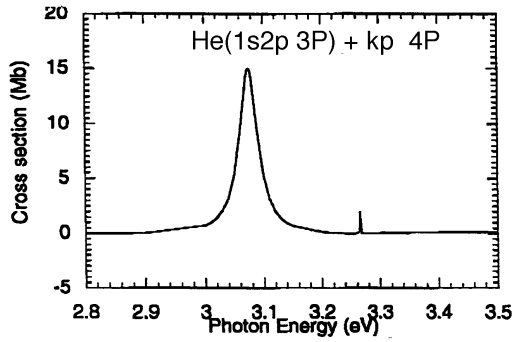

(d) He(1s2p ^{3}P^o) partial cross sections of ^{4}P symmetry near the 1s3p^2 ^{4}P and 1s3p4p ^{4}P state

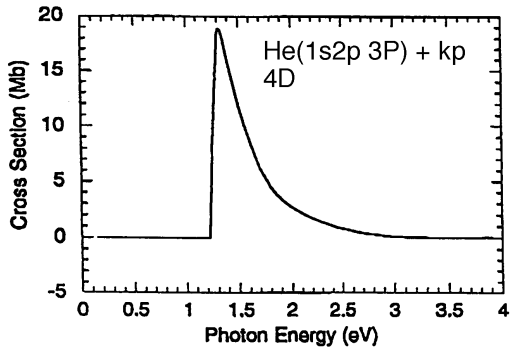

(e) Overview of He(1s2p ^{3}P^o) partial cross sections of ^{4}D symmetry

Figure C.4.: *The He(1s2p $^3P^o$) partial cross sections: The partial photodetachment cross sections monitored by selectively detecting He atoms in the 1s2p $^3P^o$ state [130].*

Bibliography

[1] U. Ljungblad, A. Klinkmüller, and D. Hanstorp. A new apparatus for studies of negative ions. In Mike Hopkins and Samantha Fahy, editors, *Fifth european workshop on the production and application of light negative ions*, pages 35–40, Glasnevin, Dublin 9, Ireland, March 1994. Dublin City University.

[2] U. Berzinsh, G. Haeffler, D. Hanstorp, A. Klinkmüller, E. Lindroth, U. Ljungblad, and D. J. Pegg. Resonance structure in the Li^- photodetachment cross section. In R. C. Thompson, editor, *5th EPS conference on atomic and molecular physics*, page 65, Edinburgh, UK, April 1995. European physical society.

[3] A. E. Klinkmüller, G. Haeffler, U. Berzinsh, D. Hanstorp, I. Yu. Kiyan, U. Ljungblad, D. J. Pegg, and J. Rangell. Electron affinities of As, Te and Li: A comparison of three different measurements. In *RIS-96, Program and Abstracts*, page 131. Eighth interantional symposium on resonance ionisation spectroscopy and its applications, June 1996.

[4] G. Haeffler, A. E. Klinkmüller, D. Hanstorp, I. Yu. Kiyan, C. W. Ingram, D. J. Pegg, and J. R. Peterson. Photodetachment study of doubly excited states in He^-. *Bull. Am. Phys. Soc.*, 42(2):1136, April 1996.

[5] G. Haeffler, U. Berzinsh, D. Hanstorp, I. Yu. Kiyan A. E. Klinkmüller, U. Ljungblad, and J. Rangell. Electron affinities of As, Te and Li: A comparison of three different measurements. *Bull. Am. Phys. Soc.*, 41(3):1086, May 1996.

[6] Andreas E. Klinkmüller, Gunnar Haeffler, Dag Hanstorp, Chris W. Ingram, Igor Yu. Kiyan, Uldis Berzinsh, David J. Pegg, and James R. Peterson. Photodetachment study of He^- resonances. In H.-D. Kronfeldt, editor, *29. EGAS Berlin abstracts*, europhysics conference abstracts, pages 16–17. European group for atomic spectroscopy, European physical society, July 1997.

[7] Andreas E. Klinkmüller, Gunnar Haeffler, Dag Hanstorp, Chris W. Ingram, Igor Yu. Kiyan, Uldis Berzinsh, David J. Pegg, and James R. Peterson. Photodetachment study of He^- resonances. In F. Aumayr, G. Betz, and H. P. Winter, editors, *XX. ICPEAC*, volume 1, page WE047, July 1997.

[8] L. Kerwin, editor. *Symbols, units and nomenclature in physics.* U.I.P. 20. Union internationale de physique pure et appliquée, 1978.

[9] Barry N. Taylor. Guide for the use of the international system of units (SI). NIST Special publication 811, United States Department of Commerce Technology Administration, National Institute of Standards and Technology, Gaithersburg, MD-20 899-0001, April 1995.

[10] E. Richard Cohen and Barry N. Taylor. The 1986 CODATA recommended values of the fundamental physical constants. *J. Phys. Chem. Ref. Data*, 17(4):1795–1803, 1988.

[11] Sir Harrie Massey. *Negative ions*. Cambridge University Press, The Pitt building, Trumpington street, Cambridge CB2 1RP, third edition, 1976.

[12] B. M. Smirnov. *Negative Ions*. McGraw-Hill, New York, 1976.

[13] Stephen J. Buckman and Charles W. Clark. Atomic negative-ion resonances. *Rev. Mod. Phys.*, 66(2):539–655, April 1994.

[14] A. V. Esaulov. Electron detachment from atomic negative ions. *Ann. Phys. Fr.*, 11(5):493–592, October 1986.

[15] T. Andersen. Spectroscopy of negativ ions. *Phys. Scr.*, T34:23–35, 1991.

[16] V. A. Oparin, R. N. II'in, I. T. Serenkov, and E. S. Solov'ev. Negative ion exicted states and the determination of their binding energy by electron detachment by an electric field. *Sov. Phys.-JETP*, 39(6):989–994, 1974.

[17] M.-J. Nadeau, X.-L. Zhao, M. A. Garwan, and A. E. Litherland. Ca negative ion binding energy. *Phys. Rev. A*, 46(7):R3588–R3590, October 1992.

[18] Gordon W. F. Drake, editor. *Atomic molecular & optical physics* HANDBOOK, chapter 58, pages 681–689. American Institute of Physics, 1996.

[19] Gordon W. F. Drake, editor. *Atomic molecular & optical physics* HANDBOOK, chapter 59, pages 690–700. American Institute of Physics, 1996.

[20] H. Hotop and W. C. Lineberger. Binding energies in atomic negative ions. *J. Phys. Chem. Ref. Data*, 14(3):731–750, 1985.

[21] C. Blondel. Recent experimental achievements with negative ions. *Phys. Scr.*, T58:31–42, 1995.

[22] V. V. Petrunin, J. D. Voldstad, P. Balling, P. Kristensen, and T. Andersen. Resonant ionization spectroscopy of Ba^-: Metastable and stable ions. *Phys. Rev. Lett.*, 75(10):1911–1914, September 1995.

[23] Gunnar Haeffler, Dag Hanstorp, Igor Kiyan, Andreas E. Klinkmüller, Ulric Ljungblad, and David J. Pegg. Electron affinity of Li: A state-selective measurement. *Phys. Rev. A*, 53(6):4127–4131, June 1996. e-print: physics/9703013.

[24] P. G. Harris, H. C. Bryant, A. H. Mohagheghi, R. A. Reeder, H. Sharifian, C. Y. Tang, J. B. Donahue, C. R. Quick, D. C. Rislov, W. W. Smith, and J. E. Stewart. Observation of high lying resonances in the H^- ion. *Phys. Rev. Lett.*, 65(3):309–312, 1990.

[25] T. Andersen, L. H. Andersen, P. Balling, H. K. Haugen, P. Hvelplund, W. W. Smith, and K. Taulbjerg. Metastable-ion lifetime studies utilizing a heavy-ion storage ring: Measurements on He^-. *Phys. Rev. A*, 47(2):890–896, February 1993.

[26] D. J. Larson, C. J. Edge, R. E. Elmquist, N. B. Mansour, and R. Trainham. Physics with negative ions in ion traps. *Phys. Scr.*, T22:183–190, 1988.

[27] D. J. Larson and R. Stoneman. Photodetachment of atomic negative ions near threshold in a magnetic field. *Phys. Rev. A*, 31(4):2210–2214, 1985.

[28] M. Crance. Multiphoton detachment from the negtive ion of fluorine. *J. of Phys. B*, 20:L411–L416, February 1987.

[29] C. Blondel and C. Delsart. Two-photon detachment from the negative ions F^- and I^-: Angular distributions with elliptically polarised light. *Nucl. Instrum. Methods B*, 79:156–158, June 1993.

[30] H. Stapelfeldt, P. Kristensen, U. Ljungblad, T. Andersen, and H. K. Haugen. Autoionizing states of negative ions in strong resonant laser fields: The negative rubidium ion. *Phys. Rev. A*, 50:1618–1626, August 1994.

[31] P. Kristensen, H. Stapelfeldt, P. Balling, and T. Andersen. Spectroscopy of negative ions utilizing multiphoton detachment in a Raman coupling regime. *Phys. Rev. Lett.*, 71(21):3435–3438, November 1993.

[32] J. Thøgersen, L. D. Steele, M. Scheer, H. K. Haugen, P. Kristensen, P. Balling, H. Stapelfeldt, and T. Andersen. Fine structure measurements for negative ions: Studies of Se^- and Te^-. *Phys. Rev. A*, 53(5):3023–3028, May 1996.

[33] M. Weissbluth. *Atoms and Molecules.* Academic Press, New York, 1986.

[34] Robert Duane Cowan. *The theory of atomic structure and spectra*, chapter 4, pages 93–141. Los Alamos series in basic and applied sciences. University of California Press, Berkeley and Los Angeles, California, 1981.

[35] M. Ya. Amusia. *Atomic Photoeffect*, chapter 1.3, pages 6–7. Physics of atoms and molecules. Plenum press, New York and London, 1990.

[36] J. A. Alonso and N. A. Cordero. Variation of the ground state correlation energy of atoms with atomic number. *J. of Phys. B: At., Mol. Opt.*, 29:1629–1636, 1996.

[37] Sten Salomonson, Håkan Warston, and Ingvar Lindgren. Many-body calculations of the electron affinity for Ca and Sr. *Phys. Rev. Lett.*, 76(17):3092–3095, April 1996.

[38] T. Brage and C. Froese Fischer. Autodetachment of negative ions. *Phys. Rev. A*, 44:72–79, 1991.

[39] Gordon W. F. Drake, editor. *Atomic molecular & optical physics* HANDBOOK, chapter 21, pages 243–257. American Institute of Physics, 1996.

[40] Hans A. Bethe and Edwin E. Salpeter. *Quantum mechanics of one- and two-electron atoms.* Springer Verlag, Berlin–Göttingen–Heidelberg, third edition, 1957. published by Plenum Publishing Corporation.

[41] J. W. Cooper, U. Fano, and F. Pratts. Classification of two electron excitations of helium. *Phys. Rev. Lett.*, 10(12):518–521, 1963.

[42] R. P. Madden and K. Codling. New auto-ionizing atomic energy levels in He, Ne, and Ar. *Phys. Rev. Lett.*, 10(12):516–518, 1963.

[43] Paul Rehmus, Michael E. Kellman, and Stephen Berry. Spatial correlation of atomic electrons: He. *Cont. Phys.*, 31:239–262, 1978.

[44] A. R. P. Rau. Group theoretical treatment of strongly correlated atomic dynamics. *Rep. on Prog. in Phys.*, 53:181–220, 1990.

[45] R. S. Berry. How good is Niels Bohr's atomic model? *Cont. Phys.*, 30(1):1–19, 1989.

[46] J. M. Rost and J. S. Briggs. Saddle structure of the three body Coulomb problem; symmetries of doubly excited states and propensity rules for transitions. *J. of Phys. B: At., Mol. Opt.*, 24:4293–4322, 1991. Topical review.

[47] Dieter Wintgen and Klaus Richter. Semiclassical nature of planetary atom states. *Comments At. Mol. Phys.*, 29(5):261–274, January 1994.

[48] C. D. Lin. *Review of fundamental processes and applications of atoms and ions*, book 8., pages 357–401. World Scientific Co. Pte. Ltd., P O Box 128, Farrer Road, Singapore 91 28, 1993.

[49] C. D. Lin. Classification of two-electron doubly excited states. *Comments At. Mol. Phys.*, 19(2):89–98, 1987.

[50] O. Sinanoğlu and D. R. Herrick. Group theoretic prediction of configuration mixing effects due to Coulomb repulsions in atoms with applications to doubly-excited spectra. *J. Chem. Phys.*, 62:886–892, 1975.

[51] O. Sinanoğlu and D. R. Herrick. Erratum: Group theoretic prediction of configuration mixing effects due to Coulomb repulsions in atoms with applications to doubly excited spectra [J. Chem. Phys. 62, 886 (1975)]. *J. Chem. Phys.*, 65:850, 1976.

[52] D. R. Herrick and O. Sinanoğlu. Comparison of doubly excited helium energy levels, isoelectronic series, auto-ionization lifetimes, and group theoretical configuration mixing predictions with large configuration interaction calculations and experimental spectra. *Phys. Rev. A*, 11:97–110, 1975.

[53] C. D. Lin. Properties of resonance states in H^-. *Phys. Rev. A*, 14:30–35, 1976.

[54] M. E. Kellman and D. R. Herrick. Rotor-like spectra for some doubly excited two-electron states. *J. of Phys. B: At. and Mol.*, 11:L755–L759, 1978.

[55] D. R. Herrick and M. E. Kellman. Novel supermultiplet energy levels for doubly excited He. *Phys. Rev. A*, 21:418–425, 1980.

[56] D. R. Herrick, M. E. Kellman, and R. D. Poliak. Supermultiplet classification of higher intrashell doubly excited states of H^- and He. *Phys. Rev. A*, 22(4):1517–1535, October 1980.

[57] C. D. Lin. Properties of high-lying doubly excited states of H^-. *Phys. Rev. A*, 25(3):1535–1545, March 1982.

[58] C. D. Lin. Radial and angular correlations of doubly excited electrons. *Phys. Rev. A*, 25(1):76–87, January 1982.

[59] J. M. Feagin and J. S. Briggs. Molecular descripion of two-electron atoms. *Phys. Rev. Lett.*, 57:984–987, 1986.

[60] Carl Wulfman. Approximate dynamical symmetry of two-electron atoms. *Chem. Phys. Lett.*, 23(3):370, December 1973.

[61] C. Wulfman. Configuration mixing within the 2s-2p shell. *Phys. Rev. Lett.*, 51(13):1159–1162, September 1983.

[62] Thomas A. Heim. Decay properties of doubly excited ridge states. *J. of Phys. B: At., Mol. Opt.*, 26:4343–4365, 1993.

[63] C. D. Lin. Classification and supermultiplet structure of doubly excited states. *Nucl. Instrum. Methods B*, 240:572–576, 1985.

[64] J. M. Rost and J. S. Briggs. Propensity rules for radiative and non-radiative decay of doubly-excited states. *J. of Phys. B: At., Mol. Opt.*, 23:L339 – L346, 1990.

[65] P. Tykesson. The production of negative heavy ion beams through charge exchange processes. Symposium of Northeastern Accelerator Personnel Oak Ridge, Tennessee, USA., October 1978.

[66] M. Ya. Amusia. *Atomic Photoeffect*, chapter 2.1, pages 13–16. Physics of atoms and molecules. Plenum press, New York and London, 1990.

[67] Yu. N. Demkov and V. N. Ostrovskii. *Zero-range potentials and their applications in atomic physics*, chapter 1.3, pages 8–14. Physics of atoms and molecules. Plenum Press, 233 Spring Street, New York, N.Y. 10 013, 1988.

[68] M. Ya. Amusia. *Atomic Photoeffect*, chapter 3.6, pages 72–74. Physics of atoms and molecules. Plenum press, New York and London, 1990.

[69] Eva Lindroth. private communication, 1994.

[70] Eugene P. Wigner. On the behavior of cross sections near thresholds. *Phys. Rev.*, 73(9):1002–1009, 1948.

[71] Y. K. Bae and J. R. Peterson. Modified photodetachment threshold behavior near resonances. In J. R. Peterson D. C. Lorents, W. E. Meyerhof, editor, *Electronic and atomic collisions*, pages 799–806. Elsevier Science Publisher, 1986.

[72] H. Friedrich. *Theoretische Atomphysik*. Springer–Lehrbuch. Springer–Verlag, Berlin, 1990.

[73] C. J. Joachain. *Quantum Collision Theory*, volume 1. North Holland Publishing Company, Amsterdam, 1975.

[74] George Arfken. *Mathematical methods for physicists*. Academic Press, INC., 1985.

[75] Thomas F. O'Malley. Effect of long-range final state forces on the negative ion photodetachment cross section near threshold. *Phys. Rev.*, 137(6A):A1668–A1672, March 1965.

[76] H. Hotop and W. C. Lineberger. Dye-laser photodetachment studies of Au^-, Pt^-, PtN^-, and Ag^{-*}. *J. Chem. Phys.*, 58(6):2379–2387, March 1973.

[77] H. Hotop, T. A. Patterson, and W. C. Lineberger. High resolution photodetachment study of se^- ions. *Phys. Rev. A*, 8(2):762–774, August 1973.

[78] John W. Farley. Photodetachment cross section of negative ions: The range of validity of the Wigner threshold law. *Phys. Rev. A*, 40(11):6286–6292, December 1989.

[79] J. R. Peterson, Y. K. Bae, and D. L. Huestis. Threshold behavior near an electronic shape resonance: Analysis of the $He(^3P)$ threshold in He^- photodetachment and determination of the $He(2^3S)$ electron affinity. *Phys. Rev. Lett.*, 55(7):692–695, August 1985.

[80] C. W. Walter, J. A. Seifert, and J. R. Peterson. Re-examination of the He^- $1s2p^2\,{}^4P^e$ shape resonance: Details of its properties and a precise electron affinifty for He $2\,{}^3S$. *Phys. Rev. A*, 50(3):2257–2262, September 1994.

[81] U. Fano. Effects of configuration interactions on intensities and phase shifts. *Phys. Rev.*, 124:1866–1878, 1961.

[82] T. A. Ferrett, D. W. Lindle, P. A. Heimann, W. D. Brewer, U. Becker, H. G. Kerkhoff, and D. A. Shirley. Lithium $1s$ main line and satellite photo-emission: Resonant and nonresonant behavior. *Phys. Rev. A*, 36(7):3172–3183, October 1987.

[83] Bruce W. Shore. Parametrization of absorption line profiles. *Phys. Rev.*, 171(1):43–54, July 1968.

[84] Anthony F. Starace. Behavior of partial cross sections and braching ratios in the neighborhood of a resonance. *Phys. Rev. A*, 16(1):231–242, July 1977.

[85] H. Friedrich. *Theoretische Atomphysik*, chapter 3.2.3, pages 138–143. Springer–Lehrbuch. Springer–Verlag, Berlin, 1990.

[86] C. H. Green. private communication, 1995.

[87] H. Friedrich. *Theoretische Atomphysik*, chapter 1.4.3, pages 36–38. Springer–Lehrbuch. Springer–Verlag, Berlin, 1990.

[88] Young K. Bae and James R. Peterson. Effect of a virtual state near an s-wave threshold: Absolute Li^- photodetachment cross sections near the $Li(2\,{}^2P)$ threshold. *Phys. Rev. A*, 32(3):1917–1920, September 1985.

[89] M. Ya. Amusia. *Atomic Photoeffect*, chapter 3.7, pages 74–77. Physics of atoms and molecules. Plenum press, New York and London, 1990.

[90] S. L. Kaufman. High-resolution laser spectroscopy in fast beams. *Opt. Comm.*, 17(3):309–312, 1976.

[91] Roy Middelton. A negative ion cookbook, October 1989.

[92] Jörgen Roslund. Design of a sputter negative ion source system. Master's thesis, Chalmers tekniska högskola AB, S-412 96 Göteborg, Sweden, August 1995. GIPR-330, ISSN 0280-2872.

[93] E. Harting and F. H. Read. *Electrostatic lenses*. Elsevier scientific publishing company, Amsterdam-Oxford-New York, 1976.

[94] Gunnar Haeffler. Photodetachment spectroscopy: Negative ion bound states and resonances. Master's thesis, Göteborgs Universitet och Chalmer tekniska högskola AB, Department of atomic physics, S–412 96 Göteborg, 1996. ISBN 91-7197-379-6.

[95] D. Hanstorp. A secondary emission detector capable of preventing detection of the photoelectric effect induced by pulsed lasers. *Meas. Sci. Technol.*, 3:523–527, 1992.

[96] D. Hanstorp, C. Bengtsson, and D. J. Larson. Angular distribution in photodetachment from O^-. *Phys. Rev. A*, 40(2):670–675, July 1989.

[97] Jonas Rangell. Computer control and wavelength calibration of a dye laser. GIPR 337, Göterborgs universitet and Chalmers tekniska högskola AB, SE-412 96 Göteborg, Sweden, 1996. ISSN 0280-2872.

[98] W. H. Press, B. P. Flannery, S. A. Teukolsky, and W. T. Vetterling. *Numerical Recipes. The Art of Scientific Computing (FORTRAN Version).* Cambridge University Press, Cambridge, 1989.

[99] D. Hanstorp and M. Gustafsson. Determination of the electron affinity of iodine. *J. of Phys. B: At., Mol. Opt.*, 25:1773–1783, 1992.

[100] D. M. Neumark, K. R. Lykke, T. Andersen, and W. C. Lineberger. Laser photodetachment measurement of the electron affinity of atomic oxygen. *Phys. Rev. A*, 32(3):1890–1892, September 1985.

[101] U. Berzinsh, M. Gustafsson, D. Hanstorp, A. Klinkmüller, U. Ljungblad, and A.-M. Mårtensson-Pendrill. Isotope shift in the electron affinity of chlorine. *Phys. Rev. A*, 51(1):231–238, January 1995.

[102] C. Blondel, P. Cacciani, C. Delsart, and R. Trainham. High-resolution determination of the electron affinitiy of fluorine and bromine using crossed ion and laser beams. *Phys. Rev. A*, 40:3698–3701, October 1989.

[103] Gunnar Haeffler, Andreas E. Klinkmüller, Jonas Rangell, Uldis Berzinsh, and Dag Hanstorp. The electron affinity of tellurium. *Z. Phys. D*, 38:211–214, October 1996. e-print: physics/9703012.

[104] Lennart Minnhagen. Spectrum and the energy levels of neutral argon, Ar I. *J. Opt. Soc. Am.*, 63(10):1185–1198, 1973.

[105] Edward S. Chang and William G. Schoenfeld. Improved experimental and theoretical energy levels of neon I. *Phys. Scr.*, 49:26–33, 1994.

[106] Victor Kaufman and Lennart Minnhagen. Accurate ground term combinations in Ne I. *J. Opt. Soc. Am.*, 62(1):92–95, January 1972.

[107] J. Slater and W. C. Lineberger. High resolution photodetachment studies of P^- and Te^-. *Phys. Rev. A*, 15(6):2277–2282, June 1977.

[108] G. S. Hurst, M. G. Payne, S. D. Kramer, and J. P. Young. Resonance ionization spectroscopy and one-atom detection. *Rev. Mod. Phys.*, 51(4):767–819, October 1979.

[109] U. Ljungblad, D. Hanstorp, U. Berzinsh, and D. J. Pegg. Observation of doubly excited states in Li^-. *Phys. Rev. Lett.*, 77(18):3751–3754, October 1996.

[110] D. Feldmann. Infra-red photodetachment threshold measurements: Li^- and P^-. *Z. Phys. A*, 277:19–25, 1976.

[111] L. D. Landau and E. M. Lifschitz. *Quantenmechanik*. Akademie-Verlag-Berlin, 1979.

[112] I. I. Fabrikant. Theory of negative ion decay in an electrical field. *J. of Phys. B*, 26:2533–2541, 1993.

[113] B. M. Smirnov and M. I. Chibisov. The breaking up of atomic particles by an electrical field and by electron collisions. *Sov. Phys.-JETP*, 22(3):585–592, 1966.

[114] Yu. N. Demkov and G. F. Drukarev. Loosely bound particle with nonzero orbital angular momentum in an electric or magnetic field. *Sov. Phys.-JETP*, 54(4):650–656, 1981.

[115] Yu. N. Demkov and G. F. Drukarev. Decay and polarizability of negative ions in an electric field. *Sov. Phys.-JETP*, 20(3):614–618, March 1964.

[116] C. E. Moore. *Atomic Energy Levels as Derived from the Analysis of Optical Spectra. Volume I. ^1H to ^{23}V*, volume 35 of *National Standards Reference and Data Series*. National Bureau of Standards (U. S.), Washington, 1975.

[117] Y. K. Bae and J. R. Petersson. Near-threshold measurements of K^- two-electron photo-ionization cross section. *Phys. Rev. A*, 37(9):3254–3258, May 1988.

[118] N. L. Manakov, V. D. Ovsyannikov, and L. P. Rapoport. Atomic calculations using pertubation theory with a model potential. *Opt. Spectrosc.*, 38(2):115–117, February 1975.

[119] J. Dellwo, Y. Liu, D. J. Pegg, and G. D. Alton. Near-threshold photodetachment of the Li^- ion. *Phys. Rev. A*, 45(3):1544–1547, February 1992.

[120] Craig J. Sansonetti and Bruno Richou. Precise measurements of the lithium resonance lines by doppler-free frequency modulation spectroscopy. *Bull. Am. Phys. Soc.*, 40(4):1272–1273, 1995.

[121] Kwong T. Chung and Paul Fullbright. Electron affinity of lithium. *Phys. Scr.*, 45:445–449, 1992.

[122] Charlotte Froese Fischer. Convergence studies of MCHF calculations for Be and Li^-. *J. of Phys. B: At., Mol. Opt.*, 26(5):855–862, 1993.

[123] D. Hanstorp, G. Haeffler, A. E. Klinkmüller, U. Ljungblad, U. Berzinsh, I. Yu. Kiyan, and D. J. Pegg. Two-electron dynamics in photodetachment. *Adv. Quant. Chem.*, 29, 1997. e-print: physics/9706013.

[124] U. Berzinsh, G. Haeffler, D. Hanstorp, A. Klinkmüller, E. Lindroth, U. Ljungblad, and D. J. Pegg. Resonance structure in the Li^- photodetachment cross section. *Phys. Rev. Lett.*, 74(24):4795–4798, June 1995. e-print: physics/9703015.

[125] Andreas E. Klinkmüller, Gunnar Haeffler, Dag Hanstorp, Igor Yu. Kiyan, Uldis Berzinsh, Christopher Ingram, David J. Pegg, and James R. Peterson. Photodetachment study of the $1s3s4s\,^4S$ resonance in He^-. *Phys. Rev. A*, 56(4):2788–2791, October 1997. e-print: physics/9703011.

[126] Cheng Pan, Anthony F. Starace, and Chris H. Green. Photodetachment of Li^- from the Li $3s$ threshold to the Li $6s$ threshold. *Phys. Rev. A*, 53(2):840–852, February 1996.

[127] Eva Lindroth. Photodetachment of H^- and Li^-. *Phys. Rev. A*, 52(4):2737–2749, October 1995.

[128] C. Pan, A. F. Starace, and C. H. Greene. Parallels between high doubly excited state spectra in H^- and Li^- photodetachment. *J. of Phys. B: At., Mol. Opt.*, 27:L137, 1994.

[129] M. E. Hamm, R. W. Hamm, J. Donahue, P. A. M. Gram, J. C. Pratt, M. A. Yates, R. D. Bolton, D. A. Clark, H. C. Bryant, C. A. Frost, and W. W. Smith. Observation of narrow resonances in the H^- photodetachment cross section near the $n = 3$ threshold. *Phys. Rev. Lett.*, 43(23):1715–1718, 1979.

[130] Jinhua Xi and Charlotte Froese Fischer. private communication, 1996.

[131] Julius W. Hiby. Massenspektrographische Untersuchungen an Wasserstoff- und Heliumstrahlen (H_3^+, H_2^-, HeH^+, HeD^+, He^-). *Analen der Phys.*, 34:473–487, 1939. (5. Folge).

[132] V. V. Petrunin, H. H. Andersen, P. Balling, P. Kristensen, and T. Andersen. Resonance ionization spectroscopy of negative ions. In *15th international conference on atomic physics Zeeman-effect centenary*, page ThE2, Amsterdam, The Netherlands, 1996.

[133] A. V. Bunge and C. F. Bunge. Electron affinity of helium $(1s2s)\,^3S$. *Phys. Rev. A*, 19(2):452–456, February 1979.

[134] R. N. Compton, G. D. Alton, and D. J. Pegg. Photodetachment cross sections for $He^-(^4P^o)$. *J. of Phys. B: At., Mol. Opt.*, 13:L651–L655, 1980.

[135] R. V. Hodges, M. J. Coggiola, and J. R. Peterson. Photodetachment cross sections for $He^-\ ^4P$. *Phys. Rev. A*, 23(1):59–63, January 1981.

[136] D. J. Pegg, J. S. Thompson, J. Dellwo, R. N. Compton, and G. D. Alton. Partial cross sections for the photodetachment of metastable He^-. *Phys. Rev. Lett.*, 64:278–281, 1990.

[137] A. U. Hazi and K. Reed. Theoretical photodetachment cross section for $He^-(^4P^o)$. *Phys. Rev. A*, 24(4):2269–2272, October 1981.

[138] H. P. Saha and R. N. Compton. Theoretical studies of the photophysics of $He^-(1s2s2p)^4P^o$. *Phys. Rev. Lett.*, 64(13):1510–1513, March 1990.

[139] Maryvonne Le Dourneuf and Shinichi Watanabe. Grandparent model of the doubly excited He^{-**} resonances from a hypersperical viewpoint. *J. of Phys. B: At., Mol. Opt.*, 23:3205–3224, 1990.

[140] Jinhua Xi and Charlotte Froese Fischer. Cross section and angular distribution for the photodetachment of $He^-(1s2s2p\,^4P^o)$ below the $He(n = 4)$ threshold. *Phys. Rev. A*, 53(5):3169–3177, May 1996.

[141] W. L. Wiese, M. W. Smith, and B. M. Glennon, editors. *Atomic transition probabilities*, volume I, hydrogen through neon of *National standard reference data series*. United States Department of Commerce, 1966.

[142] Miroslaw Bylicki. Spectrum of doubly excited $^4P^e$ resonances in He^-. *J. of Phys. B: At., Mol. Opt.*, 30:189–201, 1997.

[143] Spyros I. Themelis and Cleanthes A. Nicolaides. Energies, widths and l-dependence of the H^- ^3P and He^- ^4P TEIL states. *J. of Phys. B: At., Mol. Opt.*, 28:L379–L385, 1995.

[144] W. F. Meggers, C. H. Corliss, and B. F. Scribner. NBS Monograph 145, 1975.

[145] R. L. Kurucz and E. Peytremann. SAO Special Report 362, 1975.

[146] Spyros I. Themelis and Cleanthes A. Nicolaides. Effect of interchannel coupling on the partial and total auto-ionization widths: Application to the $1s3s3p\,^4P^o$ and $1s3p^2\,^4P$ states for $Z{=}2-5, 10$. *Phys. Rev. A*, 49(3):1618–1622, March 1994.

[147] Brian F. Davis. Energy and auto-ionization width of the $1s3s3p\,^4P^o$ and the $1s3p3p\,^4P$ states in lithium-like ions. *Phys. Rev. A*, 41(11):5844–5855, June 1990.

[148] J. Thøgersen, M. Scheer, L. D. Steele, H. K. Haugen, and W. P. Wijesundera. Two-photon detachment of negative ions via magnetic dipol transitions. *Phys. Rev. Lett.*, 76(16):2870–2873, April 1996.

[149] J. Dellwo, Y. Liu, C. Y. Tang, D. J. Pegg, and G. D. Alton. Photodetachment cross section for Li^-. *Phys. Rev. A*, 46(7):3924–3928, 1992.

[150] S. H. Vosko, J. A. Chevary, and I. L. Mayer. Predictions of stable Yb^- in the $P^o_{1/2}$ state: The importance of spin-orbit coupling. *J. of Phys. B: At., Mol. Opt.*, 24:L225–L231, 1991.

[151] S. H. Vosko, J. B. Lagowski, I. L. Mayer, and J. A. Chevary. Theoretical study of even- and odd-parity states in La^- and Ac^-: Evidence for the uniqueness of La^-. *Phys. Rev. A*, 43:6389–6392, 1991.

[152] A. A. Gribakina, G. F. Gribakin, and V. K. Ivanov. The structure and photodetachment of the Yb^- negative ion. *Phys. Rev. Lett.*, 68:280–284, August 1992.

[153] K. Dinov, D. R. Beck, and D. Datta. Electron affinities of six bound states of Ce^- formed by attachment of $6p$ and $5d$ electrons to Ce. *Phys. Rev. A*, 50(2):1144–1148, August 1994.

[154] Debais Datta nad Donald R. Beck. Electron affinities of opposite parity bound states on Th^-: Relativistic-configuration-interaction studies. *Phys. Rev. A*, 50(2):1107–1111, August 1994.

[155] Konstantin Dinov and Donald R. Beck. Electron affinities of $6p$ electrons in Pr^-. *Phys. Rev. A*, 51(2):1680–1682, February 1995.

[156] Konstantin Dinov and Donald R. Beck. Electron affinity and hyperfine structure for U^- and U I obtained from relativistic configuration-interaction calculations. *Phys. Rev. A*, 52(4):2632–2637, October 1995.

[157] Konstantin Dinov and Danald R. Beck. Electron affinity of Pa by $7p$ attachment and hyperfine constants for Pa^-. *Phys. Rev. A*, 53(6):4031–4035, June 1996.